CRITICAL PARAMETERS IN MAGMATIC DEGASSING

A

THESIS

Presented to the Faculty
of the University of Alaska Fairbanks

in Partial Fulfillment of the Requirements
for the Degree of

DOCTOR OF PHILOSOPHY

By

Joanna Mongrain, MChem, MEng.

Fairbanks, Alaska

August 2008

CRITICAL PARAMETERS IN MAGMATIC DEGASSING

By

Joanna Mongrain

RECOMMENDED:

Advisory Committee Chair

Chair, Department of Geology and Geophysics

APPROVED:

Dean, College of Natural Science and Mathematics

Dean of the Graduate School

Dec 12, 2008

Date

Abstract

Decompression experiments conducted at pressures up to 200MPa and temperatures of 825°C-880°C on hydrated K-phonolite and rhyolite melts were used to explore the critical parameters controlling nucleation, exsolution and degassing behavior. Experiments on the low viscosity/surface tension K-Phonolite melt highlighted the role of melt properties. Although the sample porosities deviated below equilibrium values for pressures less than ~40MPa, the melt exsolved water in equilibrium over all the pressures and decompression rates studied. Melt shearing is proposed to have caused bubble deformation and alignment, lowering the porosity at which extensive permeability develops and significant degassing occurs compared to rhyolite.

Experiments on a rhyolite melt decompressed slowly from 100 MPa and then held at 10 MPa for up to 900 s highlighted the critical parameters controlling the formation and stability of a highly vesicular magma: bubble number density, bubble size distribution and porosity. The porosity of the interconnected, highly vesicular network decreased during "Stage I" degassing and the bubble size distribution evolved from a unimodal population to include a population of much larger bubbles. During Stage II degassing, the network collapsed. Pre-collapse and collapse degassing rates were obtained and a coalescence-induced coalescence model proposed to explain the rapid destabilization.

The ability of a melt to efficiently exsolve volatiles and the ease of bubble coalescence are both a function of the initial distribution of nucleated bubbles. The development of a new method for quantifying this distribution using spatial statistics will allow future

researchers to explore the underlying controls on nucleation such as melt structure and the occurrence of a prior nucleation event.

To investigate the critical parameters controlling shallow dike intrusion and therefore magmatic ascent rate, the fracture mechanics of intrusion into homogeneous and layered (weak sandstone/strong granite) particle models under lithostatic, compressive and extensional regimes were examined. Although the scale of the model intrusions were an order of magnitude greater than field observations, extensive microfracturing across the weaker layers, parallel dike jointing in the stronger layers and a length scale dependence to fracture toughness were observed suggesting that the use of a particle code is a promising approach to intrusion modeling.

Table of Contents

Page

List of Figures

Page

List of Tables

Page

Acknowledgements

I wish to thank the following organizations for their financial support; National Science Foundation, UAF Department of Geology and Geophysics, UAF Geophysical Institute, UAF Graduate School, Alaska Volcano Observatory, CSIRO, College of Natural Science and Mathematics and the Geological Society of America. I am very grateful that through their combined support, I had an RA or thesis completion grant for my entire PhD and thus was able to fully concentrate on my research. Their support further allowed me to attend two AGU meetings, a GSA field forum in Yosemite, the volcanological field school in Katmai and to travel to Canada and Australia to complete components of this PhD. These experiences were invaluable in the transformation from hesitant student to "researcher".

Thanks to Penny King for the use of her micro-reflectance FTIR apparatus. I loved visiting the lab and meeting other students who were as enthralled with bubbles and melt properties as I.

Thanks also to Alison Ord of CSIRO who encouraged and supported my visit to CSIRO. I enjoyed the work immensely in spite of the >100 degree Fahrenheit weather whilst pregnant.

Thanks to my committee for guidance over the last few years, particularly John Eichelberger who acted as my advisor early on, provided introductions to prominent researchers and was always excited by my enthusiasm for some new research.

I am most appreciative of the constant encouragement, support and time of my advisor, Jess Larsen particularly over the last year. I specifically wish to thank her for giving me the freedom to follow research directions, working patiently though the many writing problems and for the intellectually stimulating conversations. That the papers became easier to write/wrangle is mostly due to her help. I'm still somewhat amazed that I wrote a thesis.

The finish line would not have been reached without the specific support of the following friends and family; My mum and Marian for coming out to Fairbanks and looking after Daniel, Mariah, Katie Jacobs and Yiming for the frequent progress meetings, Kristin, Lea and Katie Hessen for babysitting, Mum and Dad for encouragement through some of the darker times.

Finally and most importantly, I would like to thank my husband Jake for his constant support and encouragement and for putting the completion of this thesis above progress on his own. I'll pay you back in a few years. Thanks for sharing and juggling the demands of babies and PhD's with me- it's been a little crazy but fun.

Chapter 1 Introduction

Volcanic eruptions are energetically driven by volatile exsolution. During magmatic ascent, bubbles nucleate in the melt as the dissolved volatiles become supersaturated in the melt with respect to external pressure. As the melt pressure decreases further, the volatile phase continues to diffuse into the bubbles which grow and may coalesce. The process of volatile diffusion out of the melt and into bubbles is defined as exsolution. This rapidly exsolving volatile phase expands the magma and dramatically accelerates it towards the surface. If the free vapor phase can be efficiently removed/degassed from the magma and conduit system during magmatic ascent, the resulting eruption will be effusive. If degassing is inefficient the melt may fragment as a result of one or more of several possible mechanisms:1) bubble overpressure leading to catastrophic failure of bubble walls, 2) shear forces within the magma causing brittle or ductile failure of the melt leading to bubble wall rupture. The extent to which a magma can exsolve and degas volatiles is critical to predicting the eruptive style.

Estimated ascent/decompression rates for explosive and effusive eruptions typically differ by orders of magnitude, suggesting that the timescales over which magma can exsolve water vapor or other volatiles and degas at shallow depths are critical in determining the resulting eruptive mechanism (Eichelberger 1995; Eichelberger et al. 1986; Westrich et al. 1988). Experimental decompression studies provide valuable information on the kinetics of volatile exsolution in silicate melts. Recent results show that higher viscosity rhyolites tend to exsolve in disequilibrium at faster decompression rates (>0.25MPa/s);(Burgisser and Gardner 2004; Gardner et al. 1999; Gardner et al.

2000) whilst a lower viscosity Na-Phonolite remains in equilibrium under similar decompression conditions (Larsen and Gardner 2004). The critical properties controlling volatile exsolution are surface tension (Mangan et al. 2004; Sparks 1978), volatile species diffusivity (Proussevitch and Sahagian 1996) and viscosity (Toramaru 1995).

Degassing is also a time dependent process. Degassed silicic magmas are found not only in the centre of volcanic domes resulting from effusive eruptions (Fink et al. 1992) but also in the degassed magmatic plugs in conduits that are thought to lead to Vulcanian-style explosions (Cashman and McConnell 2005; D'Oriano et al. 2005; Hammer et al. 1999; Taddeucci et al. 2004). These degassed magmas are thought be derived from a permeable magmatic foam at shallow depths which is able to efficiently degas and collapse. Thus, the timescale of permeability development and hence degassing in volcanic conduits is closely tied with eruption mechanism, and is a critical component to our understanding of eruptive mechanisms.

An important parameter in exsolution is the diffusive path length. If a volatile species has on average a very short pathway to a bubble, the time taken to arrive at that bubble will also be short and equilibrium exsolution is more likely to result for a given ascent rate. We would expect therefore that the spatial distribution of the bubbles may be important in determining if exsolution will be in equilibrium or not.

Finally, the blithe use of ascent rates belies that fact that most dikes injected into composite volcanoes never make it to the surface (Gudmundsson 1995; Gudmundsson 2002; Marinoni and Gudmundsson 2000). In addition to assessing the impact of various

melt and magma properties in determining eruptive style, we need to understand what controls the ascent rate itself. The mechanics which allow or prevent a dike reaching the surface are not well understood. However, since the intrusions tend to be of similar density to the surrounding rock, fracture mechanics rather than buoyant rise may be the controlling mechanism at shallow depths. Determining the parameters which control fracture mechanics at shallow depths in volcanic setting is important in predicting volcanic eruptions.

This studies contained in this thesis investigate four major aspects of exsolution and degassing: the role of surface tension and/or viscosity on exsolution and degassing behavior during ascent, the mechanism by which a completely degassed magma can form at shallow depths, the proposed use of spatial statistics to quantify nucleation, and the role of lithology and regional stress regimes on dike propagation.

In the first chapter, an experimental study on the behavior of a hydrated K-Phonolite melt from Vesuvius 79AD eruption, a well know explosive eruption under decompression is presented. Alkalic melts differ in water solubility (Carroll and Blank 1997) and viscosity (Whittington et al. 2001) from rhyolites and might be expected to behave very differently on decompression. Through bubble characterization, the relative roles of surface tension and viscosity on exsolution and also degassing behavior are assessed. This has implications for how such magmas may behave differently than rhyolite is discussed in the context of explosive volcanism.

The study in the second chapter documents the experimental creation of an interconnected, highly vesicular rhyolite from a H_2O-saturated rhyolitic melt. The results of the study are compared to previous experimental studies on coalescence in rhyolitic melts (Burgisser and Gardner 2004; Gardner 2007) in order to expose the critical parameters driving the formation of an interconnected bubbly network, and its subsequent destabilization and collapse. The implications of the findings of this study for the mechanisms of explosive and effusive eruptions are also discussed.

In the third chapter, the power of using spatial statistics, through the use of the R package Spatstat, to characterize bubble populations is demonstrated. The technique is used to quantitatively describe the bubble populations in a well characterized heterogeneous nucleated sample and to distinguish between two similarly complex heterogeneously nucleated samples. Potential further applications of the technique are also explored.

The final chapter is a study of dike intrusions at shallow depths using a particle code. Through this study the relative importance of lithology and regional stress regimes on the ability of a dike to propagate to the surface are assessed. This study also serves as a test of the particle code model in volcanic settings.

The work contained in this thesis explores many of the critical parameters whose values determine if a volcanic eruption will occur and what style it will take. The findings contained within the chapters are a substantial contribution to the field of volcanology and will be of use to other researchers.

References

Burgisser, A. and Gardner, J.E., 2004. Experimental constraints on degassing and permeability in volcanic conduit flow. Bulletin of Volcanology, 67(1): 42-56.

Carroll, M.R. and Blank, J.G., 1997. The solubility of H_2O in phonolitic melts. American Mineralogist, 82: 549-556.

Cashman, K.V. and McConnell, S.M., 2005. Multiple levels of magma storage during the 1980 summer eruptions of Mount St. Helens, WA. Bulletin of Volcanology, 68: 57-75.

D'Oriano, C. et al., 2005. Changes in eruptive style during the AD 1538 Monte Nuovo eruption (Phlegrean Fields, Italy): The role of syn-eruptive crystallization. Bulletin of Volcanology, 67: 601-621.

Eichelberger, J.C., 1995. Silicic volcanism; ascent of viscous magmas from crustal reservoirs. Annual Review of Earth and Planetary Sciences, 23: 41-63.

Eichelberger, J.C., Carrigan, C.R., Westrich, H.R. and Price, R.H., 1986. Non-explosive silicic volcanism. Nature, 323(6089): 598-602.

Fink, J.H., Anderson, S.W. and Manley, C.R., 1992. Textural constraints on effusive silicic volcanism: Beyond the permeable foam model. Journal of Geophysical Research, 97: 9073-9083.

Gardner, J.E., 2007. Bubble coalescence in rhyolitic melts during decompression from high pressure. Journal of Volcanology and Geothermal Research, 166: 161-176.

Gardner, J.E., Hilton, M. and Carroll, M.R., 1999. Experimental constraints on degassing of magma; isothermal bubble growth during continuous decompression from high pressure. Earth and Planetary Science Letters, 168(1-2): 201-218.

Gardner, J.E., Hilton, M. and Carroll, M.R., 2000. Bubble growth in highly viscous silicate melts during continuous decompression from high pressure. Geochimica et Cosmochimica Acta, 64(8): 1473-1483.

Gudmundsson, A., 1995. Infrastructure and mechanics of volcanic systems in Iceland. Annual Review of Earth and Planetary Sciences, 28(107-140).

Gudmundsson, A., 2002. Emplacement and arrest of sheets and dykes in central volcanoes. Journal of Volcanology and Geothermal Research, 116: 279-298.

Hammer, J., Cashman, K.V., Hoblitt, R.P. and Newman, S., 1999. Degassing and microlite crystallization during pre-climatic events of the 1991 eruption of Pinatubo, Philippines. Bulletin of Volcanology, 60: 355-380.

Larsen, J.F. and Gardner, J.E., 2004. Experimental study of water degassing from phonolite melts: implications for volatile oversaturation during magmatic ascent. Journal of Volcanology and Geothermal Research, 134: 109-124.

Mangan, M.T., Sisson, T.W. and Hankins, W.B., 2004. Decompression experiments identify kinetic controls on explosive silicic eruptions. Geophysical Research Letters, 31: no.8, 4.

Marinoni, L.B. and Gudmundsson, A., 2000. Dykes, faults and palaeostresses in Teno and Anaga massifs of Tenerife (Canary Islands). Journal of Volcanology and Geothermal Research, 103(83-103).

Proussevitch, A.A. and Sahagian, D.L., 1996. Dynamics of coupled diffusive and decompressive bubble growth in magmatic systems. Journal of Geophysical Research, 101: 17447-17455.

Sparks, R.S.J., 1978. The dynamics of bubble formation and growth in magmas; a review and analysis. Journal of Volcanology and Geothermal Research, 3(1-2): 1-37.

Taddeucci, J., Pompilio, M. and Scarlato, P., 2004. Conduit Processes during the July-August 2001 explosive activity of Mt Etna (Italy): Inferences from glass chemistry crystal size distribution of ash particles. Journal of Volcanology and Geothermal Research, 137: 33-54.

Toramaru, A., 1995. Numerical study of nucleation and growth of bubbles in viscous magmas. Journal of Geophysical Research, B, Solid Earth and Planets, 100(2): 1913-1931.

Westrich, H.R., Stockman, H.W. and Eichelberger, J.C., 1988. Degassing of rhyolitic magma during ascent and emplacement. Journal of Geophysical Research, 93(B6): 6503-6511.

Whittington, A., Richet, P., Linard, Y. and Holtz, F., 2001. The viscosity of hydrous phonolites and trachytes. Chemical Geology, 174: 209-224.

Chapter 2 Rapid water exsolution, degassing, and bubble collapse observed experimentally in K-phonolite melts.[1]

Abstract

We performed three sets of decompression experiments on a hydrated K-phonolite melt at 880°C in order to study the exsolution and degassing behavior of this low viscosity melt. The range of decompression rates studied was 0.01MPa/s to 0.25MPa/s. The pressure range was 200MPa to 10MPa. We determined that the melt exsolved water in equilibrium at all pressures at the decompression rates studied using micro-reflectance FTIR, a new method which is particularly well suited to determining the dissolved water concentration in high porosity experimental samples. Below 40-50MPa at all decompression rates, the samples exsolved water in equilibrium, but the sample porosities deviated from values derived from equilibrium calculations/experiments and instead porosities remained constant or even decreased at lower pressures. The bubbles in all samples were predominantly deformed with features characteristic of partially collapsed bubble textures apparent at low pressures. Analysis of the bubble size distributions and deformation parameters indicate that melt shearing due to bubble growth and attendant sample expansion may cause the bubbles to deform, leading to the formation of bubble chains. The deformation and alignment of bubbles increases connectivity and lowers the porosity at which extensive permeability develops. In this

[1] J. Mongrain , J.F. Larsen, and P.L. King submitted to Journal of Volcanology and Geothermal Research, currently in press.

situation, many of the connected bubbles are in contact with external vapor leading to significant degassing at 40-50MPa. This degassing reduces the sample porosity and creates collapsed bubble textures at low pressures. This behavior differs significantly from that of hydrated rhyolite melts.

Keywords: bubbles; decompression; degassing; coalescence; deformation; micro-reflectance FTIR

Introduction

Volatile exsolution drives volcanic eruptions, as a rapidly exsolving volatile phase expands the magma and dramatically accelerates it towards the surface. Estimated ascent/decompression rates for explosive and effusive eruptions typically differ by orders of magnitude, suggesting a connection between magma decompression rate, volatile exsolution, and the fragmentation process linked to explosive eruptions (Woods and Koyaguchi 1994). This process has been extensively studied in high SiO_2 rhyolites but only recently have alkalic phonolitic and trachytic magmas been studied, despite their ability to produce extremely violent eruptions, such as those of Vesuvius and Laacher See (Sheridan et al. 1981; Wömer and Schmincke 1984). Alkalic melts differ in water solubility (Carroll and Blank 1997) and viscosity (Whittington et al. 2001) from rhyolites, and it may not be reasonable to apply experimental results from rhyolitic melts to model alkalic magmatic processes. The purpose of this study is to examine the fundamental behavior of K-rich alkalic melts as they exsolve water, and discuss the implications for

how such magmas may behave differently than rhyolite in the context of explosive volcanism.

Methods

Experiments utilized crushed pumice from the 79AD eruption of Vesuvius, Italy (Cioni 2000; Cioni et al. 1995; Gurioli et al. 2005). The purpose of the study is not to replicate vesiculation processes during that eruption, but rather to examine first-order changes in porosity and permeability in phonolite melt over a range of potential magma ascent rates. The first set of experiments consisted of isobaric, isothermal runs to determine equilibrium H_2O solubility at 880 °C and static pressures from 200 to 50 MPa. Ten to 30 mg samples were welded into 15 mm long by 5 mm (outer diameter), by 0.17 mm wall thickness Ag tubes, along with ~10 wt. % de-ionized water to ensure vapor saturation, and were held for 6-7 days at experimental pressure. The second set of experiments comprised three decompression series. Solid water saturated glass slugs were first synthesized using the methods detailed above with experimental conditions of 200MPa and 880 °C. These were then sectioned into 5 by 3 mm slabs, re-loaded into 4 mm diameter Ag or Au tubes and re-equilibrated at 880 °C and 200 MPa for 30 minutes in rapid-quench capable cold-seal vessels. They were then decompressed rapidly to 100 MPa and held at this pressure for 30 minutes, producing a bubble population in equilibrium with the melt. The experiments were further decompressed step-wise, at average decompression rates from 0.01 MPa/s to 0.25 MPa/s and then quenched at final pressures between 90 and 10 MPa (Table 2.1), equivalent to depths of ~0.4 to 3.6 km in a volcanic conduit, assuming a lithostatic pressure gradient. The samples were quenched by

pulling the experiments down into a water cooled jacket using a magnet. Using this experimental setup, the experiments are estimated to quench in around 2s (Gardner et al. 1999; Lyakhovsky et al. 1996). The vessel and pressure lines are open to a larger reservoir attached to the intensifier, so that the increase in vessel pressure as the hot capsule and holder are pulled down into the water cooled jacket area and cool is limited. For example, for a sample quenched at 30 MPa, the total increase in vessel pressure is 5 MPa during quenching. The samples were removed from their capsules, sectioned and polished providing thick sections for bubble size measurements. A petrographic microscope with an attached camera was used to produce digital photomicrographs. These were analyzed using the ImageJ program (Larsen and Gardner 2004) to determine sample bubble size distributions and porosities. Sample porosities were measured using photomicrographs acquired in reflected light with 3-6 images per sample. Bubble sizes were measured using photomicrographs acquired in transmitted light and a minimum of 150 bubbles per sample were measured, where possible, to create the bubble size distributions (BSD). As most of the bubbles in the experiments are deformed into approximate ellipsoids (Figure 2.1 (C)), the equivalent bubble radius (a) was calculated using Eq. 1 where (l) is the observed long axis and (b) is the short axis, assuming a prolate ellipsoid shape. We assumed that the two short axes are equivalent for all bubbles. Although the polished sections are not generally aligned to the direction of bubble elongation, only bubbles which were in focus were measured so that the long axis measured should approximate the long axis of the ellipsoid.

$$a = \sqrt[3]{lb^2} \quad (1)$$

The degree of deformation was calculated using the dimensionless parameter, D characterized by Eq. 2. (Rust et al. 2003).

$$D = {(l-b)}/{(l+b)} \quad (2)$$

Total water concentrations were measured via a newly developed micro-reflectance FTIR method that provided a way to constrain dissolved water concentrations in experimental glasses without the need for doubly polished thin sections (King et al. 2006). This enabled the measurement of total water concentrations in extremely fragile samples quenched at low pressures (<40 MPa), which had porosities up to 60 to 70 vol. %. These measurements would have been impossible using standard transmission FTIR techniques requiring doubly polished, 50 to 100 μm thick glass wafers. Water concentrations were measured at the University of Western Ontario using the Nicolet Nexus 670 FTIR with a Continuum microscope and an attached LN-cooled MCT-A detector to collect reflectance spectra in the region 5400-650 cm^{-1}, which spans the principle 3750 cm^{-1} combined OH and H_20 vibrations. The samples were singly-polished and the IR spectrum measured relative to the reflectance spectrum of a polished gold standard, used to collect the background atmospheric H_2O and CO_2 concentrations. The raw reflectance data were smoothed to a 40.5 cm^{-1} window and Kramers-Kronig absorbance spectra, KK-Abs, were

calculated. This corrects spectra for the optical dispersion due to a specular reflection component of the reflectance spectra. The KK-Abs was measured from a linear baseline for H_20 total. The composition specific KK-Abs can be calibrated against an independent measure of glass water contents to derive a calibration coefficient (m) in order to determine the total dissolved H_20 using Eq. 3.

$$Total\ H_2O\ wt.\% = \left(3550cm^{-1} band\ KK - Abs\right) \times m \qquad (3)$$

For the K-phonolite, a calibration coefficient of 204 was used based upon transmission and micro-reflectance FTIR analyses of total water dissolved in experimental glasses of an Na-phonolite (King et al. 2006) from a prior experimental study (Larsen and Gardner 2004). The systematic error is assumed to be low based on a <10 % difference between the measured transmission FTIR extinction coefficients, calibrated using Karl Fisher Titration, for a similar K-phonolite in a study by Iacono Marziano et al. (2007) and those of Na-phonolite glasses determined by Carroll and Blank (1997). Independent verification was made by comparing unpublished solubility data obtained for the K-phonolite used in this study at 1000 °C with those obtained via transmission FTIR by Iacono Marziano et al. (2007) at 1050 °C, and both sets of data agreed within error, indicating our use of the Na-phonolite calibration curve is acceptable.

Two repeat experiments were performed to document reproducibility (Table 2.1). The repeat experiment 79VB15_2_12_3_4 (Table 2.1) was decompressed at 0.25MPa/s and quenched at 80 MPa. It reproduced the bubble number density, porosity, mean bubble

radius and average deformation parameter within one standard deviation of the original experiment. The repeat experiment 79VB15_2_12_3_6 (Table 2.1) was decompressed at 0.25 MPa/s and quenched at 30 MPa. It had a slightly higher bubble number density, probably due to more bubbles being nucleated initially, though they are still close (within 0.3 orders of magnitude). The mean bubble radii agree within 1 standard deviation with the lower mean bubble radii being associated with the higher bubble number density as expected for a higher initial bubble number density. Also, their porosities and the estimated average deformation parameter were reproduced within 1 standard deviation.

Results

Experimental porosities as a function of final pressure

Visual observations of the experiments show that K-phonolite glasses quenched at different final pressures (Table 2.1) have very different textures from their rhyolite counterparts. Those quenched at >40 MPa have irregular vesicles, and show the formation of bubble chains, though the samples themselves tend to hold together as solid slugs (Figure 2.1(A)). At final pressures <40 MPa, the recovered samples are fragmental and contain highly irregular vesicles with "tails" indicative of bubble collapse (Table 2.1; Figure 2.1(B)).

To evaluate how porosity develops in the K-phonolite, the same equilibrium model employed by a previous study (Gardner et al. 1999) was used to calculate expected bubble porosities via dissolved water concentration, final pressure, and expansion of water vapor at the experimental conditions. The total water solubility for the K-phonolite

melts was measured and derived from the isobaric, isothermal saturation experiments run specifically for this purpose (Table 2.1). K-phonolite melts decompressed at an average rate of 0.25 MPa/s follow the predicted equilibrium porosity trend at final pressures between 90 and 50 MPa, but between 30 and 10 MPa, the experimental porosities show a sharp decrease from 32 to 17 vol. %. The trend in samples decompressed at 0.01 MPa/s is similar, as between 40 and 20 MPa the porosity decreases from 53 vol. % to 38 vol. %. A similar trend is observed for samples decompressed at 0.05MPa, although porosities level off at around 30 vol. % below 50 MPa. In sum, rather than approaching equilibrium at the lowest quench pressures (Burgisser and Gardner 2004), the K-phonolite porosities decrease measurably or remain approximately constant below 40 MPa at all average decompression rates applied in this study.

Water concentrations as a function of final pressure

Figure 2.3 shows the total water concentrations measured in the quenched K-phonolite experimental glasses as a function of final pressure in comparison with the water solubility curve measured at 880 °C and pressures between 50 and 200 MPa (Table 2.1). Samples from both 0.05 and 0.25 MPa/s decompression regimes have total dissolved water concentrations that predominantly track the solubility curve within 1 standard deviation error.

Bubble size distributions

Table 2.1 and Figure 2.4 summarize the bubble size distribution (BSD) for each decompression series. Overall, the three series show similar trends in BSD. In general, the BSD broadens as the pressure decreases. An initial increase in mean bubble radius as

the pressure decreases towards ~40 MPa is reversed as the pressure falls further. In the 0.01 MPa/s series (Figure 2.4 (a)) at 80 MPa, the BSD is narrow, with most bubbles having an equivalent radius of <10 μm and a mean bubble radius of 8(13) μm where the number in parentheses is the standard deviation. At 60 MPa, the population has broadened to include bubbles of >50 μm in radius with a mean bubble radius of 24(32) μm. At 40 MPa the mean bubble size is 39(51) μm and the BSD has broadened to include bubbles >80 μm in radius with a diminished small bubble population (<10 μm). At 20 MPa, the mean bubble size has decreased to 26(32) μm, with the whole population shifted towards smaller bubble radii. In the 0.05 MPa/s series (Figure 2.4b) at 70 MPa, the BSD is narrow with most bubbles having a radius of <20 μm and a mean bubble radius of 10(11) μm. At 50 MPa, the BSD has broadened with most bubbles having a radius of 10-30μm and a mean bubble radius of 18(19) μm. At 10 MPa, the BSD is broad but retains a large population of small bubbles (<20 μm) and a mean bubble radius of 30(38) μm. In the 0.25 MPa/s series (Figure 2.4(c)), the BSD at 90 MPa and 80 MPa are similar with most bubbles <10 μm and mean bubble radii of 7(10) μm. At 50 MPa the population has broadened to include bubble radii up to 30 μm and a mean bubble radius of 17(30) μm. At 10 MPa, the BSD has broadened substantially to include bubbles >50 μm with a mean bubble radius of 22(28) μm. Almost all the bubbles in the samples show some deformation with average D values (Eq. 2) ranging from 0.14 to 0.24 (Table 2.1). This is in sharp contrast to bubbles in quenched decompression rhyolite experiments which are typically spherical (Burgisser and Gardner 2004; Gardner et al. 1999; Larsen and Gardner 2000; Mourtada-Bonnefoi and Laporte 2004).

Discussion

A striking observation of this study is the behavior of the experimental porosities as a function of pressure. In all decompression series, the porosities reach only a maximum of 30 to 53 vol. % at low pressures of 30 to 40 MPa, despite having tracked the equilibrium porosity curve at higher pressures. Using the criteria of Burgisser and Gardner (2004) that coalescence is observed when the ratio of the standard deviation of mean bubble radius to the bubble radius is approximately unity, coalescence occurs from the start of each decompression series. Calculations of the bubble number density (BND) using the method of Gardner et al. (1999) show a decrease with lower quench pressures which may also support this (Table 2.1). However, the application of this method for these samples is not statistically robust because of the small number of bubbles present at low pressures.

The decrease in porosities relative to equilibrium at lower pressures could reflect either disequilibrium exsolution with retarded bubble growth, bubble collapse with the onset of degassing of the experimental samples, Ostwald ripening of sample edge bubbles or degassing due to bubbles rising out of the melt. The hypothesis of disequilibrium exsolution is disproved by the reflectance FTIR results which demonstrate that the experimental glasses contain equilibrium dissolved water concentrations at all final pressures (Figure 2.3). We shall show that degassing due to bubble rise is too slow and Ostwald ripening too fast at all pressures to account for the low porosities at lower pressures. The remaining hypothesis is that the experimental samples developed extensive permeability at pressures around 30 to 40 MPa leading to significant degassing and subsequent bubble collapse. In order to explore this hypothesis and how it might

relate to natural systems, we need to understand how bubble coalescence and shear in the capsules relates to the percolation threshold, the development of extensive connectivity, degassing, and subsequent bubble collapse.

Bubble Rise

To investigate the hypothesis that the low experimental porosities were a result of sample degassing as bubbles rose out of the sample, we estimated the bubble rise velocity using the following formulation of Stokes Law:

$$v = \frac{2}{9\mu}\left(a^2 g(\rho_b - \rho_m)\right) \qquad (4)$$

where v is bubble rise velocity in m/s, g is gravitational acceleration, μ is the viscosity of the melt, a is the bubble radius in m, ρ_b is the bubble gas density and ρ_m is the melt density. At 100 MPa and 880 °C the dissolved water concentration is estimated to be 3.83 wt. % (from r-FTIR data).Under these conditions the viscosity of the phonolite melt is estimated to be $10^{3.54}$ Pas (Hui and Zhang 2006) with a melt density of 2300 kgm^{-3}. Equation 4 predicts that a bubble with a radius of 30 μm will rise at a rate of 1.2 nm/s and take a total of 1200 hours to rise the complete length of the sample (~5 mm). As the viscosity increases with decreased dissolved water saturation, the rise rate will be reduced by several orders of magnitude as the sample is decompressed. It is therefore unlikely that any significant proportion of the bubble population rose out of the melt slug during the total duration of the longest experiments.

Ostwald Ripening

To investigate the hypothesis that the low experimental porosities arise from Ostwald ripening of internal or sample edge bubbles which degas or are not imaged, we used the ripening timescale detailed in Proussevitch et al. (1993). Ostwald ripening is the growth of bubbles through diffusive gas exchange between bubbles of differing internal pressures. Gas diffuses from the small high pressure bubbles to the larger lower pressure bubbles, resulting in the annihilation of small bubbles and a larger average bubble size.

$$\tau^* = \frac{r_0^{\,2} P \delta}{4RTD_f \sigma L} \qquad (5)$$

where τ^* is the ripening timescale, P is the melt pressure, δ is the interbubble spacing, R is the ideal gas constant, T is temperature, D_f is the diffusivity of H_20, σ is the surface tension and L is the solubility of H_20 in the melt per fixed bubble gas pressure. At 100 MPa and 880 °C, the melt-vapor surface tension is estimated to be 0.063 Nm^{-1}, the dissolved water concentration 3.83 wt. % and diffusivity $2.4x10^{-10}$ m^2s^{-1} (Iacono Marziano et al. 2007) . At 30 MPa and 880 °C, the melt-vapor surface tension is estimated to be 0.099 Nm^{-1}, the dissolved water concentration 2.04 wt. % and the diffusivity $2.4x10^{-10}$ m^2s^{-1}. Using a cross sample pathway of 2mm, a bubble in the center of the sample with a radius of 10 microns undergoing Ostwald ripening in the presence of large sample edge bubbles at 100MPa should collapse after 15 hours and after 79 hours at

30 MPa. The slow timescales at high and low pressures suggest that Ostwald ripening diffusion to edge bubbles as a mechanism for porosity reduction at low pressures is unlikely.

Bubble Deformation

Cause of deformation

Bubble deformation occurs when shear stresses are greater than the restoring surface tension, which tends to minimize the melt-bubble interfacial area. The ratio of these stresses is the capillary number Ca, which is defined as

$$Ca = a\tau/\sigma \qquad (6)$$

Where a is the equivalent bubble radius, τ is the shear stress and σ is the surface tension. The surface tension for a hydrated rhyolitic melt (3.44 wt. % H_2O) at 825 °C is estimated to be σ=0.135 Nm^{-1} (Bagdassarov et al. 2000; Mangan et al. 2004). A hydrated phonolitic melt (3.83 wt. % H_2O) at 880°C has an estimated surface tension of σ=0.063 Nm^{-1} (Larsen 2006). The ratio of the capillary numbers for a bubble subject to a given shear stress in the phonolite melt versus the rhyolite melt is 2.12. As a result of the lower surface tension of K-phonolite melt, bubbles in phonolite melts are more likely to deform than bubbles in rhyolitic melts under the same shear stresses and this may be key to understanding their differences in behavior during decompression. If the estimated surface tension of K-phonolite melt were closer to that estimated for rhyolite at similar

conditions (Iacono Marziano et al. 2007), we would expect to see similar degrees of bubble deformation in the two melts.

Source of Shear Stress

The deformed nature of the bubbles leads us to infer that there is an element of shear stress acting at all pressures on the bubbles. We propose that the source of this shear stress is localized melt shearing that occurs in the experimental capsules as a result of expansion as the sample porosity increases. As nearby bubbles expand due to exsolution and/or decompression, the surrounding melt shears. In an experimental capsule this shearing will be primarily along the capsule length, leading to deformation in a dominant direction, and hence the creation of bubbles chains along that direction. Manga and Stone (1994) observed a similar phenomenon in translating close bubbles where the stress field produced by one bubble deformed a nearby bubble, leading to a horizontal velocity component for the nearby bubble, and subsequent bubble alignment.

The shear stress can be related to the shear rate though Eq. 7 where G is the shear rate and μ is the melt viscosity

$$\tau = G\mu \qquad (7)$$

For pure and simple shear of bubbles in melts with a Reynolds number, Re, as given by Eq. 8 below, and capillary number, Ca $<<1$, the capillary number is related to the deformation parameter, D as shown in Eq. 9 and Eq. 10 respectively (Cox 1969; Taylor 1932; Taylor 1934).

$$\mathrm{Re} = \rho_m G a^2 / \mu \tag{8}$$

$$D = 2Ca \tag{9}$$

$$D = Ca \tag{10}$$

Bubble dynamics in magmas are typically characterized by small Re (7) where ρ_m is the melt density, μ is the melt viscosity, a is the bubble radius and G is the shear rate. Using the parameters from section 4.1 for shear rates less than 0.6 s^{-1}, the capillary number is less than 1. The Reynolds number is less than one for shear rates less than 1.7×10^9 s^{-1}. The estimated shear rates in the study by Larsen and Gardner (2000) on deformed bubbles adjacent to large hydration bubbles was in the range G=0.001-0.02 s^{-1} for a melt of similar viscosity with similar D values. It should be reasonable therefore to apply Eq. 9 or Eq. 10 to the results of this study. The type of shear is unknown in these experiments, but assuming it is simple shear results in the highest estimated shear rates. This assists in the assessment of whether Eq. 9 and Eq. 10 are applicable. The highest calculated shear rate is 0.4 s^{-1}, implying that the application of these equations to these samples is valid.

Figure 2.5 shows the calculated shear stress for all samples assuming simple shear. The shear stress decreases approximately linearly as the quench pressure decreases for all decompression series. The 0.01 $MPas^{-1}$ series may plot lower than the other faster series.

The decrease in shear stress with pressure may be explained by the greater increase in radius per unit volume when the bubbles are small (high quench pressures) than in the larger bubbles quenched at lower pressures. Figure 2.6 shows the calculated shear rate for all samples, which indicates how the effect of the shear stress is modified by the melt viscosity (Eq. 7). As the samples are decompressed and lose water via exsolution, the melt increases in viscosity. Between 90 and 50 MPa, the shear rate decreases linearly from approximately 0.4 s^{-1} to almost zero. Below 50MPa, the shear rate remains close to zero reflecting the dramatic increase in viscosity as decompression proceeds to lower pressures. The large error bars at high quench pressures reflect the broad range of D values exhibited in the sample, interpreted to arise from variations in interbubble spacing and bubble sizes. This range should decrease as the bubbles become more closely packed at lower quench pressures resulting in smaller error bars.

The magnitudes of the shear stress and shear rates calculated for the samples may not reflect the true shear values if the source of deformation is primarily due to coalescence followed by slow bubble relaxation rather than shearing. However, using the relaxation timescale of Toramaru (1995)

$$\tau_r \approx \mu a / \sigma \qquad (11)$$

Where τ_r is the relaxation timescale, μ is the melt viscosity, a is the bubble radius and σ is the surface tension and the input parameters from section 4.1, the relaxation timescale for

a deformed bubble with an equivalent radius of 30 μm is 1.64 s. This will increase at lower pressures as water loss from the melt results in higher melt viscosities and greater melt-vapor surface tension. At 50 MPa with an estimated melt viscosity of $10^{4.1}$ Pas (Hui and Zhang 2006) and surface tension of 0.0866 Nm^{-1}, the relaxation timescale is still short at 4.4s, suggesting that deformed bubbles due to coalescence are expected to relax quickly. Concerns over the applicability of Eq. 11 to the experimental capsule setup were addressed through a set of experiments decompressed at 0.05 MPa/s to 40 MPa and held for up to 600 s before quenching (Table 2.1). If the deformation was due to coalescence, we would expect the deformation parameter to decrease gradually as first small and then larger deformed bubbles relaxed. If the deformation was primarily due to shear, we would expect all bubbles to relax quickly following the end of the shearing. The deformation parameter decreases between 60 and 120 s from 0.24 to 0.09, similar to the value held after the long nucleation timestep, and does not change on increasing the hold time to 600 s. Our interpretation is that bubble relaxation is fast and that the observed deformation does result primarily from melt shear. In the absence of shear, coalesced bubbles will relax quickly, though this bubble relaxation may itself also be a source of local melt shear. Overall, it appears that melt shearing dominates as the source of deformation over the timescales of these experiments. However, the possibility remains that if the relaxation timescale is slower, our results will be skewed by the inclusion of bubbles deformed purely as the result of coalescence.

The effect of bubble deformation in the experimental capsules

The theoretical percolation threshold is ~30 vol. % for a population of spherical bubbles, representing the volume fraction at which a percolating cluster exists across an infinite medium (Sahimi 1994). However, Saar and Manga (1999) and Mueller et al. (2005) observed that gas flowed though a range of natural pumices at lower porosities and proposed that the BSD and the extent of bubble deformation might also strongly influence the permeability of the sample. According to Yi and Sastry (2004), the theoretical percolation threshold drops to ~25 vol. % for a collection of ellipsoids where the aspect ratio=2 and 20 vol. % for an aspect ratio of 3. Mueller et al. (2005) found that pumice with a range of bubble sizes had greater connectivity than those with an equivalent uniform size. In addition, experimental work by Manga and Stone (1994) showed that the rate of coalescence increased with bubble deformation, which would decrease the percolation threshold further.

Accordingly, we might assume that our experimental phonolite samples become permeable between 20-30 vol. % porosities. However, permeability will be low and few bubbles will be connected to external vapor, thereby limiting the degree of degassing that can occur. Extensive permeability is assumed to have developed in these samples only when the sample porosity deviates from equilibrium without a concurrent deviation in dissolved water content. For the phonolite experimental samples this occurs between 40-50 vol. % (Figure 2.2).

Implications for volcanic processes

In summary, the combined set of observations from the K-phonolite experiments indicate that the samples exsolved water in equilibrium into the primary population of bubbles that nucleated during the first decompression step. As the pressure decreased from 100 MPa, the bubbles expanded causing melt shearing, leading to deformation and coalescence. As the pressure decreased to 50 MPa, the proportion of connected bubbles increased, generating extensive connectivity within the sample at vesicularities of 40-50 vol. %. As the bubbles became connected to the external vapor, they lost excess vapor pressure, causing them to degas to the external vapor within the capsule. After degassing, the connected bubbles collapsed, leaving remnant bubble textures (e.g. tails; Figure 2.1) and a significantly decreased sample porosity.

The role of melt shearing in promoting coalescence and degassing may be enhanced in the conduit over that observed in the experimental capsule. In addition to melt shearing from bubble expansion, shearing could also arise due to velocity gradients across the conduit. Assuming a parabolic velocity profile across the conduit, we expect that the degree of deformation particularly near the conduit wall where velocity gradients are steepest would be greater and the porosity at which the percolation threshold and the onset of extensive permeability are reached would be reduced further.

The extent to which the experimental results apply to explosive volcanic settings might be hindered by the low observed maximum experimental porosities compared to natural pumices (Gardner et al. 1996). However, the experimentally derived shear stresses and

shear rates were low at low pressures suggesting that further bubble expansion due to exsolution and/or decompression would result in fewer deformed bubbles and therefore a higher percolation threshold. At 10MPa a completely degassed sample with remaining dissolved water content = 1.15% could theoretically reach a porosity of 91% at 1MPa allowing for equilibrium exsolution and no further degassing. The extent to which experimental studies under conduit conditions can be related to post fragmentation pumice textures is therefore limited. The rapid bubble collapse observed in these experiments on the K-phonolite melt also indicates that post-fragmentation modifications to porosity could be more extensive in alkalic magmas than in rhyolites, since their low viscosities lead to very short melt relaxation timescales. In this case, bubble collapse may result in a significantly reduced vesicularity over a period of minutes at relatively high pressures. If the experiments reflect processes occurring in nature, alkalic magmas erupted at relatively high temperatures near 900 °C are expected to show some features of bubble collapse in the erupted pumice, barring post fragmentation modifications to the vesicle textures.

References

Bagdassarov, N., Dorfman, A. and Dingwell, D.B., 2000. Effect of alkalis, phosphorus, and water on the surface tension of haplogranite melt. American Mineralogist, 85(1): 33-40.

Burgisser, A. and Gardner, J.E., 2004. Experimental constraints on degassing and permeability in volcanic conduit flow. Bulletin of Volcanology, 67(1): 42-56.

Carroll, M.R. and Blank, J.G., 1997. The solubility of H_2O in phonolitic melts. American Mineralogist, 82: 549-556.

Cioni, R., 2000. Volatile content and degassing processes in the AD 79 magma chamber at Vesuvius (Italy). Contributions to Mineralogy and Petrology, 140(1): 40-54.

Cioni, R. et al., 1995. Compositional layering and syn-eruptive mixing of a periodically refilled shallow magma chamber: the AD 79 plinian eruption of Vesuvius. Journal of Petrology, 36(3): 739-776.

Cox, R.G., 1969. The deformation of a drop in a general time- dependent fluid flow. Journal of Fluid Mechanics, 37: 601-623.

Gardner, J.E., Hilton, M. and Carroll, M.R., 1999. Experimental constraints on degassing of magma; isothermal bubble growth during continuous decompression from high pressure. Earth and Planetary Science Letters, 168(1-2): 201-218.

Gardner, J.E., Thomas, R.M.E., Jaupart, C. and Tait, S., 1996. Fragmentation of magma during Plinian volcanic eruptions. Bulletin of Volcanology, 58(2): 144-162.

Gurioli, L., Houghton, B.F., Cashman, K.V. and Cioni, R., 2005. Complex changes in eruption dynamics during the 79 AD eruption of Vesuvius. Bulletin of Volcanology, 67(2): 144-159.

Hui, H. and Zhang, Y., 2006. Toward a general viscosity equation for natural anhydrous and hydrous silicate melts. Geochimica et Cosmochimica Acta, 2007(71): 403-416.

Iacono Marziano, G., Schmidt, B.C. and Dolfi, D., 2007. Equilibrium and disequilibrium degassing of a phonolitic melt (Vesuvius AD 79 "white pumice") simulated by decompression experiments. Journal of Volcanology and Geothermal Research, 161(3): 151-164.

King, P.L., Larsen, J.F., Lui, D.K., Lockard, J., Dalby, K.D. and Griffin,T., 2006. Rapid Analysis of total H_20 and molecular H_2O contents of small geologic glasses using reflectance IR spectroscopy. Geol. Assoc. Canada-Mineral. Assoc. Canada, Abstract 649.

Larsen, J.F., 2006. Experimental study of bubble nucleation in K-phonolite melt, AGU, San Francisco.

Larsen, J.F. and Gardner, J.E., 2000. Experimental constraints on bubble interactions in rhyolite melts; implications for vesicle size distributions. Earth and Planetary Science Letters, 180(1-2): 201-214.

Larsen, J.F. and Gardner, J.E., 2004. Experimental study of water degassing from phonolite melts: implications for volatile oversaturation during magmatic ascent. Journal of Volcanology and Geothermal Research, 134: 109-124.

Lyakhovsky, V., Hurwitz, S. and Navon, O., 1996. Bubble growth in rhyolitic melts-experimental and numerical investigation. Bulletin of Volcanology, 58(1): 19-32.

Manga, M. and Stone, H.A., 1994. Interactions between bubbles in magmas and lavas: effects of bubble deformation. Journal of Volcanology and Geothermal Research, 63: 267-279.

Mangan, M.T., Sisson, T.W. and Hankins, W.B., 2004. Decompression experiments identify kinetic controls on explosive silicic eruptions. Geophysical Research Letters, 31: no.8, 4.

Mourtada-Bonnefoi, C.C. and Laporte, D., 2004. Kinetics of bubble nucleation in a rhyolitic melt; an experimental study of the effect of ascent rate. Earth and Planetary Science Letters, 218(3-4): 521-537.

Mueller, S., Melnik, O., Spieler, O., Scheu, B. and Dingwell, D.B., 2005. Permeability and deagssing of dome lavas undergoing rapid decompression:An experimental determination. Bulletin of Volcanology, 67: 526-538.

Proussevitch, A.A., Sahagian, D.L. and Kutolin, V.A., 1993. Stability of foams in silicate melts. Journal of Volcanology and Geothermal Research, 59(1-2): 161-178.

Rust, A.C., Manga, M. and Cashman, K.V., 2003. Determining flow type, shear rate and shear stress in magmas from bubble shapes and orientations. Journal of Volcanology and Geothermal Research, 122(1-2): 111-132.

Saar, M.O. and Manga, M., 1999. Permeability-porosity relationship in vesicular basalts. Geophysical Research Letters, 26(1): 111-114.

Sahimi, M., 1994. Applications of percolation theory. Taylor & Francis, 258 pp.

Sheridan, M.F., Barberi, F., Rosi, M. and Santacrose, R., 1981. A model for Plinian eruptions of Vesuvius. Nature, 289: 282-285.

Taylor, G.I., 1932. The viscosity of a fluid containing small drops of another fluid. Proceedings of the Royal Society of London, A, 138: 41-48.

Taylor, G.I., 1934. The formation of emulsions in definable fields of flow. Proceedings of the Royal Society of London, A, 146: 501-523.

Toramaru, A., 1995. Numerical study of nucleation and growth of bubbles in viscous magmas. Journal of Geophysical Research, B, Solid Earth and Planets, 100(2): 1913-1931.

Whittington, A., Richet, P., Linard, Y. and Holtz, F., 2001. The viscosity of hydrous phonolites and trachytes. Chemical Geology, 174: 209-224.

Wömer, G. and Schmincke, H.-U., 1984. Petrogenesis of the zoned Laacher See tephra. Journal of Petrology, 25: 836-851.

Woods, A.W. and Koyaguchi, T., 1994. Transitions between explosive and effusive eruptions of silicic magmas. Nature, 370(6491): 641-644.

Yi, Y.-B. and Sastry, A.M., 2004. Analytical approximation of the percolation threshold for overlapping ellipsoids of revolution. Proceedings of the Royal Society of London, A, 460: 2353-2380.

Acknowledgements

This study was supported by the National Science Foundation, Canadian National Science and Engineering Research Council and the Canadian Foundation for Innovation. We thank Lucia Gurioli for the Vesuvius K-phonolite pumice used as starting material.

The manuscript was improved by the constructive comments of Jim Gardner, Tom Sisson and two anonymous reviewers.

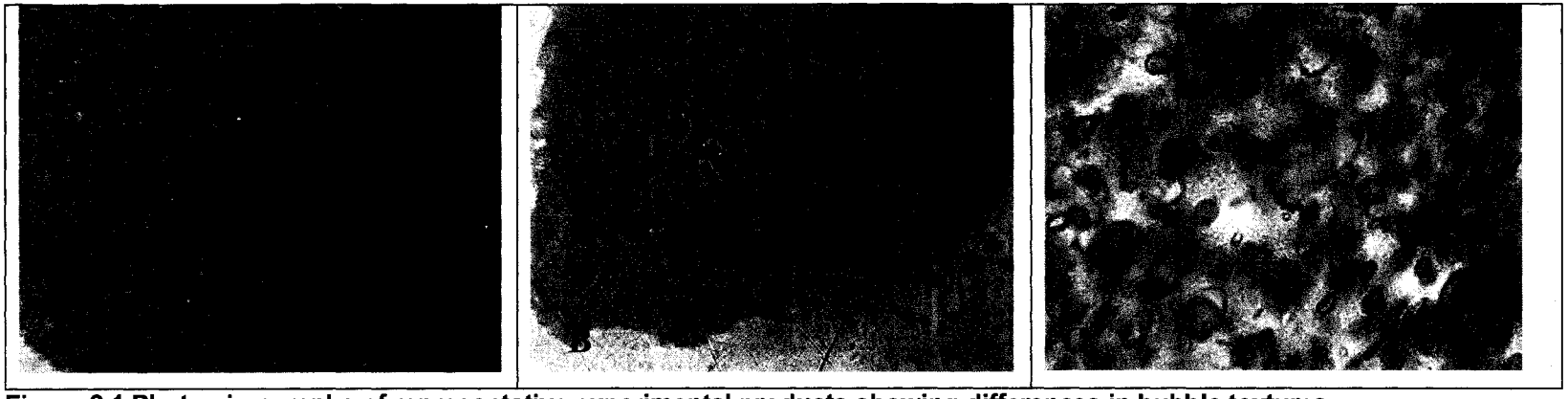

Figure 2.1 Photomicrographs of representative experimental products showing differences in bubble textures.
(A) Experiment quenched at 50 MPa shows high degree of connectivity through linearly deformed, partially coalesced bubble chains. (B) Experiment quenched at 10 MPa shows low connectivity with exhibited textures attributable to various stages of bubble collapse. There are large isolated deformed bubbles, bubble relics in the form of tails and large bubble free areas assumed to derive from complete bubble collapse. (C) Experiment quenched at 80 MPa and imaged using transmitted light shows bubbles deformed into approximate ellipses.

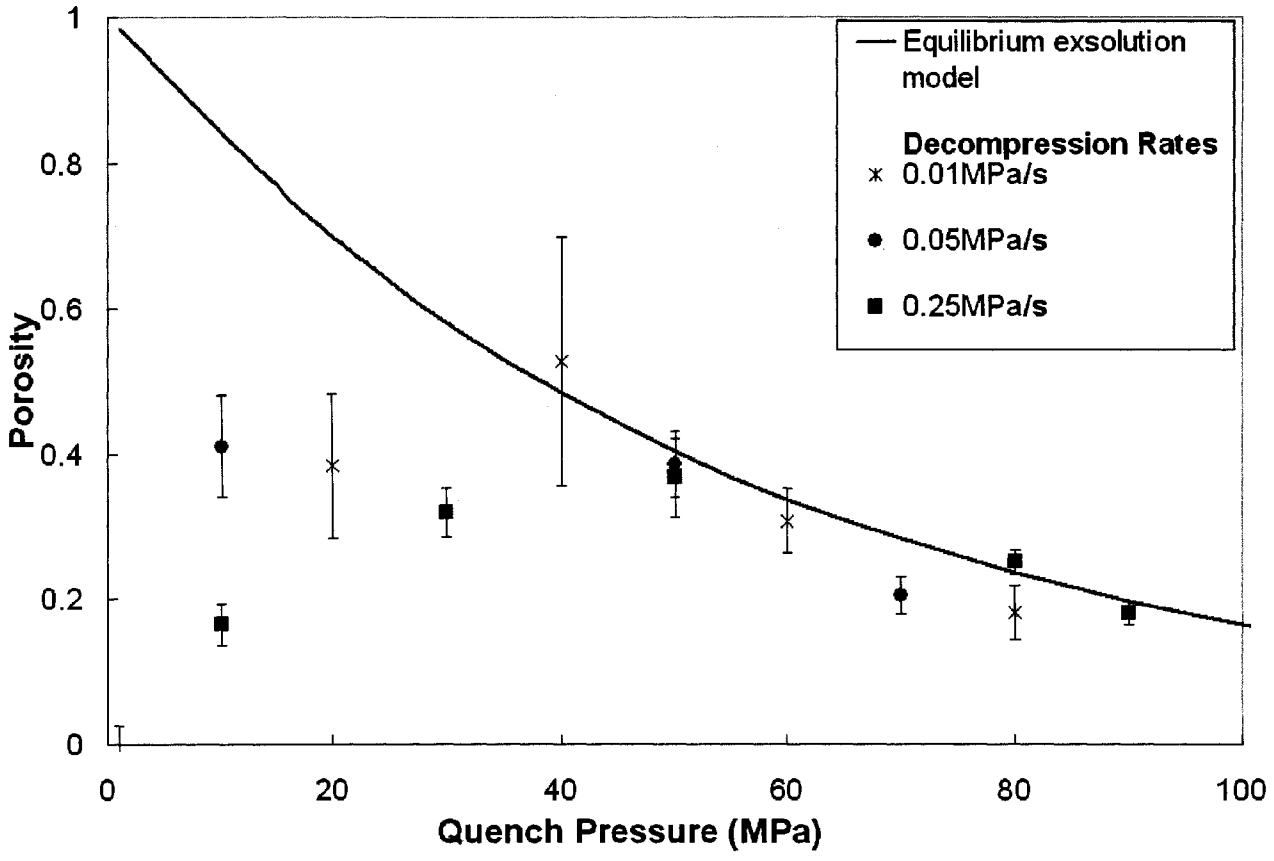

Figure 2.2 Porosity versus quench pressure for three constant decompression rates.
The solid line indicates equilibrium exsolution porosities calculated using the equation of Gardner et al. (1999) and an experimentally derived solubility curve (Table 2.1). Equilibrium exsolution is observed for all rates down to a quench pressure of 40 MPa. Below 40 MPa, porosities are lower than the expected equilibrium values. Error bars are 1σ standard deviation.

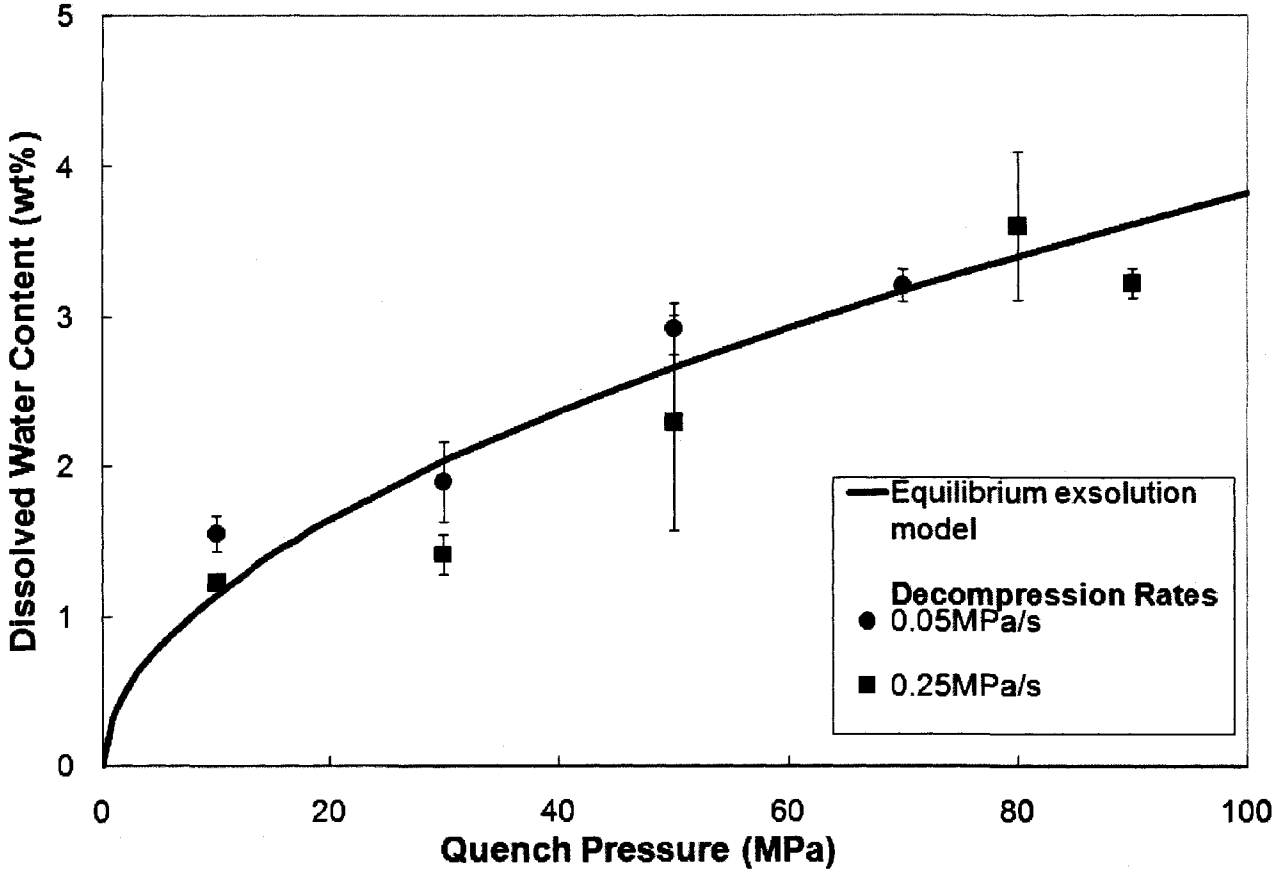

Figure 2.3 Total dissolved water concentration versus quench pressure.
Water concentrations obtained from micro-reflectance FTIR analyses. The solid curve is water solubility in phonolite glass determined from best fit of solubility data using the same technique (Table 2.1). Error bars are 1σ standard deviation

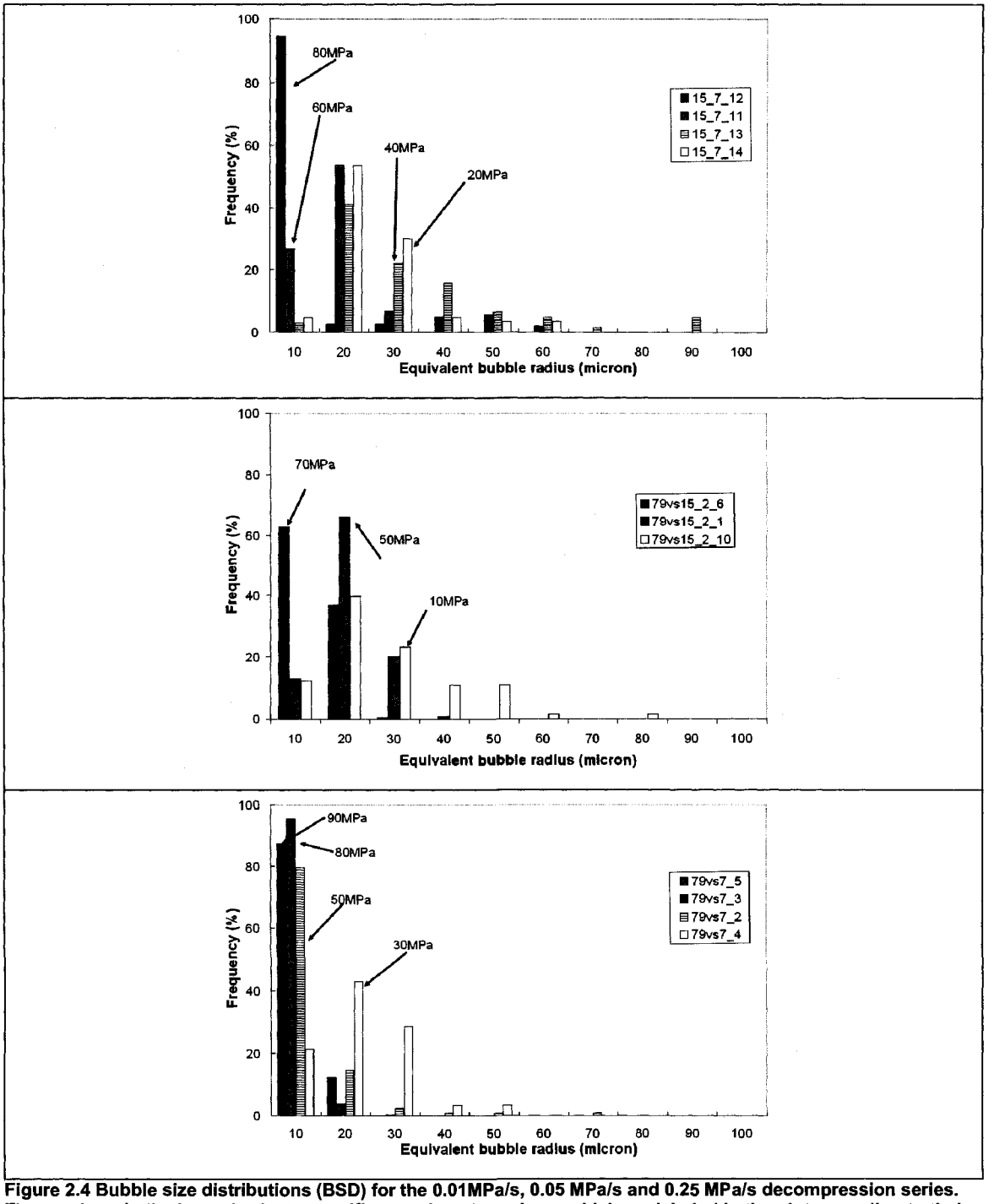

Figure 2.4 Bubble size distributions (BSD) for the 0.01MPa/s, 0.05 MPa/s and 0.25 MPa/s decompression series. The numbers in the legend refer to specific experiment numbers, which are labeled in the plot according to their final pressures. (A) Bubble size distributions (BSD) for the 0.01MPa/s decompression series. (B) Bubble size distributions (BSD) for the 0.05MPa/s decompression series. (C) Bubble size distributions (BSD) for the 0.25MPa/s decompression series. in each series, the size distributions broaden and bubble sizes increase, primarily due to growth and maturation of the population (ripening and/or coalescence).(C) shows a backtracking to smaller bubble sizes, reflecting the collapse of bubbles at low pressures (Figure 2.2).

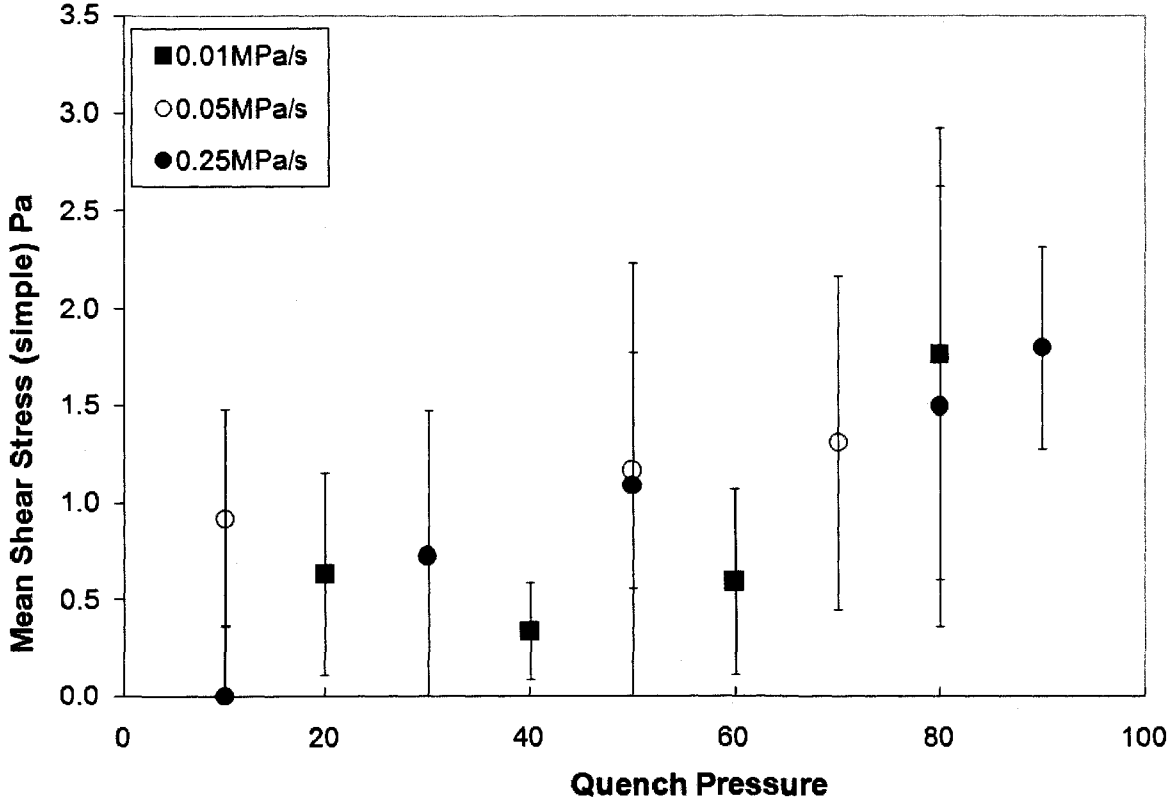

Figure 2.5 Calculated mean shear stress, assuming simple shear, as a function of quench pressure. Error bars are 1 deviation

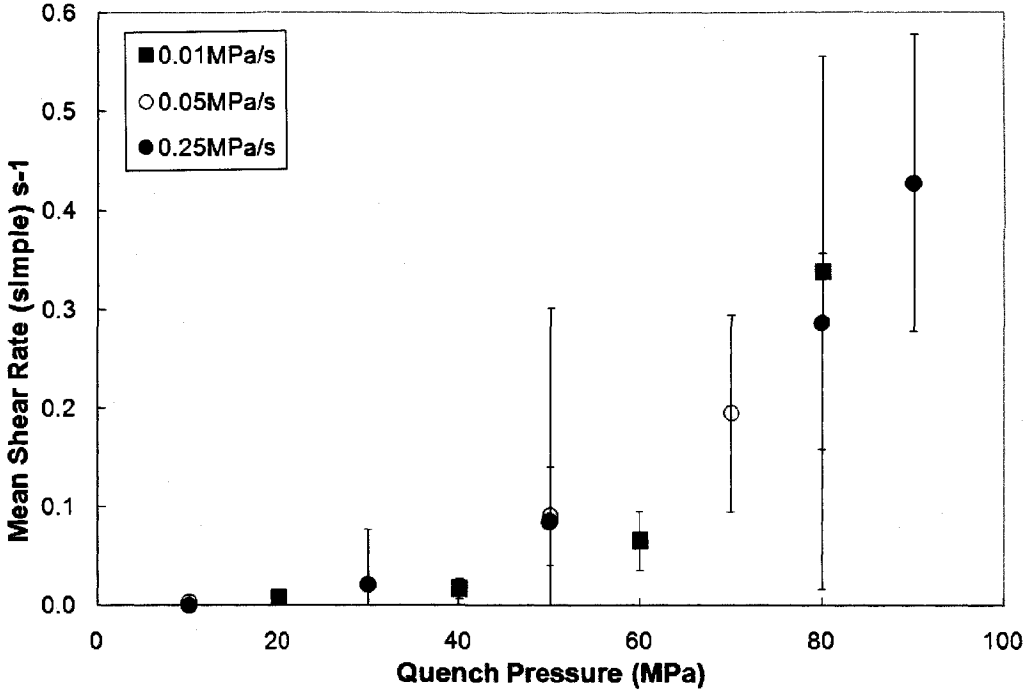

Figure 2.6 Calculated mean shear rate, assuming simple shear, as a function of quench pressure.
Error bars are 1 standard deviation. This figure shows how the calculated shear rate drops as decompression proceeds to lower pressures. This most likely reflects increasing meit viscosities as water is lost via exsolution during decompression. Calculated viscosities as a function of quench pressure assuming equilibrium dissolved water concentrations using model of Hui and Zhang (2006).

Table 2.1 Bubble population and melt properties for decompression experiments.

Decompression Runs[a]	Mass (mg)	dP/dt ($MPas^{-1}$)	P_{Final} (MPa)	Time at P_{Final} (s)	Porosity (Vol%)[b]	Total H2O (Wt%)[c]	D[d, b]	rMean (μm)[e, b]	# bubbles[f]	N_V[g, b] ($x10^7 cm^{-3}$)
79VS7_6	11.2	-	100	-	13.7(2.1)	-	0.09(0.06)	8(12)	39	6.7(1.9)
79VS15_2_6	22.6	0.05	70	-	20.5(2.6)	3.2(0.1)	0.18(0.12)	10(11)	209	4.0(3.2)
79VS15_2_1	14.3	0.05	50	-	38.6(2.5)	2.9(0.2)	0.24(0.13)	18(19)	124	1.4(1.3)
79VS15_2_12	8.4	0.05	30	-	-	1.9(0.3)	-	-	-	-
79VS15_2_10	18.9	0.05	10	-	41.0(3.2)	1.6(0.1)	0.24(0.14)	30(38)	73	0.3(0.2)
79VS7_5	17.5	0.25	90	-	18.1(0.7)	3.2(0.1)	0.20(0.13)	7(10)	167	9.6(4.5)
79VS7_3	26.0	0.25	80	-	25.1(1.1)	3.6(0.5)	0.14(0.11)	7(10)	296	18.0(5.4)
79VB15_2_12_3_4	6.3	0.25	80	-	27.7(1.6)	-	0.14(0.12)	6(6)	79	20.8(21.0)
79VS7_2	27.3	0.25	50	-	36.8(0.8)	2.3(0.7)	0.21(0.14)	17(30)	108	1.7(0.3)
79VS7_4	9.6	0.25	30	-	31.9(2.6)	1.4(0.1)	0.16(0.08)	22(28)	28	0.7(0.3)
79VB15_2_12_3_6	15.2	0.25	30	-	30.6(6.1)	-	0.15(0.11)	14(17)	51	2.8(1.5)
79VS1_4	12.4	0.25	10	-	16.5(3.1)	1.2(0.0)	-	-	-	-
79VS15_7_12	22.1	0.01	80	-	18.2(4.5)	-	0.19(0.13)	8(13)	148	8.7(1.8)
79VS15_7_11	19.7	0.01	60	-	30.8(1.7)	-	0.17(0.14)	24(32)	145	0.5(0.2)
79VS15_7_13	16.3	0.01	40	-	52.7(11.5)	-	0.14(0.1)	39(51)	63	0.2(0.1)
79VS15_7_14	10.5	0.01	20	-	38.3(6.6)	-	0.15(0.13)	26(32)	170	0.4(0.2)
Solubility Runs										
JL_79VS1	-	-	200	-	-	5.5(0.1)	-	-	-	-
JL_79VS7	-	-	150	-	-	4.7(0.1	-	-	-	-
JL_79VS8	-	-	125	-	-	4.6(0.1)	-	-	-	-
JL_79V1	-	-	75	-	-	3.4(0.2)	-	-	-	-
JL_79VS10	-	-	50	-	-	3.0(0.1)	-	-	-	-
Time Series										
79VB_8_3	11.9	0.05	40	60	23.2(3.3)	-	0.25(0.12)	14(18)	95	1.9(1.0)
79VB15_7_15	5.7	0.05	40	120	27.6(7.6)	-	0.11(0.07)	20(29)	51	0.8(0.3)
79VB8_4	8.0	0.05	40	600	21.2(6.9)	-	0.11(0.10)	19(26)	51	0.7(0.3)

Notes

[a] All experiments carried out at 880°C. Samples first hydrated at 200MPa for 7 days prior to decompression.

[b] 1σ standard deviation of all measurements are given in parentheses.

[c] Water contents were determined using micro-reflectance FTIR.

[d] D-Deformation parameter. See text for description.

[e] Mean bubble radius (r) is a volume weighted mean derived from the mean bubble volume.

[f] Total number of bubbles measured in each quenched experiment.

[g] N_V-Bubble number density

Chapter 3 Experimental Constraints on Degassing and Collapse of Highly Vesicular Rhyolite[2]

Abstract

This study presents experimental results on a natural rhyolite melt decompressed, (after a rapid pressure drop from 150 MPa and holding time of 30 minutes) at a slow rate (0.01 MPa/s) from 100 MPa and then held at 10 MPa for up to 900 s. The resultant vesicular rhyolite formed a high-porosity interconnected network, which then degassed over a very short timescale (~120 s), resulting in an almost bubble free melt after vesicle collapse. The degassing behavior occurs in two distinct phases. During Stage I degassing, the porosity of the interconnected, highly vesicular network decreases and the bubble size distribution (BSD) evolves from an initially unimodal population to one that includes a distinct population of much larger bubbles that form an interconnected network between large and small pores. During Stage II, this network collapses with attendant abrupt degassing. In comparison with other experimental datasets, the experiments highlight the critical parameters controlling the formation and stability of a highly vesicular magma: bubble number density, bubble size distribution and porosity. The results lead to quantification of the pre-collapse degassing rate (Stage I, from 1.7×10^{-2} to 5.9×10^{-3} s^{-1} per unit melt volume) and a proposed coalescence-induced coalescence model which may explain the rapid destabilization and collapse of the vesicular network, and the dramatic change in BSD over a timescale of minutes. During a coalescence event, forces

[2] Joanna Mongrain and Jessica F. Larsen submitted to Bulletin of Volcanology, in review

accompanying shape relaxation induce a change in the local melt velocity field. In a highly vesicular, close packed arrangement of bubbles with inter-bubble film thicknesses close to the critical value, this perturbation triggers a cascade of coalescence events creating large vugs, which weaken and destabilize the vesicular sample leading to rapid collapse. The estimated timescale is of the order of 4 minutes compared to 10^4 minutes estimated for binary coalescence based on prior studies. The attendant Stage II degassing rate is 5.0×10^{-2} s^{-1} per unit melt volume. In summary, these results allow quantification of the degassing rate of an interconnected bubble network and the timescale over which a crystal-poor rhyolite magma with >70 vol. % porosity becomes destabilized and experiences total collapse of its porous structure. We propose a new model that describes the rate of rapid volatile release and magmatic foam collapse at shallow levels in a volcanic conduit, and the timescale for the formation of degassed plugs of magma from slowly ascending rhyolite magmas.

Keywords: Bubble Growth, Coalescence, Degassing, Experiments, Rhyolite, Foam, Permeability.

Introduction

Understanding the transition between effusive and explosive volcanism is a major focus of volcanology research. Effusive eruptions result from efficient removal of the vapor phase from the magma and conduit system during magmatic ascent (Jaupart and Allegre 1991; Taylor et al. 1983). The timescales over which magma can exsolve water vapor and

degas at shallow depths holds critical implications for the resulting eruptive mechanism (Eichelberger 1995; Eichelberger et al. 1986; Westrich et al. 1988).

Three distinct shallow magmatic degassing mechanisms have been proposed. Most prominent is the permeable foam model (Blower et al. 2001; Burgisser and Gardner 2004; Eichelberger et al. 1986; Westrich and Eichelberger 1994), which proposes the onset of wide scale permeability above a porosity threshold for vesicular magma at shallow depths in a conduit. Coupled with permeable conduit walls, this mechanism is used to describe the transitions between explosive and effusive volcanism (Eichelberger et al., 1986). The proposed permeability threshold varies between 40 to 80 vol. %, depending on the study (40 vol. %: Burgisser and Gardner, 2004; 60-70 vol. %: Westrich and Eichelberger 1994; 45-80 vol. %: Takeuchi et al. 2005). An alternative model contends that degassing is a continuous process, with permeability remaining proportional to porosity for all vesicularities (Klug and Cashman 1996; Klug et al. 2002). Modifications to these models arise due to bubble alignment and coalescence (Saar and Manga 1999; Takeuchi et al. 2005). Gas loss from the conduit itself may be assisted by fractures in the conduit walls and overlying edifice (Heiken et al. 1988; Jaupart 1998; Jaupart and Allegre 1991). Recent studies have proposed a third mechanism where magma auto-brecciation along the conduit walls leads to bubble wall fracture and degassing through the formation of a highly permeable fracture network (Gonnerman and Manga 2003; Rust et al. 2004; Tuffen et al. 2003). Evidence for degassed silicic magmas exists in the dense obsidian found in the centre of volcanic domes (Fink et al. 1992) and degassed magmatic plugs in conduits that are thought to lead to Vulcanian-style

explosions (Cashman and McConnell 2005; D'Oriano et al. 2005; Hammer et al. 1999; Taddeucci et al. 2004). Thus, the timescales of permeability development in volcanic conduits are closely tied with eruption mechanism, and is a critical component to our understanding of eruptive mechanisms.

This study documents the experimental creation of an interconnected, highly vesicular rhyolite from a H_2O-saturated rhyolitic melt after decompression to 10 MPa. The results of the study are compared to previous experimental studies on coalescence in rhyolitic melts (Burgisser and Gardner 2004; Gardner 2007) in order to expose the critical parameters driving the formation of an interconnected bubbly network, and its subsequent destabilization and collapse. Sample collapse is proposed to result from reduced network strength due to changes in bubble size distribution (BSD), attributed to coalescence. The binary coalescence model alone (Proussevitch et al. 1993) is too slow to explain the dramatic changes observed in the experiments. A coalescence-induced coalescence model is applied, originally proposed by Martula et al. (2003) and McGuire et al. (1996) to describe a cascading coalescence process for dispersed droplets in a viscous polymer matrix (McGuire et al. 1995; Tanaka 1994). This model fits well with the experimental observations of rapid sample collapse, following limited binary coalescence. The implications of the findings of this study for the mechanisms of explosive and effusive eruptions are also discussed.

Experimental and Analytical Methods

Decompression experiments were performed using slabs of Mono Craters obsidian saturated with de-ionized water at 150 MPa and 825 °C for 5 days in Rene-style, cold-seal pressure vessels and quenched with compressed air and water submersion. This timescale ensured that the slabs were uniformly H_2O saturated (Mangan and Sisson 2000). The H_2O saturated glasses were sectioned into 5 by 3 mm slabs, re-loaded into 4 mm diameter Ag or Au tubes with ~5 wt. % de-ionized water and held at the starting conditions in rapid-quench capable cold-seal vessels (Gardner et al. 1999) for 30 minutes before decompressing rapidly to 100 MPa and holding for 30 minutes initiating bubble nucleation and growth. After 30 minutes the nucleated bubbles should have gas contents in equilibrium with the melt, relative to the solubility of water in the rhyolite melt at those conditions. The experiments were decompressed stepwise at an average decompression rate of 0.01 MPa/s and then held at a final pressure of 10 MPa for 15-900 seconds prior to rapid quenching. The samples were quenched to the glass transition within ~2 seconds, by pulling the experiments down into a water-cooled jacket using a magnet (Gardner et al. 1999; Lyakhovsky et al. 1996). The decompression rate was chosen to ensure that equilibrium exsolution was maintained during decompression (Gardner et al. 1999) so that the experimental set would document only coalescence and degassing as a function of time at low pressures. An additional experiment was decompressed to 30 MPa and held for 900 s for comparison. The samples were sectioned and polished for imaging. Digital images of high porosity samples were acquired using an ISI-SR-50 Scanning Electron Microscope (SEM) in the Advanced Instrumentation

Laboratory (AIL) and the University of Alaska Fairbanks (UAF). The images were collected using the optimum accelerating voltage, current and magnification required to ensure good image resolution for each sample. All other images were acquired using a petrographic microscope with an attached camera. The images were analyzed using the ImageJ program to determine bubble size distributions and porosities. The bubble radii reported from analysis of the SEM images are not the true bubble radii but the intersected bubble radii. Bubble number densities per unit melt volume, N_v^m were calculated using Eq. (1) where N_v^b is the bubble number density as calculated in Gardner et al. (1999)

$$N_v^m = \frac{N_v^b}{1-\phi} \tag{1}$$

Experimental Results

After decompression to 10 MPa and a hold time of 15 seconds, experiment mc1_b15_5 revealed a high porosity, interconnected vesiculated sample with relatively uniform bubble sizes (Figure 3.1). Connected pathways between bubbles can be seen in the SEM image of this sample (Figure 3.1) as much darker areas at the base of the curved bubble walls. Figure 3.2 shows that the sample held for 30 seconds also became highly porous, and is marked by the striking appearance of large vugs dispersed amongst a smaller, qualitatively uniform size bubble population. Figure 3.3 and Figure 3.4 show representative chunks collected from the sample held for 60 s. In Figure 3.3, a high porosity chunk with small bubbles adjacent to a much larger vug appears to be very

similar to the 30 s, mc1_b15_4 experiment (Figure 3.2). By contrast, Figure 3.4 shows a chunk of much lower porosity containing only a few deformed bubbles from the same experiment mc1_b16_3 (Table 3.1). Stringy textures, which may be relict bubble walls, are distributed throughout this piece of the 60 second experiment. The experiment mc1_b14_6 held for 120 seconds contains only a few deformed bubbles, and has low overall porosity (Figure 3.5). After 300 seconds, the recovered experiment was fragmental (Figure 3.6). The individual fragments are mostly bubble free with reverse curved edges, indicating the prior presence of large bubbles with approximate radii of ~60 μm. After 900 s, the experiment is virtually bubble free (Figure 3.7). As in Figure 3.6, edges of the experiment are reversely curved and suggest the prior presence of larger bubbles with radii estimated to be around 55 μm. In contrast, the experiment held for 900 seconds at 30 MPa shows a large population of similar sized bubbles evenly distributed throughout the sample (Figure 3.8).

The BSD's from the decompression experiments illustrate changes in bubble sizes with time at 10 and 30 MPa (Figure 3.9; Table 3.1). After 15 s, the BSD is narrow with a mean bubble size of 13.7(3.6) μm. After 30 s, the BSD is similarly centered on a mean bubble size of 15.1(8.3) μm with the majority of the bubbles within a narrow range. The larger standard deviation reflects the presence of large vugs (>45 μm in radius; Figure 3.2) with the population dominated mostly by small bubbles. After 60 s, the BSD for the high porosity experiment is again narrow but centered on a lower mean bubble radius of 7.6(2.7) μm. After 120 s, the BSD is still relatively narrow and centered around 12.1(6.3) μm. The BSD for the sample decompressed to 30 MPa is included for comparison with a

mean bubble radius of 7.0(3.4) μm. Here, the narrow BSD is indicative of limited coalescence.

Figure 3.10 illustrates how the porosities of each experiment change over the experimental time series at a final pressure of 10 MPa. Sample mc1_b15_5 has a porosity of 72.5(1.6) vol. %, after 15 s. The porosity is less than that expected from equilibrium exsolution (~78 vol. %) and on holding for a further 15 seconds the porosity drops to 66.1(0.8) vol. % in experiment mc1_b15_4, with the majority of the bubbles of similar size to the 15 s sample (Figure 3.9). After 60 s, two distinct textures are visible. Highly vesicular regions have an average porosity of 60.2(6.3) vol. %, while other regions have average porosities of 15.8(1.8) vol. % and contain only a few deformed bubbles. After 120 s, the sample porosity is still heterogeneous, ranging between 13.8(3.4)-46.8(4.7) vol. % though no regions with high vesicularity are seen. There is almost no observed porosity (≤2 vol. %) remaining after 300 s and 900 s.

In general, bubble number densities (N_v^m) within the experiments held at 10 MPa decreases over time from 3.82(0.11) x10^9 cm^{-3} after 15 s to 1.11(0.32) x10^9 cm^{-3} after 120 s (Table 3.1). After 60 s, one high vesicularity part of experiment mc1_b16_3 has a N_v^m of 7.46(0.50) x10^9 cm^{-3} but this does not reflect the average N_v^m for the sample as other portions have visibly fewer measurable bubbles. Samples held for >120 s have such low porosity and so few bubbles that calculation of the bubble number density is not possible.

Discussion

This study compliments the prior coalescence studies of Larsen et al. (2004), Gardner (2007) and Burgisser and Gardner (2004). At porosities above 40-45% samples from Burgisser and Gardner (2004) showed evidence of degassing and the bubble population had evolved from a population of small spherical bubbles at higher quench pressures to the majority of bubbles being highly deformed and elongated. This change in bubble textures was accompanied by an order of magnitude decrease in N_v^b (not corrected to melt volume) from ~10^6 cm^{-3} and was attributed to coalescence. In contrast, in the recent experiments of Gardner (2007) the bubbles remain spherical even up to porosities of >70 vol. %. N_v^b does decrease with decreasing pressure from ~ 10^7 cm^{-3} to 10^6 cm^{-3} but the dramatic changes observed in the Burgisser and Gardner (2004) experiments are not reproduced in those experiments. Gardner (2007) suggests that the difference in behavior can be attributed to a higher initial N_v^b generating a bubbly melt which does not deform as easily as was the case in the experiments with lower N_v^b, and thus coalescence is delayed compared to the Burgisser and Gardner (2004) study.

In this study, the experiments early in the time series had N_v^m of >10^9 cm^{-3} and therefore represent perhaps another point on the trend, whereby a higher initial bubble number density leads to further delayed coalescence. In particular, a high porosity structure results from the decompression stage, and it undergoes little initial coalescence. This indicates that the initial N_v^m exerts a strong control on the attainment of high porosity and coalescence behavior, where a high initial N_v^m appears to favor high porosity and cause a delay in coalescence during decompression. The higher N_v^m leads to increased

competition for volatiles and leads in turn to a narrow BSD. Thus, a largely unimodal bubble population results, which resists early coalescence as there are negligible internal pressure differences between the bubbles by virtue of their similar sizes (Proussevitch et al. 1993). Without coalescence and early degassing, the growing bubbles are forced to form a close packed arrangement, given the high (>70 vol. %) equilibrium porosity attained at 10 MPa final pressure. In contrast, the Burgisser and Gardner (2004) study represents the other end of the spectrum, exhibiting low initial N_v^b and strong coalescence from the start of decompression, leading to early degassing of the experiments at relatively high pressures (30 MPa). The Burgisser and Gardner (2004) experiments also had much broader BSD than this study, favoring the creation of large bubbles through coalescence, since the internal pressure differences between disparate sized bubbles would be higher.

The Larsen et al. (2004) study focused on changes in bubble number density and sizes after decompression and holding at pressures of 40-75 MPa. Since the experiments were saturated at lower pressures than this study or the studies of Burgisser and Gardner (2004) and Gardner (2007) and never reach the ~40-45 vol. % degassing porosity threshold, the observed decrease in bubble number density is not due to sample degassing but to coarsening of the bubble population. The experimental samples had initial N_v^b's of $\sim 10^8$ cm^{-3}, similar to the Gardner (2007) study. However, the starting material was powdered obsidian and the saturation hold time was insufficient to remove all resulting hydration bubbles. Therefore, although the Larsen et al. (2004) study had a high bubble

number density that would have resulted in a narrow BSD, the hydration bubbles engender a broader size distribution.

Estimation of Experimental Degassing Rates

Since the total timescales of decompression and holding at the final pressures fall well within the range that is marked by equilibrium exsolution rhyolite melts (Gardner et al., 1999), we expect that the experimental series decompressed at 0.01 $MPas^{-1}$ also exsolved water in equilibrium, since growth at slow decompression rates should only be inhibited in rhyolite melts at much cooler temperatures and higher viscosities (Navon and Lyakhovsky 1998). Therefore, the marked drop in the experimental porosities from the near equilibrium values of 72 vol. % to < 2 vol. % seen in Figure 3.10 indicates that the experiments became permeable and document varying stages of degassing along the experimental time series (Table 3.1). Although the experimental capsules clearly represent a closed system, the internal bubble pressure is greater than the melt/capsule pressure. Therefore, as the sample becomes permeable, we would still expect degassing to occur. The degassing behavior occurs in two distinct phases. During Stage I degassing, the porosity of the interconnected highly vesicular network decreases and the BSD evolves from an initially unimodal population to one that includes a peak that represents a distinct population of much larger bubbles (Figure 3.9). Visual evidence for early connectivity indeed exists in Figure 3.1, where dark circular regions seen within the bases of the curved bubble walls show the passageways into the next bubbles residing beneath the surface. During Stage II, the network between large and small pores collapses during an abrupt degassing event. From the porosity results with time, we can calculate

the rate of degassing for each stage, Q per unit melt volume over time using Eq. (2) where ϕ_f and ϕ_i are the final and initial porosity and t_f and t_i are the final and initial times held for at 10 MPa.

$$Q = \frac{\left(\frac{(\phi_i - \phi_f)}{1 - \phi_i}\right)}{t_f - t_i} \qquad (2)$$

Assuming that the vesicular sample started with equilibrium porosity at 0 seconds, the average degassing rates during Stage I are 1.7×10^{-2} s^{-1} per unit melt volume (between 0 and 15 s) falling to 1.5×10^{-2} s^{-1} between 15 and 30 s and 5.9×10^{-3} s^{-1} between 30 and 60 s (using the high porosity regions from the mc1_b16_3 experiment). The low porosity "degassed" regions of the mc1_b16_3 experiment yield an average Stage II degassing rate of 5.0×10^{-2} s^{-1}. The Stage I degassing rate appears to be strongly correlated to the porosity, with the average degassing rate of a sample with 66 vol. % porosity being 1/3 that of a highly vesicular sample with 72.5 vol. % porosity. In contrast, the experiment held at 30 MPa for 15 minutes retains an equilibrium porosity of ~42 vol. %, suggesting that porosities greater than that are required for rhyolite magmas to reach the permeability threshold and degas. These results are in line with a previous experimental study, which concluded that bubble connectivity requires porosities to reach 45-80 vol. % (Takeuchi et al. 2005).

Stage I- Degassing and Coalescence

During Stage I degassing, the BSD evolves from a unimodal distribution of small bubbles (~15 μm) to an approximately bimodal distribution incorporating vugs of order ~45 μm. This is accompanied by a general decrease in N_v^m and most probably reflects coalescence processes. Ostwald ripening is unlikely to be responsible for most of the reduction in N_v^m since the majority of bubbles are still of similar size, and therefore have similar internal pressures.

Bubble coalescence in low porosity systems (<74 vol. %) has been described by a binary coalescence model (Proussevitch et al. 1993), where capillary forces drive melt from the inter-bubble films into the plateau borders. When the film reaches a critical thickness, h_{cr}, the bubbles coalesce. The initial film thickness can be estimated using Eq. (3) (Proussevitch et al. 1993) assuming cubic close packing of bubbles where δ_f is the initial film thickness, r is the average bubble radius and ϕ is the porosity.

$$\delta_f = 2R\left[\left(\frac{0.74}{\phi}\right)^{\frac{1}{3}} - 1\right] \tag{3}$$

The average initial film thickness for the sample held for 15 s with average bubble radius of 13.7 μm and porosity of 72.5 vol. % is 0.19 μm. However, estimating the critical thickness needed to induce coalescence through capillary drainage is much more difficult.

Proussevitch et al. (1993) approximated the critical thickness in their experiments as the typical crystal size. However their thicknesses, 0.1-0.05 mm, are much greater than the experimental film thicknesses we observe and are even bigger than our bubble sizes. We assume in the following calculations that the critical thickness is 90% of the average film thickness for the sample at 72.5 vol. % porosity. The binary coalescence model Proussevitch et al. (1993) provides an estimate of the maximum stability time for a film between two bubbles with initial film thickness of δ_f and a critical rupture thickness of δ_{cr}, Eq. (4).

$$\tau_f = \frac{3\eta R^3}{4\sigma}\left(\frac{1}{\delta_{cr}^{\,2}} - \frac{1}{\delta_f^{\,2}}\right) \tag{4}$$

At 10 MPa and 825 °C, using a surface tension, σ, of 0.22 Nm^{-1} (Bagdassarov et al. 2000) and viscosity of $10^{7.3}$ Pa s (Hui and Zhang 2006), the maximum film stability timescale between two 13.7 μm radii bubbles is ~ 1.9×10^4 minutes, assuming δ_{cr}=90 % of δ_f and δ_f is 0.19 μm. Decreasing the estimate for δ_{cr}, increases the film stability time. As the predicted coalescence timescales are ~4 orders of magnitude longer than the 1 to 2 minutes over which the experimental sample BSD's evolved prior to sample collapse, binary coalescence alone cannot be responsible.

Coalescence-induced coalescence (Martula et al. 2003; McGuire et al. 1996) arises when the coalescence of inviscid droplets within a polymerized medium perturbs the medium velocity field, causing a cascade of further coalescence events as droplets within the

medium collide into one another and coalesce. This process can lead to rapid separation of the droplet phase, as observed by McGuire et al. (1995) and Tanaka (1994). Whilst the experiments that first observed this phenomenon involved much lower viscosities than that of a silicate melt, the equations shown below which govern the behavior are not experimentally derived, but model fluid flow arising from bubble coalescence by a "ring of sources" approach (McGuire et al. 1996). They may thus be used to understand the role this mechanism might play in bubble coalescence within high porosity magmas.

Consider the simple binary coalescence of two bubbles. At the instant that the inter-bubble film ruptures, the newly coalesced bubble is irregularly shaped with a neck of width $2r_0$ (Figure 3.11). Fast relaxation of the new bubble is driven by the large pressure difference across the bubble-melt interface, imparted by the large radius of curvature at the neck (McGuire et al. 1996). This fast relaxation induces a localized flow in the surrounding melt which moves bubble **A** (Figure 3.11) away from the coalescing bubbles. This process is not related to the overall time taken for a deformed bubble to become spherical in the absence of a shear stress (Lyakhovsky et al. 1996) where relaxation is driven by pressure gradients along the entire bubble surface, but the much faster timescale over which the inter-bubble melt is forced out due to negative curvature at the neck. The pressure difference driving the melt may be calculated using Eq. (5) (McGuire et al. 1996), where ΔP is the pressure difference across the film, σ is the surface tension and h_{cr} is the critical thickness:

$$\Delta P = \frac{\sigma}{h_{cr}} + \frac{\sigma}{2R} \tag{5}$$

During the coalescence of two 13.7 μm bubbles with a critical thickness of 90 % of the average initial film thickness of 0.19 μm and surface tension of 0.22Nm^{-1} (Bagdassarov et al. 2000), ΔP is 0.2 MPa. The time taken for the inter-bubble fluid to be expelled t_c may be calculated using Eq. (6) where η, σ, h_{cr} are as above and r_0 is half the width of the inter-bubble boundary (See Figure 3.11) prior to coalescence:

$$t_c = \frac{3\eta R^2}{h_{cr}\sigma}\left[1 - \left(\frac{r_0}{R}\right)^2\left(1 + 2\ln\frac{R}{r_0}\right)\right] \tag{6}$$

$$\tau = \frac{R\eta}{\sigma} \tag{7}$$

Using values for R, η, σ and h_{cr} as above and a ratio of r_0/R of 0.98, the time for complete melt expulsion is 4.0 minutes. A decrease in the r_0/R ratio to 0.95 increases the melt expulsion time to 24.8 minutes. Inspection of Eq. (6) reveals that an increase in melt viscosity or decrease in surface tension will increase the melt expulsion time as expected. By comparison, the time taken for the newly formed bubble to become spherical can be calculated using Eq. (7) (Lyakhovsky et al. 1996), and is 26 minutes for a bubble with a radius of 17.3 μm, arising from the coalescence of two bubbles with radii of 13.7 μm.

Inter-bubble melt expulsion may have little effect in a widely dispersed bubble population. However, within a close-packed polyhedral arrangement as shown in Figure 3.11 where most of the inter-bubble films are close to their critical thickness, a perturbation in the melt velocity field caused by a few coalescing bubbles could cause a cascading set of coalescence events. As bubble **A** is repelled away from the coalescing bubbles, the films between bubble **A** and adjacent bubbles (**B** and **C** in Figure 3.11) thin. Since the interbubble films are close to their critical thicknesses prior to the movement of bubble **A**, this change may result in film rupture and coalescence of bubbles **A**, **B** and **C**. Expulsion of the melt between these coalescing bubbles could lead to further film ruptures between neighboring bubbles, resulting in the rapid formation of a few large cavities, with diameters that are incompatible with simple binary coalescence of two much smaller bubbles. Creation of the large vugs (~45 μm radius) seen in the sample held for 30 s would require the rapid coalescence of 27 bubbles of mean bubble radius ~15 μm. The curved edges to samples held for <120 s are also indicative of the presence of large bubbles prior to fragmentation. With an average radius of curvature of ~55 μm, they are of the same order of magnitude of the vugs seen in earlier samples.

In complete contrast, the sample held for 900 s at 30 MPa does not show evidence of coalescence-induced coalescence despite having N_v^m similar to the samples held for 15-30 seconds and a narrow BSD. Similarly, in the Larsen et al. (2004) study where the maximum porosity is ~35 vol. %, the bubble populations coarsen over hours. This evidence highlights the relative importance of this mechanism only as the bubble population is forced to take on a close packed arrangement at high porosities. The results

of this study demonstrate that vesiculation to equilibrium porosities >70 vol. % at 10 MPa final pressure result in dramatically different behavior, providing evidence that close-packing at relatively high porosities is needed to trigger rapid coalescence and degassing. In addition, coalescence-induced coalescence should occur more commonly in magmas with a relatively uniform bubble size distribution, since binary coalescence as discussed above is favored for broad bubble size distributions due to differences in their internal pressures (Proussevitch et al. 1993).

Stage II- Collapse

No simple model exists for the mechanical strength of porous materials due to the many critical parameters that govern their properties (porosity, pore size, pore size distribution etc.). However, high mechanical strength is generally exhibited in materials with a homogeneous pore structure. Holding total porosity constant, the incorporation of larger pores into the material leads to local stress concentrations, which act to reduce the mechanical strength. Similarly, we propose that as the BSD evolved through the appearance of large vugs over the first 60 s of the experimental duration at 10 MPa, the strength of the porous experiments decreased until reaching the critical point of total sample collapse, resulting in the degassed fragments that exhibit far fewer dispersed bubbles over the 60-900 s time interval. This observation differs substantially from the conclusions derived from the permeable foam model and prior related experiments (Burgisser and Gardner 2004; Westrich and Eichelberger 1994), which were labeled strictly permeable or impermeable based entirely on porosity. In those models, a rhyolite foam could become permeable and degas once reaching a critical porosity threshold,

creating an impermeable bubble network that nevertheless retains a high enough porosity to achieve permeability a second time, as vapor exsolution continues. The catastrophic collapse observed in the present experiments is clearly irreversible, unless further bubble nucleation introduces an entirely new population of bubbles to start the process a second time.

Implications for Volcanic Conduit Processes

The transition from effusive to explosive eruptive behavior is generally attributed to how quickly magmas become permeable and degas, relative to the ascent rate and whether the conduit walls themselves are permeable or sealed (Eichelberger 1995; Jaupart and Allegre 1991; Taylor et al. 1983). The experiments presented here replicate ascent of an initially H_2O vapor-saturated, crystal-poor rhyolite magma at ~ 0.4 ms^{-1}, to a depth of ~ 0.4 km where it stalls for a relatively short period of time (15 minutes). At those conditions, the experiments predict that the magma would exsolve H_2O in equilibrium, generating a highly vesicular, interconnected bubble network. Subsequent degassing and collapse of the highly porous magma would happen over a very short timescale of seconds to minutes. Our experimental results indicate that the rapid collapse of a vesiculated rhyolite magma with initially ~73 vol. % vesicles can occur over a timescale of 1 to 2 minutes at pressures near those estimated for fragmentation by Burgisser and Gardner (2004), rapidly releasing a large volume of H_2O vapor, followed by nearly complete collapse of the bubble network, caused by a cascading coalescence induced coalescence process. The results imply that, at ascent rates approaching those estimated

for explosive eruptions, initially vapor-saturated rhyolite magmas could degas rapidly at shallow levels in a closed conduit.

During Vulcanian eruption cycles, overpressure builds beneath a conduit plug. At some critical over pressure, an explosion occurs, fragmenting the conduit plug or alternatively displacing the plug during an effusive phase. The rates of degassing and collapse experimentally constrained in our study can provide estimates of the timescales needed to create a degassed plug of magma at shallow levels in the conduit. Assuming a 30 m conduit diameter, Eq. (2) predicts that the formation of a 50 m thick plug of degassed rhyolite magma (78 vol. % initial porosity), would produce a total of ~0.5 million m^3 gas at 10 MPa (50 million m^3 gas at surface pressures) released over a 15 minute time period, assuming that the plug formed in one collapse event. Figure 3.12 illustrates the formation of this gas slug from a highly vesicular magma undergoing catastrophic collapse beneath a conduit plug. Further magma ascent leads to pressurization of the overlying gas slug until the critical overpressure is reached at which the strength of the overlying plug is exceeded, resulting in plug fragmentation and an explosive eruption. During the 1996 eruption of Soufriere Hills Volcano , a minimum pressurization of 27.5MPa was required to explain the locations of several large ballistics (Robertson et al. 1998) with typical excess pressures estimated to be 5–20 MPa (Sparks 1997). Assuming a magma flow rate of 7.5 m^3s^{-1} (as in Diller et al. (2006)), the time taken to compress the 0.5 million m^3 gas slug to an overpressure of 5-20 MPa is 6-12 hours, similar to the ten hour repose interval at Soufriere Hills Volcano. Increasing the magma flow rate decreases the time taken to reach the critical overpressure. Gas loss through permeable conduit walls (Jaupart 1998;

Jaupart and Allegre 1991; Woods and Koyaguchi 1994) will increase the time needed to reach the critical overpressure. An effusive phase may follow as the parent degassed magma ascends, an alternative mechanism to shear based fragmentation (Gonnerman and Manga 2003) for creating a relatively degassed magma that erupts effusively. Coalescence induced coalescence of highly vesicular magmas leading to catastrophic collapse and gas slug generation provides an alternative mechanism for building overpressures quickly in Vulcanian eruptions and provides a possible explanation for cycles of effusive and explosive behavior.

Conclusions

This study revealed that a high N_v^m which narrowly constrains the bubble size distribution and thereby inhibits coalescence is critical to the generation of an interconnected highly vesicular (~73 vol. %) magma. The close packed arrangement that the bubbles are forced to adopt, brings a new coalescence mechanism into play-coalescence induced coalescence, where the coalescence of two bubbles promotes the coalescence of neighboring bubbles, generating large vugs. The presence of these vugs destabilizes the vesicular magma through stress concentrations leading to eventual collapse and abrupt degassing over a timescale of minutes. Thus degassing can be fast and these experiments also show that it can be almost complete. On a conduit scale, these results may be relevant to understanding vulcanian plug formation rates, overpressure buildup and effusive eruptions.

Acknowledgements

This work was supported by NSF EAR 0511070. We thank Don Baker, Liping Ba and an anonymous reviewer for comments on an earlier version of the manuscript.

References

Bagdassarov N, Dorfman A, Dingwell DB (2000) Effect of alkalis, phosphorus, and water on the surface tension of haplogranite melt. Am Mineral 85(1):33-40

Blower JD, Mader HM, Wilson SDR (2001) Coupling of viscous and diffusive controls on bubble growth during explosive volcanic eruptions. Earth Planet Sci Lett 193(1-2):47-56

Burgisser A, Gardner JE (2004) Experimental constraints on degassing and permeability in volcanic conduit flow. Bull Volcanol 67(1):42-56

Cashman KV, McConnell SM (2005) Multiple levels of magma storage during the 1980 summer eruptions of Mount St. Helens, WA. Bull Volcanol 68:57-75

Diller K, Clarke AB, Voight B, Neri A (2006) Mechanisms of conduit plug formation: Implicaions for vulcanian explosions. Geophys Res Lett 33(L20302)

D'Oriano C, Poggianti E, Bertagnini A, Cioni R, Landi P, Polacci M, Rosi M (2005) Changes in eruptive style during the AD 1538 Monte Nuovo eruption (Phlegrean Fields, Italy): The role of syn-eruptive crystallization. Bull Volcanol 67:601-621

Eichelberger JC (1995) Silicic volcanism; ascent of viscous magmas from crustal reservoirs. An Rev Earth Planet Sci 23:41-63

Eichelberger JC, Carrigan CR, Westrich HR, Price RH (1986) Non-explosive silicic volcanism. Nature 323(6089):598-602

Fink JH, Anderson SW, Manley CR (1992) Textural constraints on effusive silicic volcanism: Beyond the permeable foam model. J Geophys Res 97:9073-9083

Gardner JE (2007) Bubble coalescence in rhyolitic melts during decompression from high pressure. J Volcanol Geotherm Res 166:161-176

Gardner JE, Hilton M, Carroll MR (1999) Experimental constraints on degassing of magma; isothermal bubble growth during continuous decompression from high pressure. Earth Planet Sci Lett 168(1-2):201-218

Gardner JE, Thomas RME, Jaupart C, Tait S (1996) Fragmentation of magma during Plinian volcanic eruptions. Bull Volcanol 58(2):144-162

Gonnerman HMG, Manga M (2003) Explosive silicic volcanism may not be an inevitable consequence of magma fragmentation. Nature 323:598-602

Hammer J, Cashman KV, Hoblitt RP, Newman S (1999) Degassing and microlite crystallization during pre-climatic events of the 1991 eruption of Pinatubo, Philippines. Bull Volcanol 60:355-380

Heiken G, Wohletz K, Eichelberger JC (1988) Fracture fillings and intrusive pyroclasts, Inyo Domes, California. J Geophys Res 93:4335-4350

Hui H, Zhang Y (2006) Toward a general viscosity equation for natural anhydrous and hydrous silicate melts. Geochim Cosmochim Acta 2007(71):403-416

Jaupart C (1998) Gas loss from magmas through conduit walls during eruption. The Physics of Explosive Volcanic Eruptions. Geological Society of London Special Publication, pp 73-90

Jaupart C, Allegre CJ (1991) Gas content, eruption rate and instabilities of eruption regime in silicic volcanoes. Earth Planet Sci Lett 102:413-429

Klug C, Cashman KV (1996) Permeability development in vesiculating magmas; implications for fragmentation. Bull Volcanol 58(2-3):87-100

Klug C, Cashman KV, Bacon CR (2002) Structure and physical characteristics of pumice from the climactic eruption of Mount Mazama (Crater Lake), Oregon. Bull Volcanol 64:486-501

Larsen JF, Gardner JE (2004) Experimental study of water degassing from phonolite melts: implications for volatile oversaturation during magmatic ascent. J Volcanol Geotherm Res 134:109-124

Larsen JF, Denis M-H, Gardner JE (2004) Experimental study of bubble coalescence in rhyolitic and phonolitic melts. Geochim Cosmochim Acta 68(2):333-344

Lyakhovsky V, Hurwitz S, Navon O (1996) Bubble growth in rhyolitic melts-experimental and numerical investigation. Bull Volcanol 58(1):19-32

Mangan M, Sisson TW (2000) Delayed, disequilibrium degassing in rhyolite magma; decompression experiments and implications for explosive volcanism. Earth Planet Sci Lett 183(3-4):441-455

Martula DS, Bonnecaze RT, Lloyd DR (2003) The effects of viscosity on coalescence-induced coalescence. International Journal of Multiphase Flow 29:1265-1282

McGuire KS, Laxminarayan A, Lloyd D, R (1995) Kinetics of droplet growth in liquid-liquid phase separation of polymer-diluent systems: experimental results. Polymer 36(26):4951-4960

McGuire KS, Laxminarayan A, Martula DS, Lloyd D, R (1996) Kinetics of droplet growth in liquid-liquid phase separation of polymer diluent systems: Model Development. J Colloid Interface Sci 182:46-58

Melnik O, Sparks RSJ (1999) Nonlinear dynamics of lava dome intrusion. Nature 402:37-41

Navon O, Lyakhovsky V (1998) Vesiculation processes in silicic magmas. In: Gilbert JS, Sparks RSJ (eds) The Physics of Explosive Volcanic Eruptions. Geological Society, Special Publications, London, pp 27-50

Proussevitch AA, Sahagian DL, Kutolin VA (1993) Stability of foams in silicate melts. J Volcanol Geotherm Res 59(1-2):161-178

Robertson R, Cole P, Sparks RJS, Harford C, Lejeune AM, McGuire WJ, Miller AD, Murphy MD, Norton G, Stevens NF, Young SR (1998) The explosive eruption of Soufriere Hills Volcano, Montserrat, West Indies, 17 September, 1996. Geophys Res Lett 25:3429-3432

Rust AC, Cashman KV, Wallace PJ (2004) Magma degassing buffered by vapor flow through brecciated conduit margins. Geology 32(4):349-352

Saar MO, Manga M (1999) Permeability-porosity relationship in vesicular basalts. Geophys Res Lett 26(1):111-114

Sparks RSJ (1997) Causes and consequences of pressurisation in lava dome eruptions. Earth Planet Sci Lett 150:177-189

Taddeucci J, Pompilio M, Scarlato P (2004) Conduit Processes during the July-August 2001 explosive activity of Mt Etna (Italy): Inferences from glass chemistry crystal size distribution of ash particles. J Volcanol Geotherm Res 137:33-54

Takeuchi S, Nakashima S, Tomiya A, Shinohara H (2005) Experimental constraints on the low gas permeability of vesicular of vesicular magma during decompression. Geophys Res Lett 32(L10312)

Tanaka H (1994) New coarsening mechanisms for spinodal decomposition having droplet patterns in binary fluid mixture: Collision-Induced Collisions. Phys Rev Lett 11:1702-1705

Taylor BE, Eichelberger JC, Westrich HR (1983) Hydrogen isotopic evidence of rhyolitic magma degassing during shallow intrusion and eruption. Nature 306(8-14):541-545

Tuffen H, Dingwell DB, Pinkerton H (2003) Repeated fracture and healing of silicic magma generate flow banding and earthquakes ? Geology 31:1089-1092

Westrich HR, Eichelberger JC (1994) Gas transport and bubble collapse in rhyolite magma: An experimental approach. Bull Volcanol 56:447-458

Westrich HR, Stockman HW, Eichelberger JC (1988) Degassing of rhyolitic magma during ascent and emplacement. J Geophys Res 93(B6):6503-6511

Woods AW, Koyaguchi T (1994) Transitions between explosive and effusive eruptions of silicic magmas. Nature 370(6491):641-644

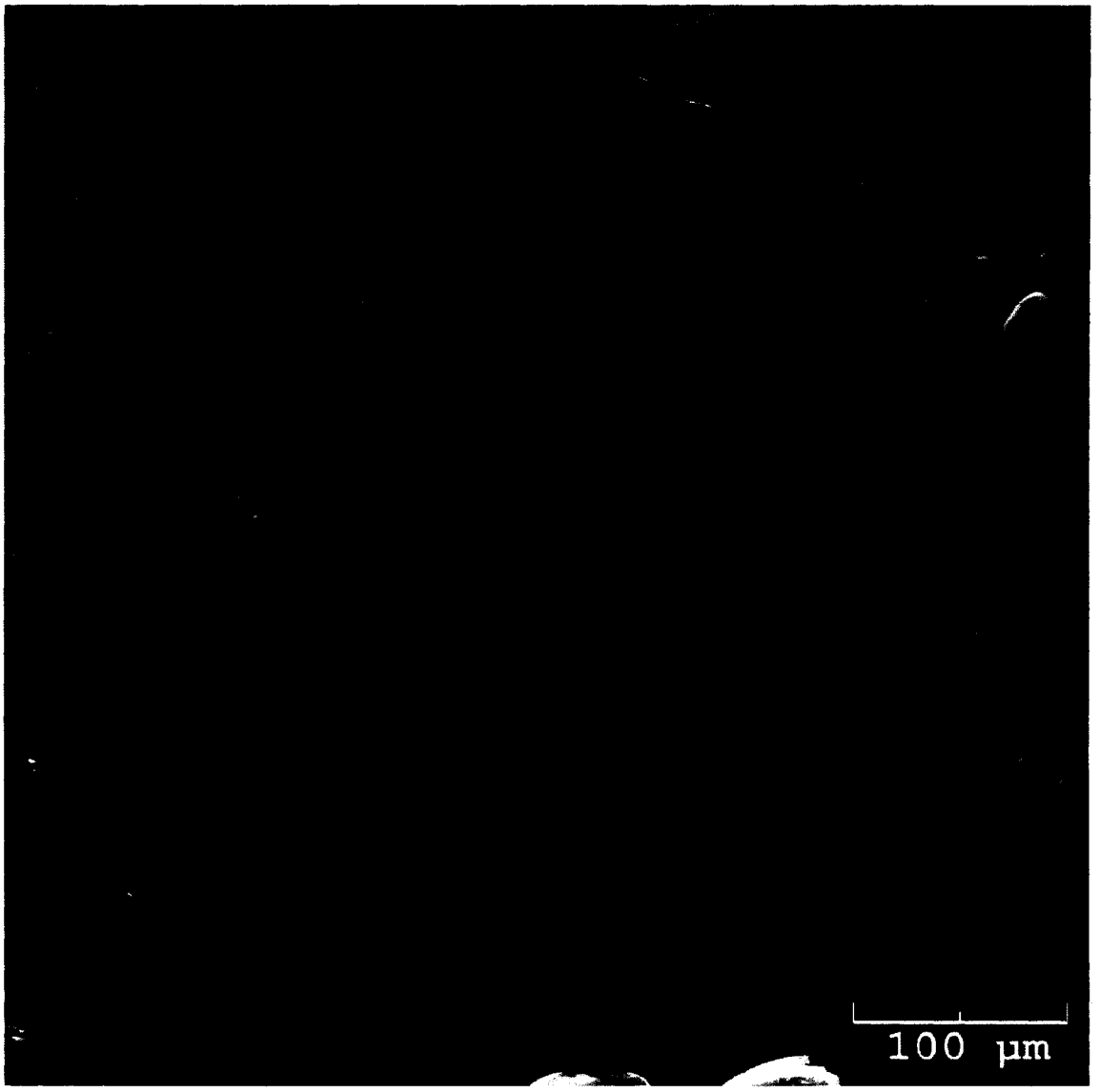

Figure 3.1 SEM image of sample mc1_b15_5 after a hold time of 15 seconds. Sample is of high porosity with interconnected vesicles.

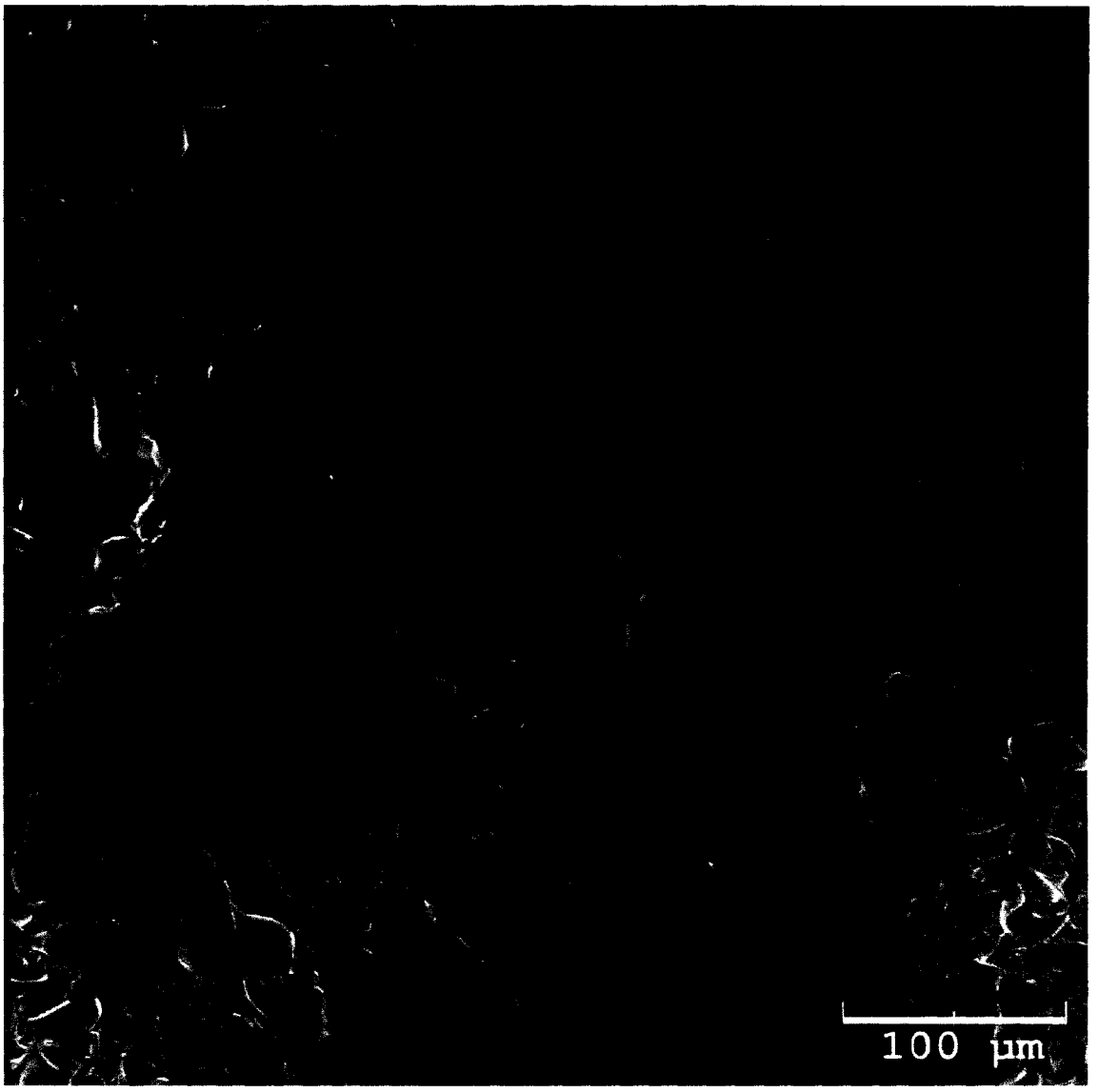

Figure 3.2 SEM image of sample mc1_b15_4 after a hold time of 30 seconds. Sample is highly porous with large dispersed vugs.

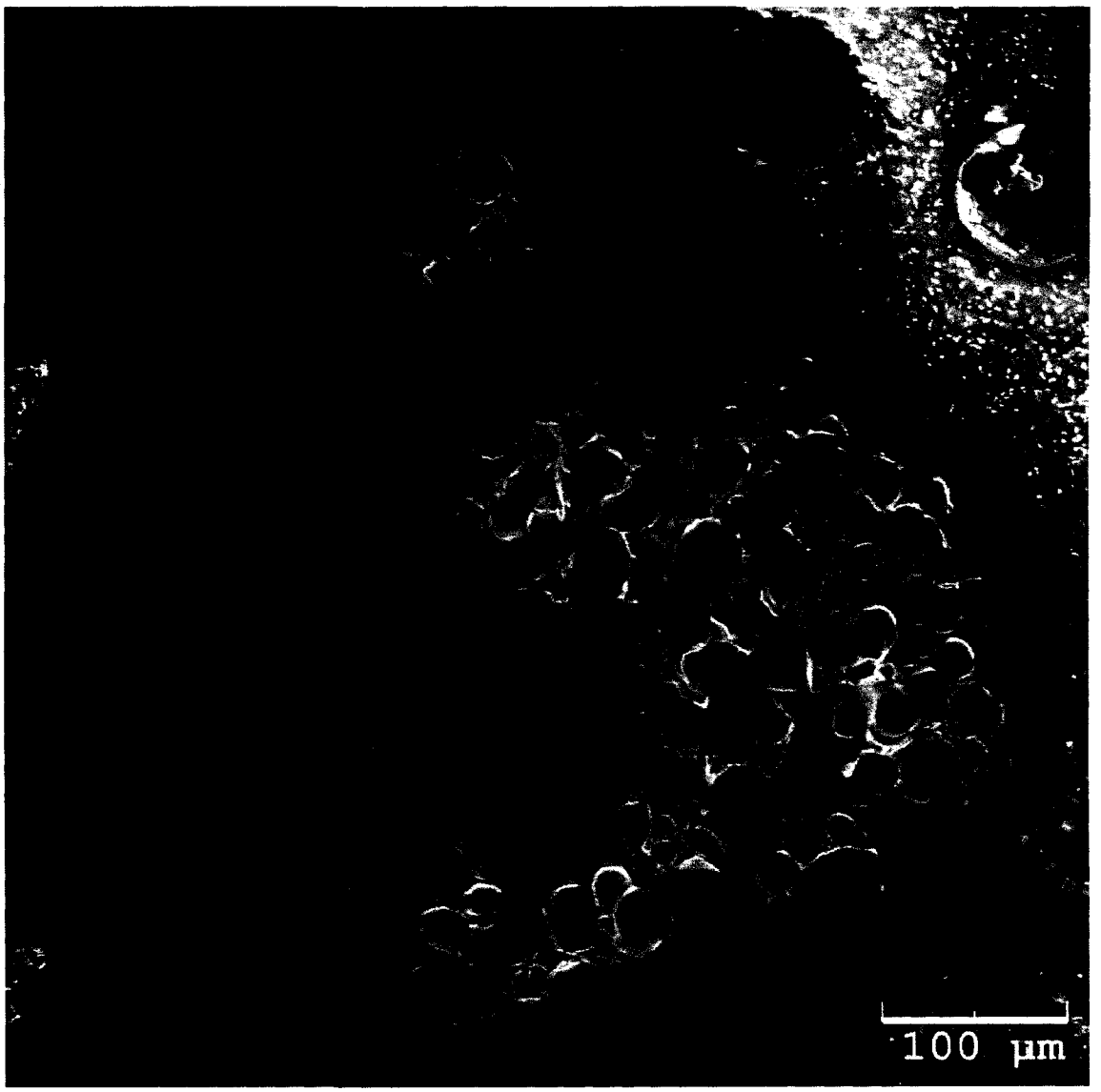

Figure 3.3 SEM image of high porosity texture evident in sample mc1_b16_3. Chunks from this sample which was held for 60 seconds exhibit a texture of either high porosity with vugs or much lower porosity with deformed bubbles.

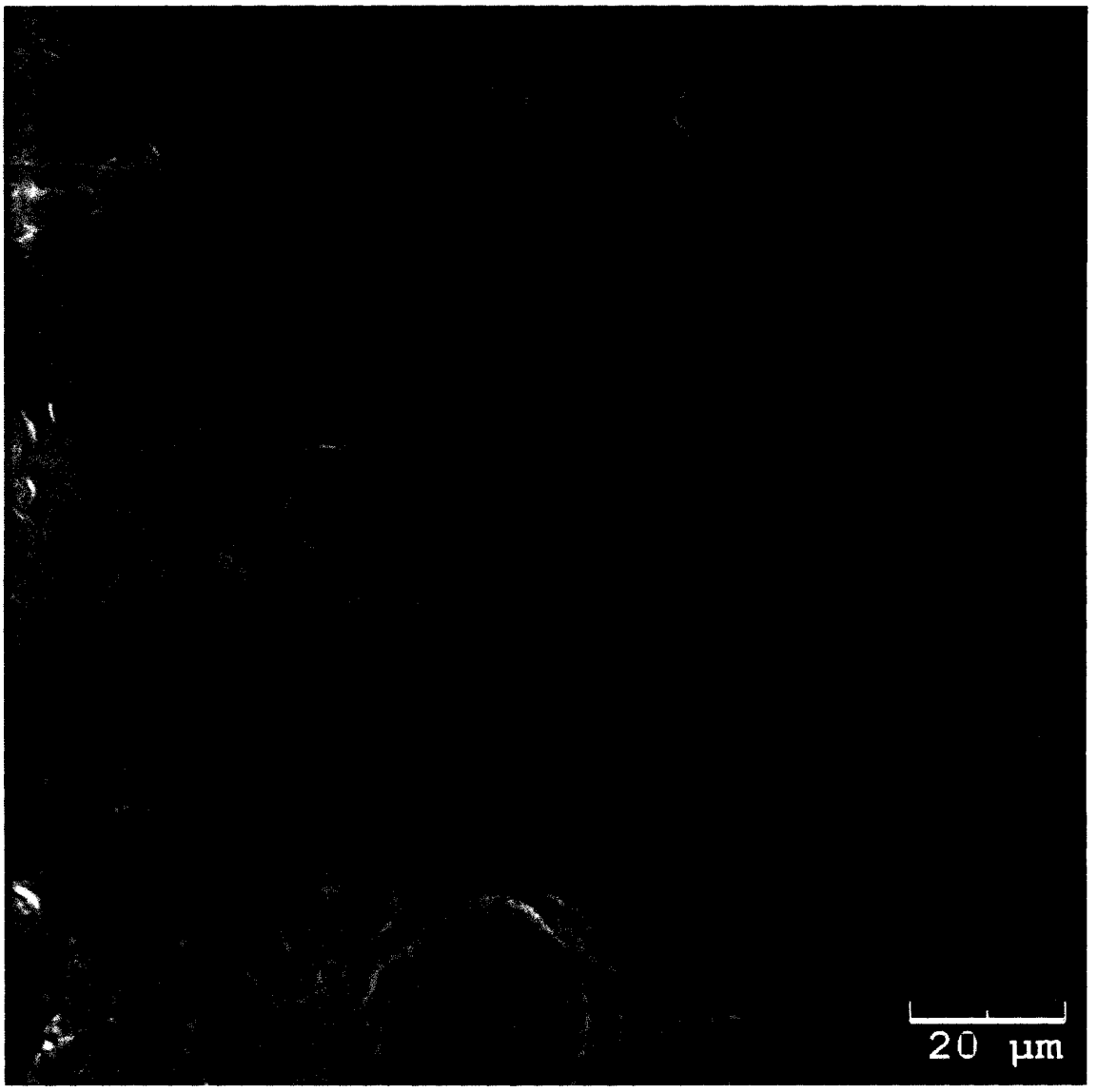

Figure 3.4 SEM image of low porosity texture evident in sample mc1_b16_3. Chunks from this sample which was held for 60 seconds exhibit a texture of either high porosity with vugs or much lower porosity with deformed bubbles.

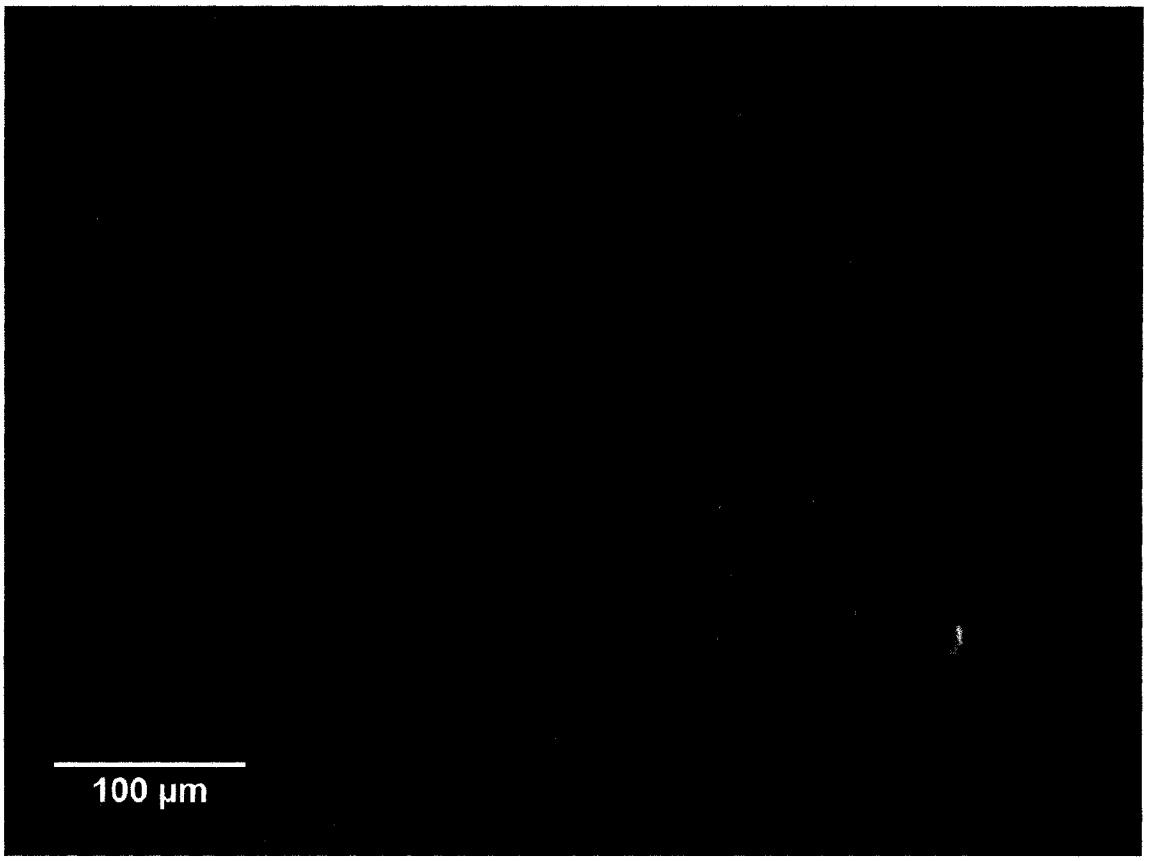

Figure 3.5 Reflected light photomicrograph of sample mc1_b14_6 after a hold time of 120 seconds.
Sample has low porosity and deformed bubbles.

Figure 3.6 Reflected light photomicrograph of sample mc1_b14_7 after a hold time of 300 seconds.
Sample is virtually bubble free with reverse curved fragment edges.

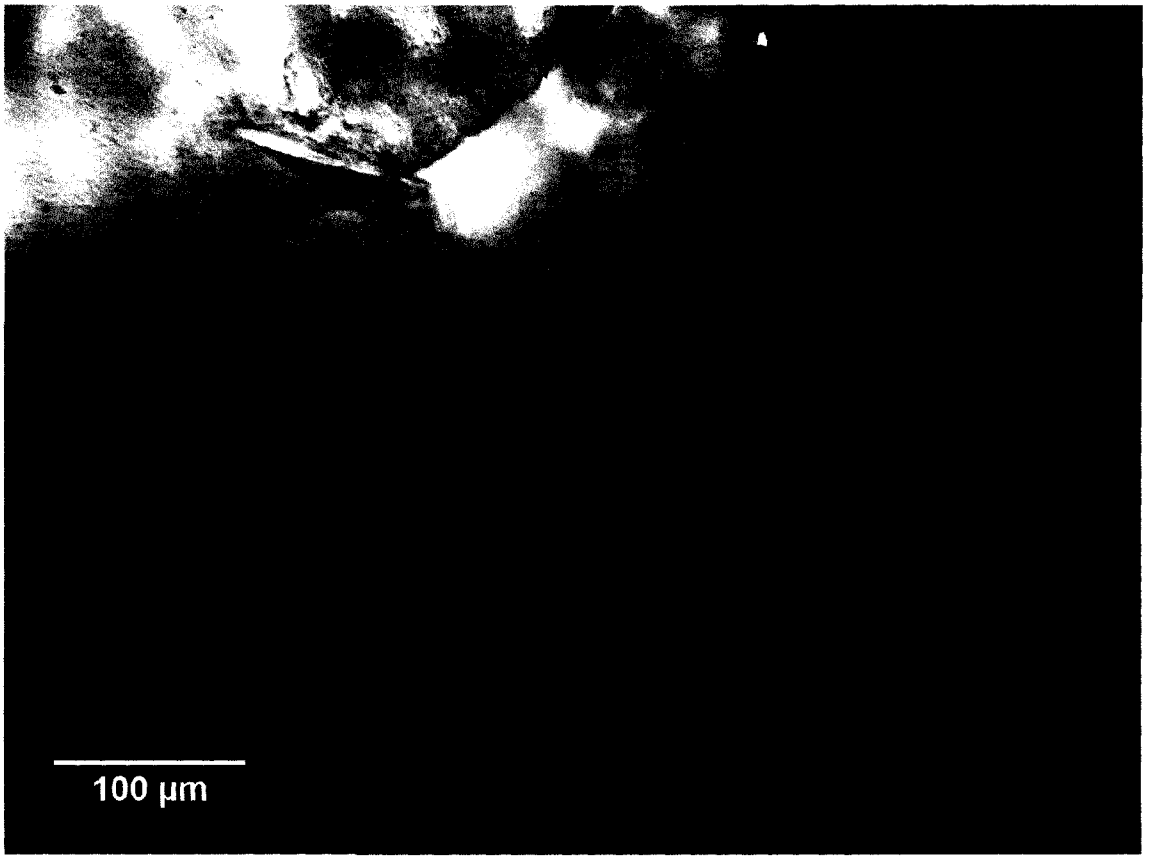

Figure 3.7 Reflected light photomicrograph of sample mc1_b14_1 after a hold time of 900 seconds.
Sample is also virtually bubble free with reverse curved fragment edges.

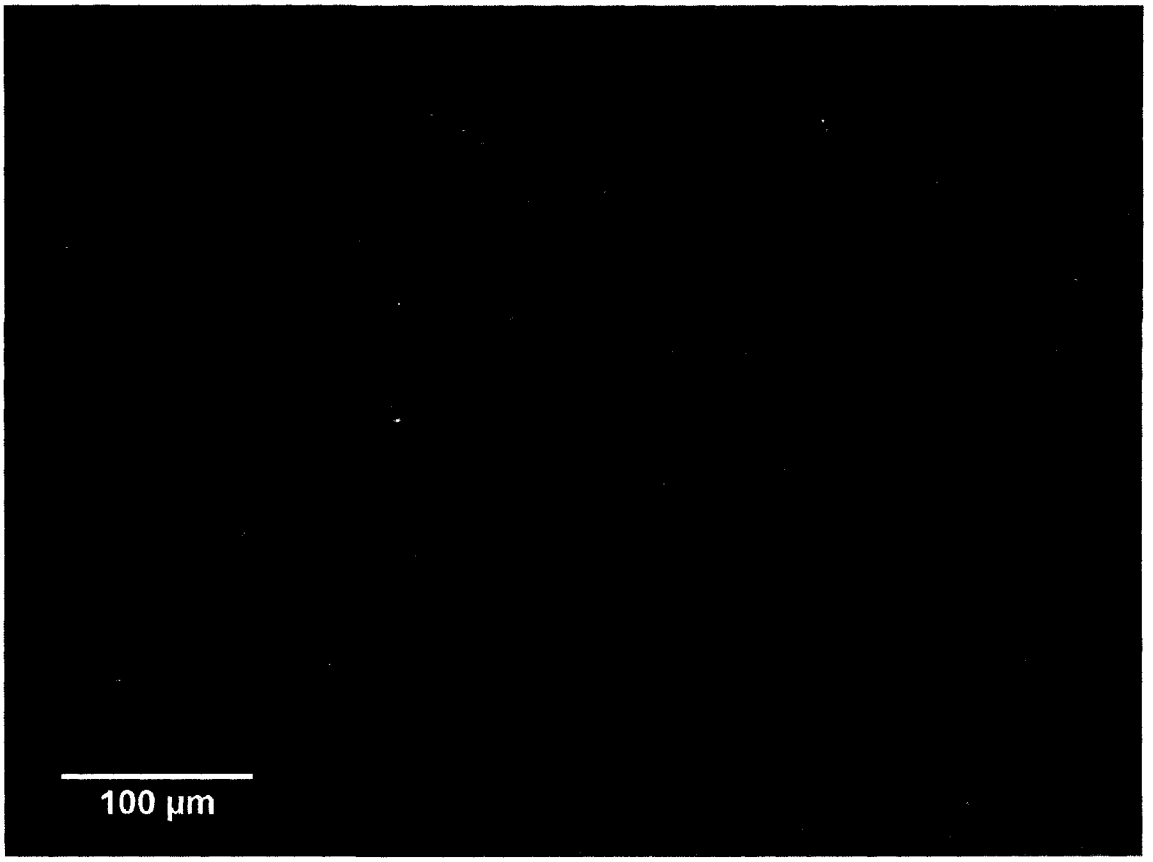

Figure 3.8 Reflected light photomicrograph of sample mc1_b15_3 held for 900s at 30MPa. The porosity remains at equilibrium values, assuming no degassing, and is derived from a population of evenly distributed similar sized bubbles.

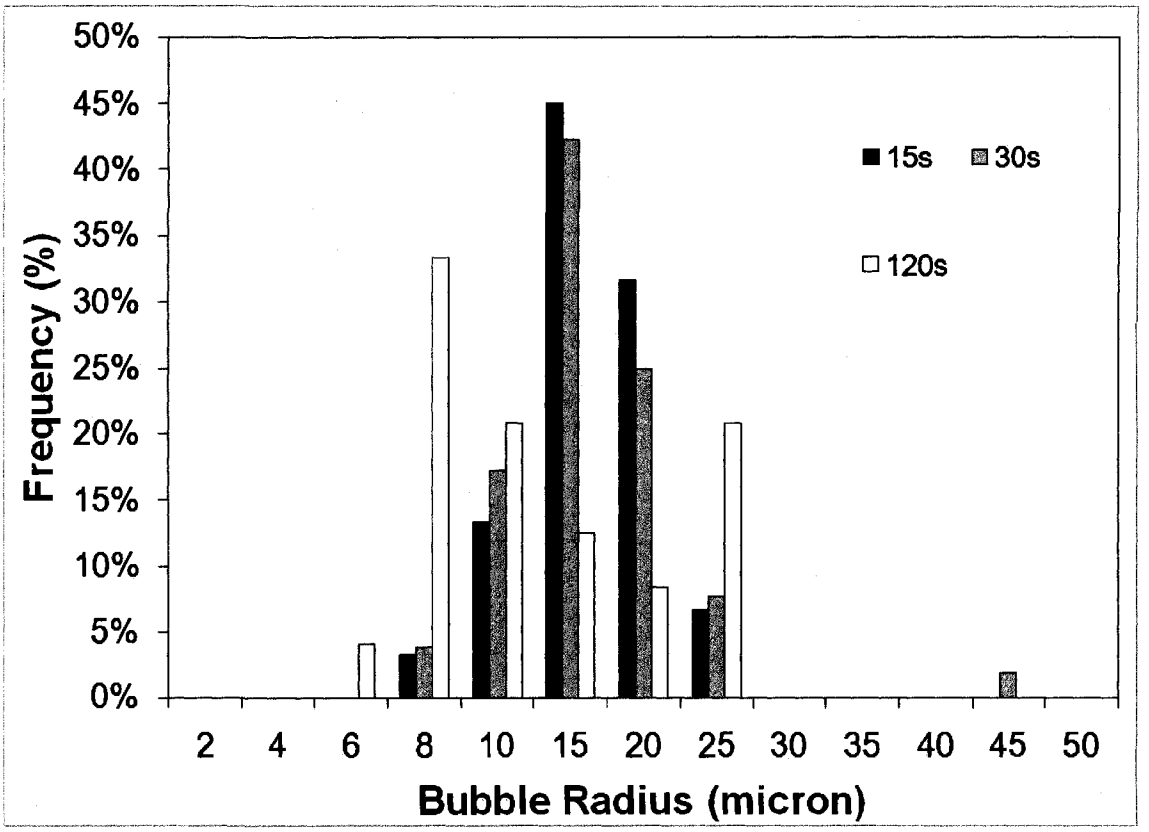

Figure 3.9 Bubble size distribution evolution (BSD) over 15-120s.
BSD evolves from 15 to 30s through large vug generation. BSD after 120s is still narrow despite large reduction in porosity.

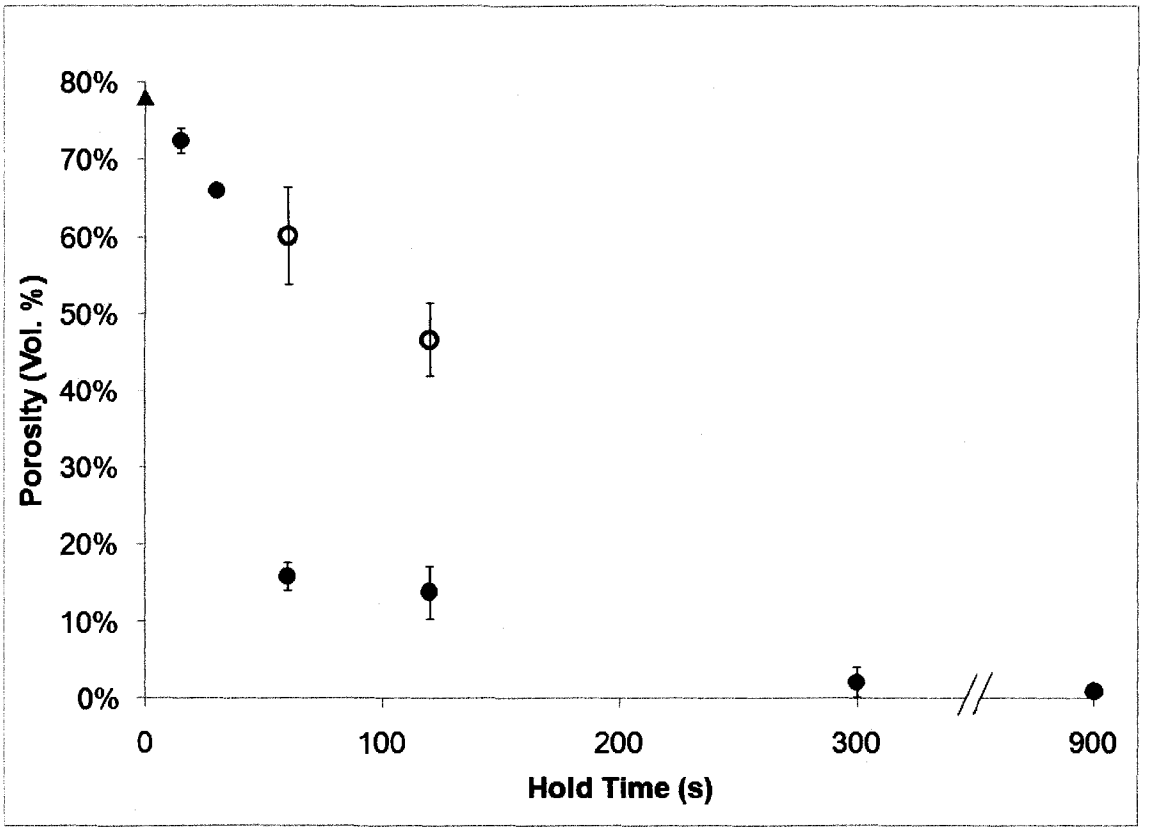

Figure 3.10 Sample porosity change over time from 0s to 900s.
Sample porosity decreases gradually from near equilibrium values over 0-60s before abruptly dropping, resulting in almost no vesicularity after 300s. Samples quenched after 60 and 120s are heterogeneous. High measured vesicularities for these samples are plotted in open circles. Porosity estimated to arise from equilibrium exsolution with no sample degassing is plotted in filled triangle. All other vesicularities are plotted in filled circles. Error bars are ±1σ.

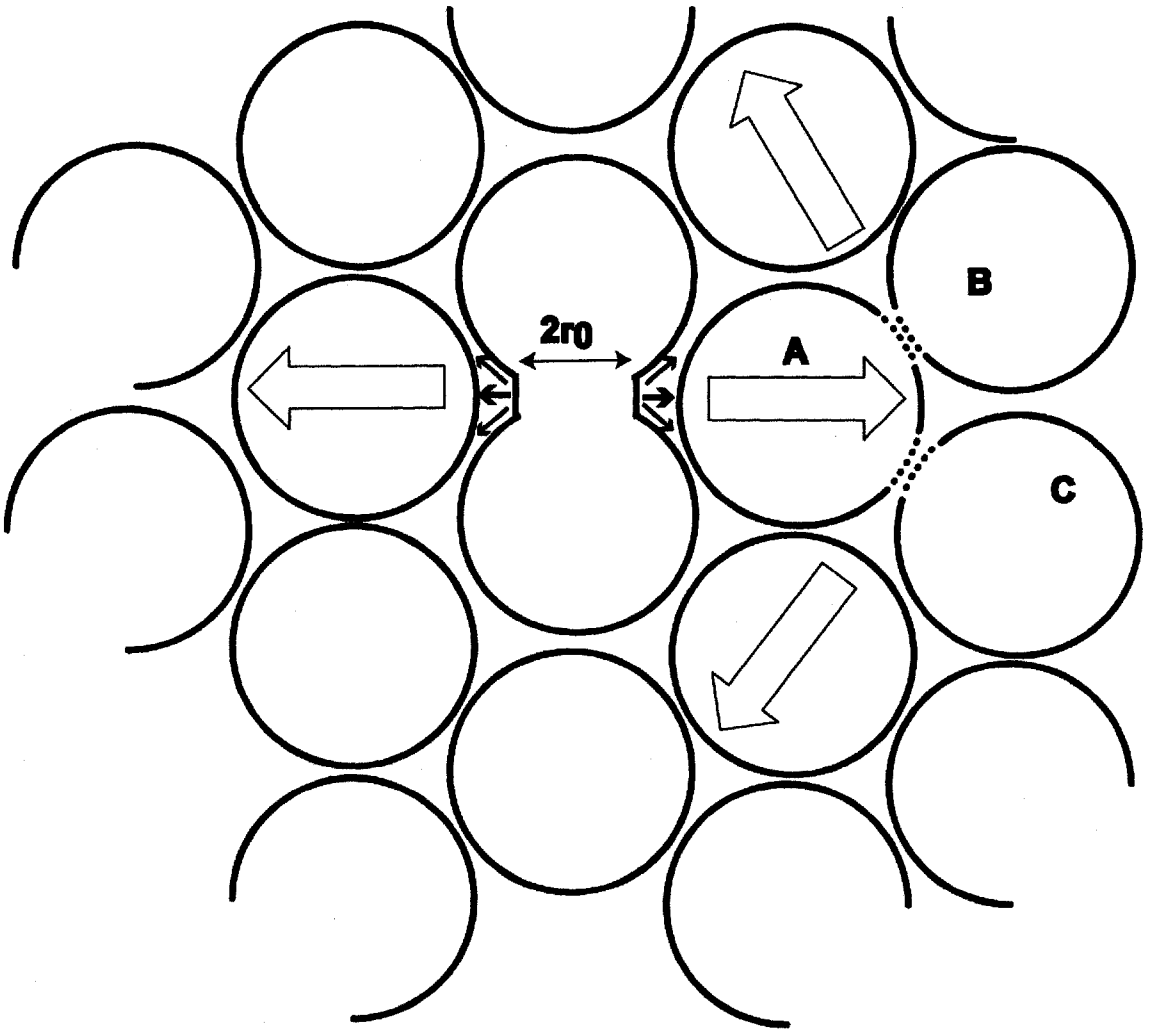

Figure 3.11 Cartoon showing coalescence-induced coalescence applied to highly vesicular rhyolite.
A newly coalesced bubble is irregularly shaped with a neck of width, $2r_0$. Fast relaxation of the bubble induces a localized flow in the surrounding melt which moves bubble A away from the coalescing bubbles. As bubble A is repelled away from the coalescing bubbles, the films between bubble A and adjacent bubbles B and C thin resulting in coalescence of these bubbles and attendant melt expulsion leading to a cascade of coalescence events.

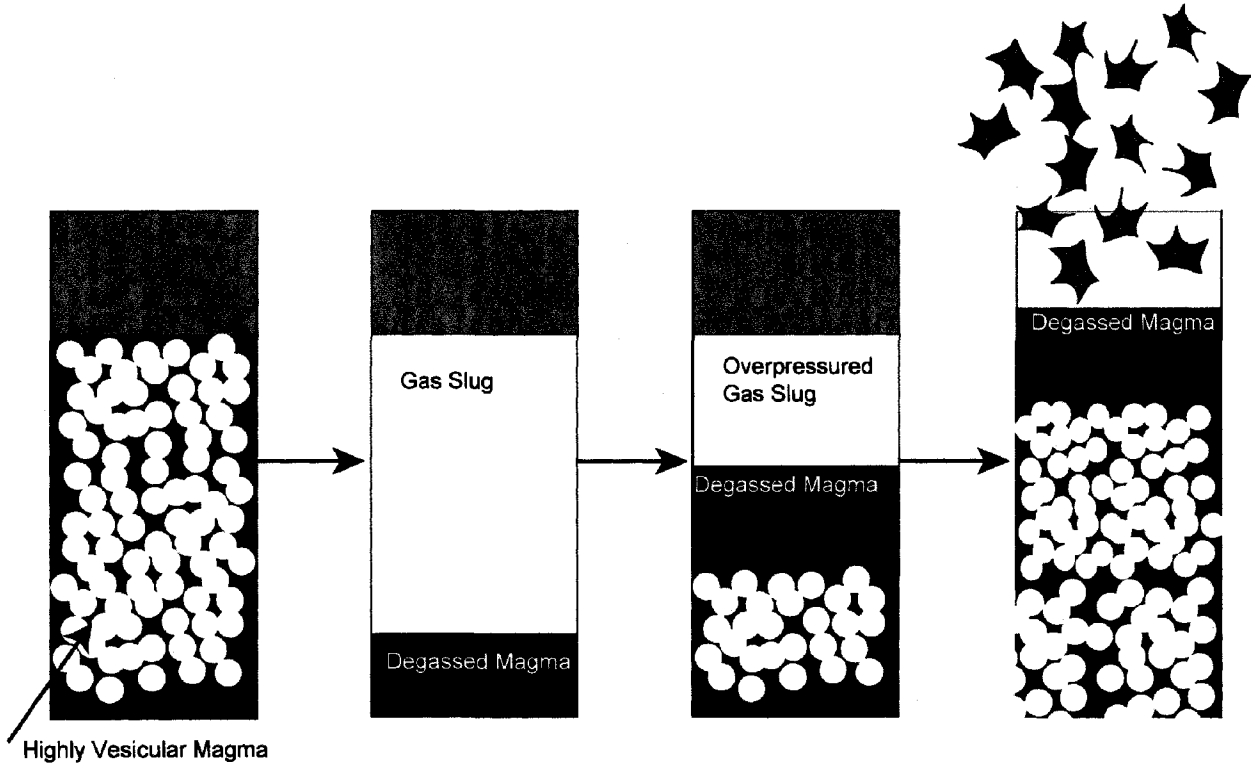

Figure 3.12 Cartoon showing creation of gas slug from collapse of highly vesicular magma followed by gas slug compression as additional magma ascends.
At critical overpressure, overlying conduit plug fragments and explosive eruption occurs.

Table 3.1 Summary of sample bubble population characteristics.

Run Name	Decompression Rate $MPas^{-1}$	P_{final} (MPa)	Time at P_{final} (s)	Porosity (vol.%)	r_{mean} (micron)	# Bubbles	$N_v^b \times 10^9$ cm^{-3}	$N_v^m \times 10^9$ cm^{-3}
mc1_b15_5	0.01	10	15	72.5(1.6)%	13.7(3.6)	60.0	1.05(0.11)	3.82(0.11)
mc1_b15_4	0.01	10	30	66.1(0.8)%	15.1(8.3)	52.0	0.44(0.20)	1.28(0.20)
mc1_b16_3_chunk_1	0.01	10	60	15.8(1.8)%	-	-	-	-
mc1_b16_3_chunk2	0.01	10	60	60.2(6.3)%	7.6(2.7)	45.0	2.97(0.47)	7.46(0.50)
mc1_b14_6_chunk1	0.01	10	120	13.8(3.4)%	12.1(6.3)	24.0	0.87(0.27)	1.11(0.32)
mc1_b14_6_chunk2	0.01	10	120	46.8(4.7)%				
mc1_b14_7	0.01	10	300	2.1(1.9)%	< 2	-	-	-
mc1_b14_1	0.01	10	900	0.9(0.3)%	<2	-	-	-
mc1_b14_3	0.05	30	0	41.3(5.1)				
mc1_b15_3	0.01	30	900	41.6(8.7)	7.0(3.4)	60.0	2.80(0.49)	4.79(0.53)

Notes

All samples were hydrated at 825 °C and 150 MPa. Decompression rate is from 100 to final pressure. P_{Final} is final/quench pressure. Time held at final pressure is in addition to time held at final pressure in order to approximate given decompression rate. Porosity of final product is determined using a minimum of 3 images per sample, with ±1σ error listed. r_{mean} is the average bubble radius, with ±1σ error listed. For the SEM images this is the intersected bubble radius, for the petrographic microscope images, this is the true bubble radius. N_v^b= bubble number density of bubbles; with ±1σ error listed. N_v^m=bubble number density final products corrected for melt volume with ±1σ error listed.

Chapter 4 Spatial Point Pattern Analysis Applied to Bubble Nucleation in Silicate Melts[3]

Abstract

Experimental bubble nucleation studies are used for determining the nucleation mechanism as a function of experimental conditions, the resulting bubble number density, and can also yield estimates of the melt-vapor surface tension via classical nucleation theory. Thus, they provide important information on gas exsolution in silicate melts to be applied towards understanding magmatic degassing in volcanic conduits. At present, determination of nucleation processes in tiny experimental samples relies upon visual observations. To improve the characterization of the spatial distribution of bubbles, we present a new application of spatial point pattern analysis. This technique allows the quantitative description of the spatial distribution of nucleation sites and has the potential to distinguish between homogeneous, heterogeneous, and multiple nucleation events. Since point pattern analysis highlights clustering or spatial regularity among objects, it can also lead towards a better understanding of the melt structure underlying the spatial distribution of nucleation sites, as well as the interaction between bubble populations resulting from different periods of nucleation within a single experimental sample.

Keywords: bubble; spatial statistics; Spatstat; nucleation; experiments

Introduction

[3] Joanna Mongrain and Jessica Larsen submitted to Computers and Geoscience, April 2008

Spatial point pattern analysis is a powerful technique used to apply statistical analyses to a dataset which records the spatial locations of objects observed within a certain region. This technique has been used across many disciplines to study the spatial distribution of objects such as trees (Cox, 1979), galaxies (Peebles, 1974) and neuron profiles in brains (Diggle et al., 1991). The result is a quantification of where the objects are located relative to one another and how they interact or influence each other. Statistical models fit to the distributions can provide further insights into the physical processes governing the object locations in two dimensions. In order to make meaningful comparisons of spatial point patterns, a reference model is required that corresponds to complete spatial randomness. This is almost always the stationary Poisson Point Process. Point patterns are then classified as being more aggregated/clustered or more regular than a Poisson distribution modeled using the same intensity or number density of objects.

We present the application of spatial point pattern analysis to bubble nucleation experiments performed in silicate melts decompressed and quenched from high pressures and temperatures. This technique allows for quantitative description of the spatial distribution of bubbles and has the potential to distinguish between homogeneous and heterogeneous nucleation mechanisms based on spatial distributions beyond simple visual observations (e.g. Hurwitz and Navon (1994) and Mangan and Sisson (2000). It could also enable researchers to separate and quantify multiple nucleation events that occurred within one experiment. In addition, since this technique highlights clustering or spatial regularity in nucleation sites, it may prove useful in elucidating the underlying melt structure or point to the location of sub microscopic crystallites. The point pattern

arising from the intersection of bubbles with the polished surface is not a genuine planar point pattern because of the well known cut effect from stereology e.g. Russ (1998), and therefore direct interpretations of the spatial point patterns are limited. However, the ability to make quantitative comparisons between and within samples, gives insights into the spatial controls on nucleation unattainable through any other current methods which may be applied to experimental samples.

Background

One of the key drivers in eruption dynamics is the nucleation and growth of bubbles as the evolution of a large gas volume from a hydrated melt during decompression alters many of the key parameters, such as viscosity and density, which govern the eruptive style. Generally, if magma is unable to sufficiently degas on ascent, fragmentation may occur, precipitating an explosive eruption. The fragmentation process may be initiated on reaching either a critical gas volume fraction or critical stress/strain around the bubbles. Both mechanisms share a common dependence on the character of the bubble population.

Experimental studies are frequently used to isolate the critical parameters governing bubble nucleation and for estimating melt surface tension- an important parameter for eruption dynamics. Bubbles nucleate in a melt in response to a pressure drop which causes the dissolved volatiles to be supersaturated in the melt with respect to external pressure. The degree of supersaturation required for homogeneous nucleation, where the nucleation site is dependent only on random volatile fluctuations, is a function of the surface tension and can be as high as 100MPa for hydrated rhyolite melts (Mourtada-

Bonnefoi and Laporte, 2004). Nucleation is also observed to occur at much lower supersaturations, assisted by the reduced energy of activation required for nucleation on existing sites such as crystals (Hurwitz and Navon, 1994) and this is classified as heterogeneous nucleation.

Classical nucleation theory describes the thermodynamics of fluid phase separation, and can be applied to the process of gas vapor exsolution in silicate melts. Following Hurwitz and Navon (1994), the nucleation rate, J, for a given pressure drop (ΔP) imposed on a water-saturated silicate melt, for example, can be calculated using Eq.(1) from classical nucleation theory e.g. Hirth et al. (1970)

$$J = J_0 \exp\left(-\frac{16\pi\sigma^3}{3kT\Delta P^2}\right) \qquad (1)$$

Where J_0 is a pre-exponential factor related to the concentration and molar volume of dissolved H_2O molecules in the melt, k is H_2O diffusivity, T is temperature, and σ is the surface tension. Derivation of J_0 is detailed in (Hurwitz and Navon, (1994) and Toramaru (1989). According to the kinetic model of Kolmogorov-Johnson-Mehl-Avrami (Avrami, 1940; Johnson and Mehl, 1939; Kolmogorov, 1937), the nuclei result from random volatile fluctuations. Therefore, the distribution of homogenously nucleated bubbles should approximate a completely spatially random Poisson distribution. The spatial arrangement of bubbles resulting from heterogeneous nucleation should deviate substantially from the Poisson distribution and reflect the locations of the crystals (Hurwitz and Navon, 1994; Mangan and Sisson, 2000).

The nucleation mechanism controls the degree of supersaturation on ascent and the likelihood and potential magnitude of a second nucleation event at shallower depths which occurs just prior to fragmentation according to the model of Massol and Koyaguchi (2005). Their model predicts that melts with high surface tensions (a proxy for homogeneous nucleation) should erupt effusively. Since, in reality, high surface tension rhyolite magmas containing 4 wt.% water tend to erupt explosively this suggests that heterogeneous nucleation should be common in nature.

The modeling study of Massol and Koyaguchi (2005) reiterates the importance of the experimental approach to nucleation in providing reasonable surface tension estimates for hydrated melts in order to predict their eruptive behavior. These estimates are derived from experiments where a single homogenous nucleation event is assumed to have occurred. A method which can verify that assumption would have significant value.

Methods

Thin sections of the experimental samples were first prepared by embedding the samples in epoxy, mounting on microscope slides and polishing finely. A series of photomicrographs were taken in reflected light of the finely polished sample in an overlapping grid fashion using a micrometer slide holder, ensuring that each photomicrograph overlapped its neighbor by ~40%. The images in this study were taken at 100X with a Leica DM LM/P petrographic light microscope and Leica DF320 digital camera with a camera resolution of 2.98 pixels /micron. A photomontage was created from these images in Adobe Photoshop recreating a high resolution whole sample image.

The perimeter of the sample was traced within the NIH ImageJ program (Rasband, 1997-2007) and the coordinates of the perimeter exported as a text file. Using image thresholding to highlight the bubbles, the coordinates of the centroids of the bubbles intersecting the surface were also determined and exported as a text file. Figure 4.1 shows examples of a bubble nucleation experiment image, photomontage, thresholded image, and centroids analyzed by ImageJ and plotted as a point pattern in panel D.

The bubble centroid dataset was imported into Spatstat, a spatial analysis package, for derivation of the spatial distribution functions. Where other packages require the window to be of a regular shape (rectangle etc.), Spatstat is unique in the use of an arbitrary window. This allows analysis of the entire sample at once, which is a more rigorous statistical approach and particularly useful for examination of experimental samples where the nucleation pattern may differ between the edge and center of the sample. Detailed instructions for loading the bubble centroid dataset and deriving fundamental data can be found in Appendix 1.

Spatial Statistics

Point Pattern Analysis

Before describing the application of statistical spatial point pattern analysis, it is important to recognize two assumptions in the method: The underlying process is assumed to be stationary (invariant under translations) and isotropic (invariant under rotations) and the statistical averages can be expressed as the limit of a spatial average. This allows statistical inference to proceed from a single sample.

To aid in quantifying differences between samples, the observed spatial point patterns are usually compared to a reference model that corresponds to complete spatial randomness, the stationary Poisson Point Process. Point patterns can then be classified as being more aggregated/clustered or more regular than a distribution arising from a Poisson process with the same intensity or density of events. Following from this, there are a number of useful distribution functions that can be derived from the point pattern of interest, and applied specifically to decipher bubble nucleation processes, as follows.

Nearest Neighbor Distribution Function G(r)

A simple description of the spatial distribution of the bubbles is based on the measurement of the distance from the center of the intersection of a typical bubble to the centre of its nearest neighbor. The nearest-neighbor cumulative distribution G(r) at a radius r is defined as follows where P() denotes probability.

$$G(r) = P(\text{distance from a typical point to the nearest point of process} \leq r) \tag{2}$$

For the stationary Poisson point process of intensity λ, the G function $G_{Poiss}(r)$ is given by

$$G_{Poiss}(r) = 1 - e^{(-\lambda \pi r^2)} \tag{3}$$

For a homogenously nucleated bubble population, G(r) should approach $G_{Poiss}(r)$. Comparing G(r) for the sample with $G_{Poiss}(r)$ highlights any clustering or spatial regularity in the intersected bubble population (e.g. Figure 4.2).

Ripley's K-Function

Ripley's K function K(r) or the reduced second moment distribution of a point process is a good first order test of homogeneity highlighting over what length scale the point pattern can be said to be homogeneous:

$$K(r) = \frac{E((\text{Number of Points within r of typicalpoint}) - 1)}{\lambda} \tag{4}$$

For the Poisson process which has intensity, λ.

$$K_{Poiss}(r) = \pi r^2 \tag{5}$$

For a homogeneously nucleated bubble population, K(r) should approximate $K_{Poiss}(r)$ at all length scales.

A commonly-used transformation of K(r) is the L-function given by Eq.(6) which transforms the Poisson K function to the straight line $L_{Poiss}(r) = r$, making visual assessment of the graph much easier (e.g. Figure 4.3).

$$L(r) = \sqrt{\frac{K(r)}{\pi}} \tag{6}$$

Non Poisson models

A large number of non Poisson point process models exist and for a true 2D dataset it can useful to test the fit of the data against these in order to elucidate the underlying mechanism. The spatial point pattern derived from intersected bubbles, however, is not

suitable for this more sophisticated analysis. The processes controlling the observed spatial point pattern are controlled by the initial 3D distribution of nucleated bubbles and the sizes of these bubbles. As the bubbles are not all the same size it is not possible, for instance, to figure out whether two points are far apart because the bubbles which are intersected are actually far apart or because we are looking a different cross sections. For instance, two bubbles could be touching in 3D but if the polished section intersects just the very top, they will look to be far apart. However, comparing the distributions with those arising from simple models can be instructive in some cases. In this study the expected distributions arising from a Matern II Model are derived. In this model, the points of a homogeneous Poisson process are marked by 'arrival times' which are independent and uniformly distributed. Any point that lies closer than a distance, r (set to the smallest measured true bubble diameter), from another point that has an earlier arrival time, is deleted. See Appendix 1 for more application details.

Application of Spatstat to bubble nucleation experiments

Homogeneous nucleation: Sample RN1b

Sample RN1B was conducted to replicate homogeneous bubble nucleation in rhyolite melt under similar conditions to those employed by Mangan and Sisson (2000). It shows two populations of bubbles: one nucleated around the edges, and one forming a "cloud" with high bubble number density in the center (Figure 4.4(A)). Figure 4.4(C) shows a contoured density map of the spatial point pattern (Figure 4.4(B)) derived from the bubble centroids from a thin section of sample RN1B. The bubble number density varies

by an order of magnitude across the intersected sample from ~5 x 10^3 bubbles cm^{-2} to ~4 x 10^4 bubbles cm^{-2}, with the highest bubble number density in the center of the sample surrounded by a region containing the lowest bubble number densities (Figure 4.4(C)). Figure 4.4(B) confirms that a high bubble number density is found in the center of the sample and is surrounded by an essentially bubble free area. The sample edges have intermediate bubble number densities.

The spatial statistics functions G(r) and L(r) are shown in Figure 4.2 and Figure 4.3, compared to the distributions expected from a Poisson process, $G_{Poiss}(r)$ and $L_{Poiss}(r)$, with the same average intensity and a Matern II model with a minimum spacing of 16 μm. Figure 4.2 shows the sample G(r) plots below $G_{Poiss}(r)$ for r<~40 μm showing a similar distribution to the MaternII model for r<~35 μm and above $G_{Poiss}(r)$ for r <100 μm. Using the isotropic corrected method, L(r) plots below $L_{Poiss}(r)$for r<36 μm with L(r) =0 for r<18 μm and above $L_{Poiss}(r)$ for values of r>36 μm. The Matern II model distribution is again similar for r<~35 μm. Performing similar modeling using a subset of bubbles in a window reduced by 500 microns from the original (Figure 4.5) results in a dramatically different calculated G(r) (Figure 4.6). Here, G(r) plots dramatically above $G_{Poiss}(r)$ for all r > 24 μm with 95% of nearest neighbor distances occurring at less than 80 μm compared with less than 166 μm for $G_{Poiss}(r)$.

Based on visual observations (Mangan and Sisson, 2000), RN1B underwent homogeneous bubble nucleation, producing the high bubble number density in the sample center. The bubbles at the sample edge are assumed to have nucleated heterogeneously and the two bubble populations are considered to be independent. Spatstat allows further

details to emerge beyond those derived from visual recognition alone. For a clustered arrangement where the distance between points is shorter than would be expected from a Poisson distribution with the same overall intensity, G(r) and L(r) are expected to plot above $G_{Poiss}(r)$ and $L_{Poiss}(r)$ respectively. Analyzing the whole sample in RN1B results in the G(r) curve (Figure 4.7) crossing where part of the bubble population can be classified as being more clustered and the other as being more regularly spaced. In this case, we can clearly see that the internal and edge bubbles represent two independent bubble populations and that a description of the sample is not well served by using a single point process model.

Considering only the internally nucleated bubbles (Figure 4.6 and Figure 4.8), G(r) plots above $G_{Poiss}(r)$, indicating that the bubbles are more clustered than would be expected from a Poisson distribution with the same average intensity. However the slope of G(r) also indicates that the bubbles are somewhat regularly spaced within the cluster. This correlates well with the observations of spatial regularity made by Mourtada-Bonnefoi and Laporte (2004) from similar nucleation experiments. Interestingly, we should not expect such spatial regularity in a theoretical homogeneously nucleated melt, since the spatial pattern should plot closer to the completely spatially random Poisson distribution. Despite issues with the cut effect, and direct applications of the models as a result, the distinct signature in G(r) of the internal nucleated bubbles in sample RN1B may be used to quantify "homogeneous" nucleation beyond simple visual recognition.

Heterogeneous nucleation: Samples 79VB2C and 79VB2d

The spatial bubble distributions in Samples 79VB2C and 79VB2D are complex (Figure 4.9 and Figure 4.10) and neither sample is considered to have undergone a simple homogeneous nucleation step. The complex spatial point pattern may derive from multiple nucleation events which could be homogeneous and/or heterogeneous. Through analysis of the spatial point patterns of the two samples, significant differences in point patterns are revealed which suggest that the complex bubble patterns in each sample derived from different processes.

Figure 4.8 shows a contoured density map of the spatial point pattern derived from sample 79VB2C. The bubble number density varies by an order of magnitude across the sample surface, from ~2x 10^4 bubbles cm^{-2} to ~1.4 x 10^5 bubbles cm^{-2}, yet without clear organization between separate edge and interior bubble populations as in RN1B. G(r) for sample 79VB2C is shown in Figure 4.10, compared to the distribution expected from a Poisson process, $G_{Poiss}(r)$, with the same average intensity and a Matern II model with a minimum spacing of 5μm. The observed G(r) is less than $G_{Poiss}(r)$ for all r indicating that the points in general are more widely spaced that would be expected from a Poisson distribution. In Figure 4.11 plots of G(r) for subsets of points within windows reduced by 50 and 200μm do not differ greatly from G(r) for the whole sample.

Figure 4.9 shows a contoured density map of the spatial point pattern derived from sample 79VB2D where the bubble number density varies from ~1 x 10^4 to 5 x 10^5, with a high concentration of edge located bubbles. In Figure 4.12, the calculated G(r) distribution is plotted for subsets of points found in windows eroded from the original by

10, 50, 100 and 200μm, plotted for comparison with the base distribution and $G_{Poiss}(r)$. The base curve sits above $G_{Poiss}(r)$ until G(r) is ~0.65 for r ~20μm. Reducing the observation window by 10μm does not change G(r) significantly. Further reductions by 50μm increments dramatically reduce the point at which G(r) crosses $G_{Poiss}(r)$ to 0.5. Further reductions up to 200μm reduce the crossover point to 0.38, effectively describing a reduction in the proportion of clustered bubbles as the window is eroded.

Whilst it was clear in sample RN1B that the nucleation pattern should be split into separate internal and edge nucleated bubble populations, the complexities of the point patterns in the other samples mean that such a straightforward distinction is not possible. However observation of the change in G(r) for a narrowing of the window of observation away from the sample edge enables us to differentiate further between the two samples and hints at differences in underlying nucleation mechanism. From Figure 4.10, we see that the spatial point pattern in sample 79VB2C is more regular than we would expect from a Poisson distribution with the same point intensity. Reducing the window of observation away from the sample edge has little effect on G(r) even for a large reduction of 200 μm, (Figure 4.10) suggesting that there is little difference in the spatial distribution of points at the sample edge and in the center and therefore that the controls on nucleation of bubbles close to the sample edge are similar to those for nucleation of "internal" bubbles. This suggests the bubbles in 79VB2C are not clearly separable into two distinct periods of nucleation, from two different mechanisms. More likely, the bubbles in 79VB2C represent a heterogeneously nucleated population(s), possibly over several time intervals.

In contrast, in Figure 4.12, the G(r) distribution from sample 79VB2D changes dramatically as the window is eroded by 50μm and 200μm. Reducing the observation window here effectively reduces the number of clustered points in the pattern, pointing to bubble clusters being more dominant close to the sample edge.

The significance of the deviations are illustrated in Figure 4.7 which shows the +-5% significance envelope for $G_{Poiss}(r)$ derived from Monte Carlo modeling (See Appendix 1 for details) , compared with G(r) for sample 79VB2D. G(r) plots outside of the significance envelope, inferring that it is a true deviation.

Summary

Application of the 2D spatial statistics model, Spatstat, to bubble nucleation experiments demonstrates a powerful method that will enable researchers to quantify bubble nucleation mechanisms and discriminate between samples with complex bubble textures. This model offers an improvement over simple visual recognition of bubble populations, used to discriminate between nucleation mechanisms qualitatively. Application of an eroding window can provide quantification of the length scales over which bubble populations' change within the experiments, a clear step forward in quantification of complex textures, such as those seen in 79VB2C and 79VB2D. Future applications could include quantification of multiple nucleation events by applying a combination of the eroding window technique with marked point processes. Bubbles resulting from separate nucleation events may be distinguishable by their size. By adding marks to each bubble according to a specified size range, the spatial characteristics of each bubble population

may be analyzed separately, and in relation to other subsets. This could provide a way to estimate the timing and resulting bubble number densities resulting from separate nucleation events within one experimental sample. To date, this has not been reproduced by experimental studies because of the intractable nature of identifying and separating different populations using standard bubble measurement techniques (e.g. (Gardner et al. (1999) and Mangan and Sisson (2000). This method could also provide interpretations of how the different bubble populations affect one another, as new nucleation events occur amidst pre-existing bubbles. Also, marked point process models could be applied to crystal nucleation in order to understand the spatial dependence of crystal nucleation on prior nucleated crystals. Proper application of point process modeling could thus help transform our ability to interpret and apply experimental studies to volcanic processes.

One of the drawbacks of the Spatstat method is that it currently is applied to two dimensional, experimental sample surfaces through reflectance light photomicrographs. Without a detailed knowledge of the sizes of the bubbles, it is not possible to "correct" the observed 2D relationships to 3D. Sahagian and Proussevitch (1998) proposed a method based on the technique of Stoyan et al. (1995) but it requires the knowledge of the true sizes of many more bubbles to be measured than is possible from experimental samples. 3D spatial analysis is computationally much more intensive and more difficult to do but some researchers have been making progress (See Baddeley et al. (1993) and Reed et al. (1997) for two examples). Advances in this field may in the future allow spatial point pattern analysis of 3D images of natural samples created by x-ray tomography or confocal microscopy. At present, experimental samples are still too small

for routine 3D computed x-ray tomography. However, it is likely that advances over the next few years will provide a new method by which the experiments may be analyzed in 3D. This will allow for rigorous application of the spatial statistics to be performed on the experimental samples, without loss of accuracy due to the cut effect.

References

Avrami, M., 1940. Kinetics of phase change I: General theory. Journal of Chemical Physics(7): 1103-1112.

Baddeley, A. and Turner, R., 2005. Spatstat: an R package for analyzing spatial point patterns. Journal of Statistical Software, 12(6): 1-42.

Baddeley, A.J., 1998. Spatial sampling and censoring. In: O.E. Barndorff-Nielsen, W.S. Kendall and M.N.M. Van Lieshout (Editors), Stochastic Geometry: Likelihood and Computation. Chapman and Hall, London, pp. 37–78.

Baddeley, A.J., Moyeed, R.A., Howard, C.V. and Boyde, A., 1993. Analysis of a three dimensional point pattern with replication. Applied Statistics, 42(4): 641-668.

Cox, T.F., 1979. A method for mapping the dense and sparse regions of a forest stand. Applied Statistics, 28: 14-19.

Diggle, P.J., Lange, N. and Benes, F.M., 1991. Analysis of variance for replicated spatial point patterns in clinical neuroanatomy. Journal of American Statistical Association, 86: 618-625.

Gardner, J.E., Hilton, M. and Carroll, M.R., 1999. Experimental constraints on degassing of magma; isothermal bubble growth during continuous decompression from high pressure. Earth and Planetary Science Letters, 168(1-2): 201-218.

Hirth, J.P., Pound, G.M. and St. Pierre, G.R., 1970. Bubble Nucleation Metallurgical and Materials Transactions, 1.

Hurwitz, S. and Navon, O., 1994. Bubble nucleation in rhyolitic melts; experiments at high pressure, temperature, and water content. Earth and Planetary Science Letters, 122(3-4): 267-280.

Johnson, W.A. and Mehl, R.F., 1939. Reaction kinetics in processes of nucleation and growth. Transactions of the Metallurgical Society of AIME 135: 416-442.

Kolmogorov, A.N., 1937. Statistical theory of metals crystallization. Bulletin of the Academy of Science, USSR, Series Mathematics(3): 355-359.

Mangan, M. and Sisson, T.W., 2000. Delayed, disequilibrium degassing in rhyolite magma; decompression experiments and implications for explosive volcanism. Earth and Planetary Science Letters, 183(3-4): 441-455.

Massol H. and Koyaguchi T., 2005. The effect of magma flow on nucleation of gas bubbles in a volcanic conduit. Journal of Volcanology and Geothermal Research 143(3-4):69-88

Mourtada-Bonnefoi, C.C. and Laporte, D., 2004. Kinetics of bubble nucleation in a rhyolitic melt; an experimental study of the effect of ascent rate. Earth and Planetary Science Letters, 218(3-4): 521-537.

Peebles, P.J.E., 1974. The nature of the distribution of galaxies. Astronomy and Astrophysics, 32: 197-202.

R Development Core Team, 2007. R: A language and environment for statistical computing. R Foundation for Statistical Computing, Vienna, Austria.

Rasband, W.S., 1997-2007. ImageJ. U. S. National Institutes of Health, Bethesda,MD.

Reed, M.G., Howard, C.V. and Shelton, C.G., 1997. Confocal imaging and second order stereological analysis of a liquid foam. Journal of Microscopy, 185(3): 313-320.

Russ, J.C., 1998. The Image Processing Handbook. CRC Press, Boca Raton, FL.

Sahagian, D.L. and Proussevitch, A.A., 1998. 3D particle size distributions from 2D observations; stereology for natural applications. Journal of Volcanology and Geothermal Research, 84(3-4): 173-196.

Stoyan, D., Kendall, W. and Mecke, J., 1995. Stochastic Geometry and its Applications. John Wiley and Sons, Chichester.

Toramaru, A., 1989. Vesiculation process and bubble size distributions in ascending magmas with constant velocities. Journal of Geophysical Research, B, Solid Earth and Planets, 94(12): 17,523-17,542.

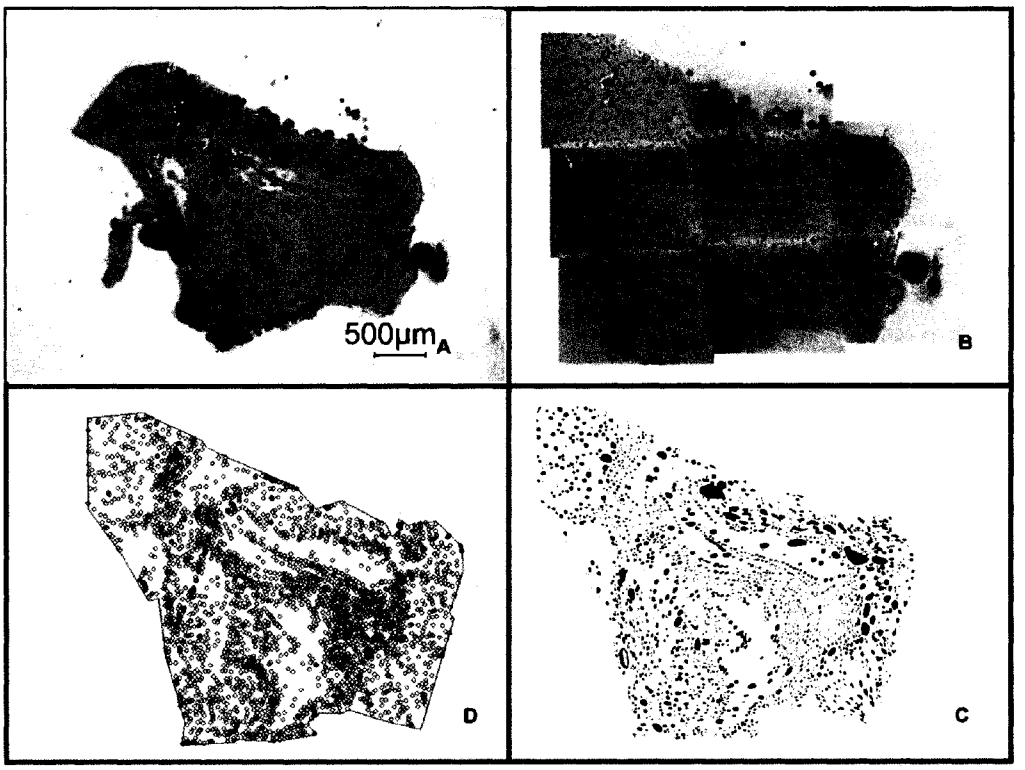

Figure 4.1 Workflow illustration for creation of spatial point patterns from experimental nucleated samples.
A- Overview Photomicrograph. B- Sample Photomontage, C- Threshold Image. D- Spatial Point Pattern.

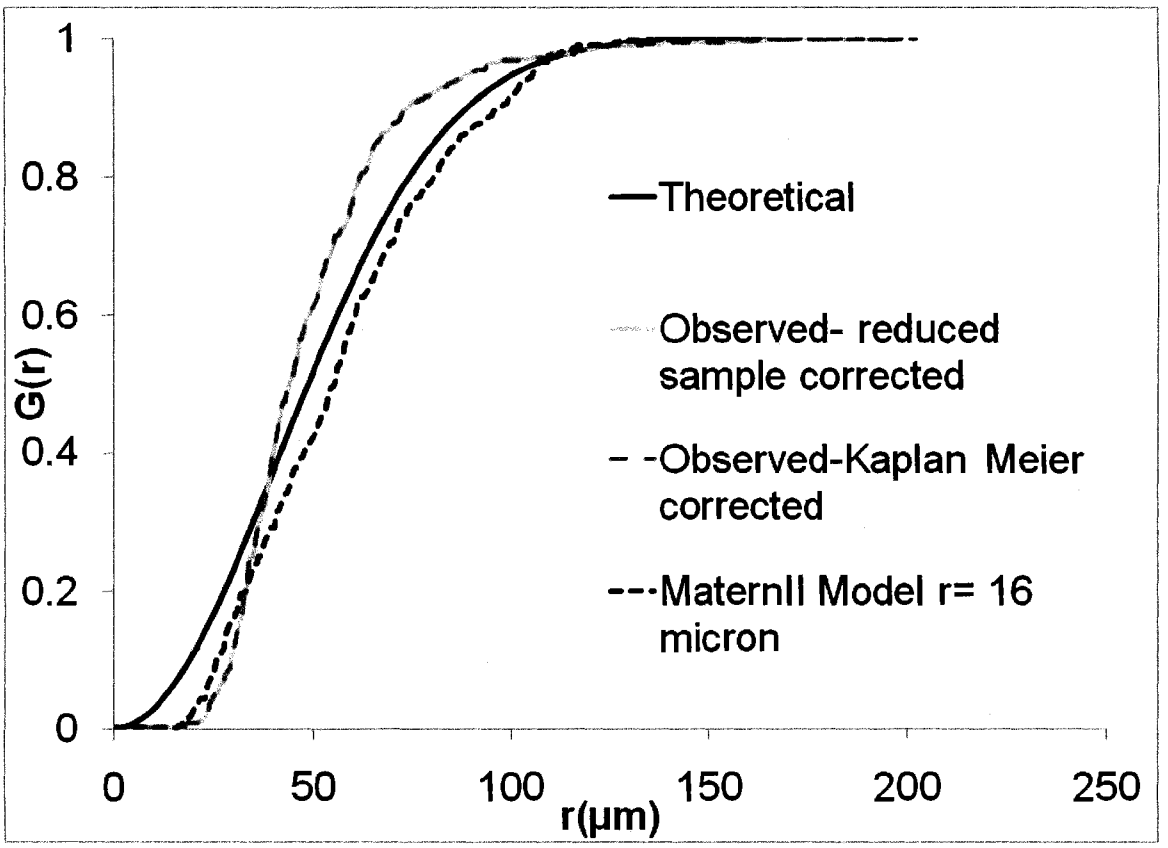

Figure 4.2. G(r) vs. $G_{Poiss}(r)$ for sample R1NB.
Edge corrected nearest neighbor cumulative distributions, G(r), for sample RN1B plotted against the expected distribution from a Poisson distributed point pattern $G_{Poiss}(r)$ of same intensity. Solid black line is $G_{Poiss}(r)$, solid light grey Line is G(r) after reduced sample correction, and dashed dark grey line is G(r) after Kaplan-Meier correction.
Dashed black line is the distribution derived from a Matern II model with minimum separation of 16µm.

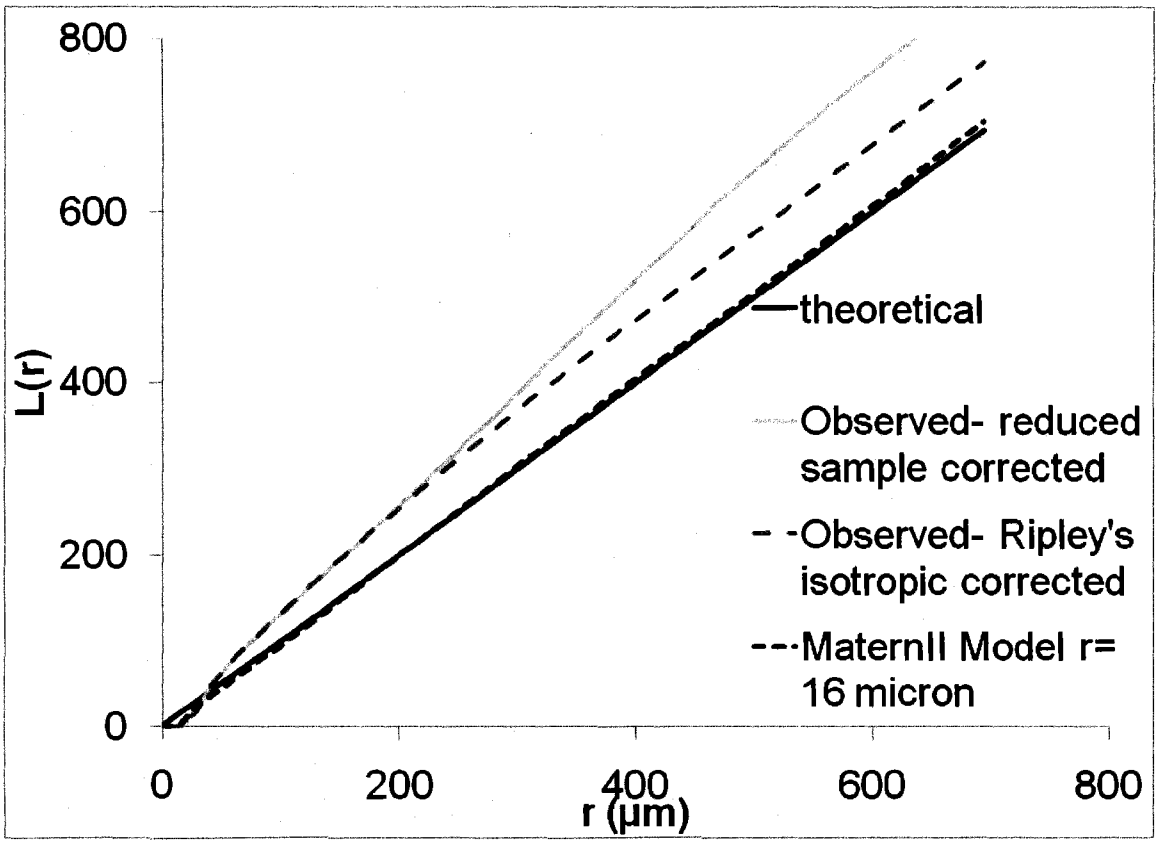

Figure 4.3 L(r) vs. $L_{Poiss}(r)$ for sample RN1B.
Edge corrected nearest neighbor cumulative distributions, L(r), for sample RN1B plotted against the expected distribution from a Poisson distributed point pattern $L_{Poiss}(r)$ of same intensity. Solid black line is $G_{Poiss}(r)$, solid light grey Line is G(r) after reduced sample correction, and dashed dark grey line is G(r) after Kaplan-Meier correction.
Dashed black line is the distribution derived from a Matern II model with minimum separation of 16µm.

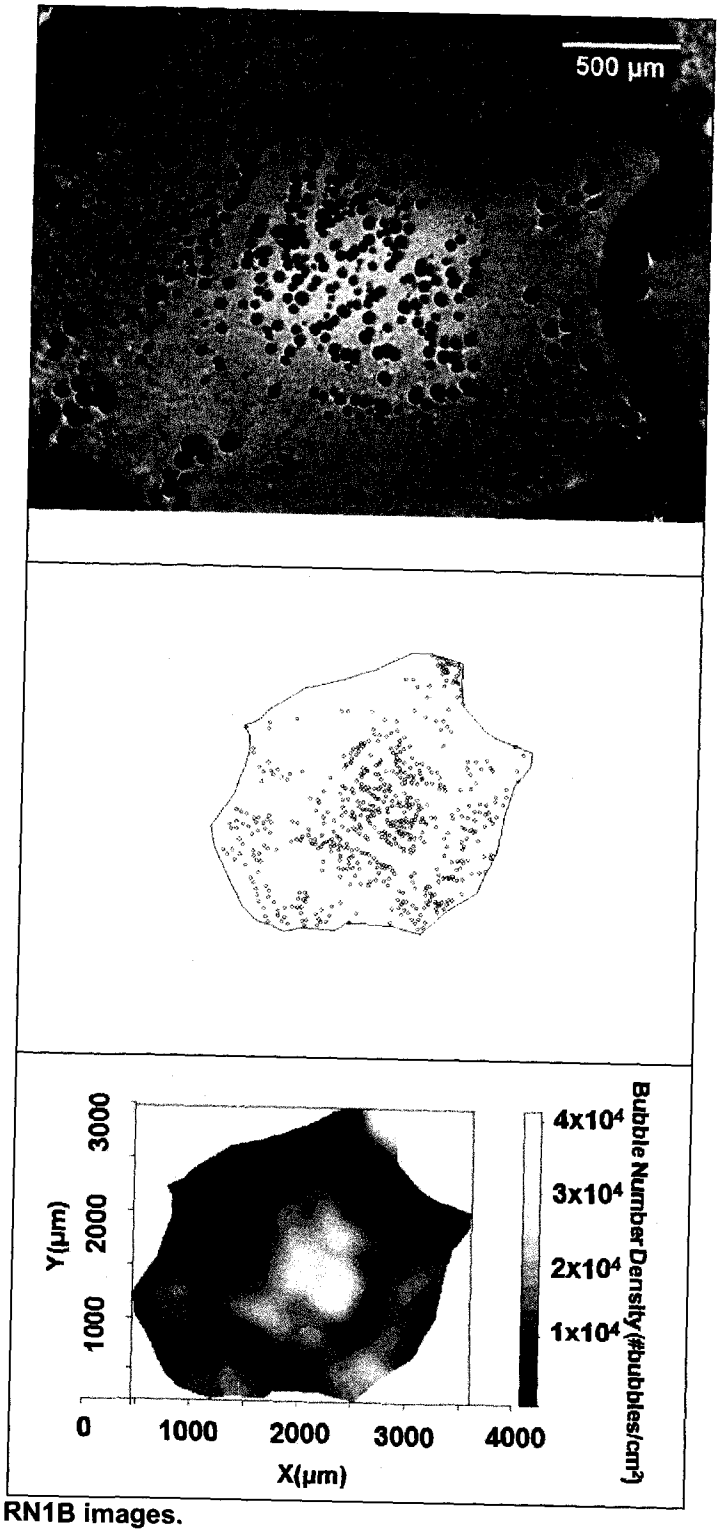

Figure 4.4 Sample RN1B images.
(A) Overview photomicrograph. (B) Spatial point pattern. (C) Bubble number density plot, kernel size is 100.

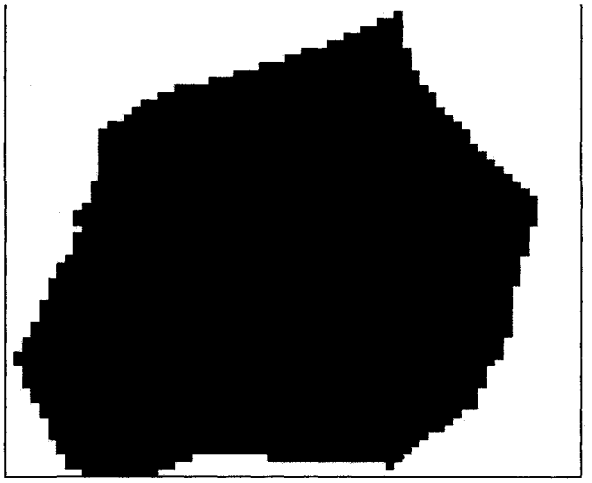

Figure 4.5 Subset of points for sample RN1B within window reduced by 500pm.

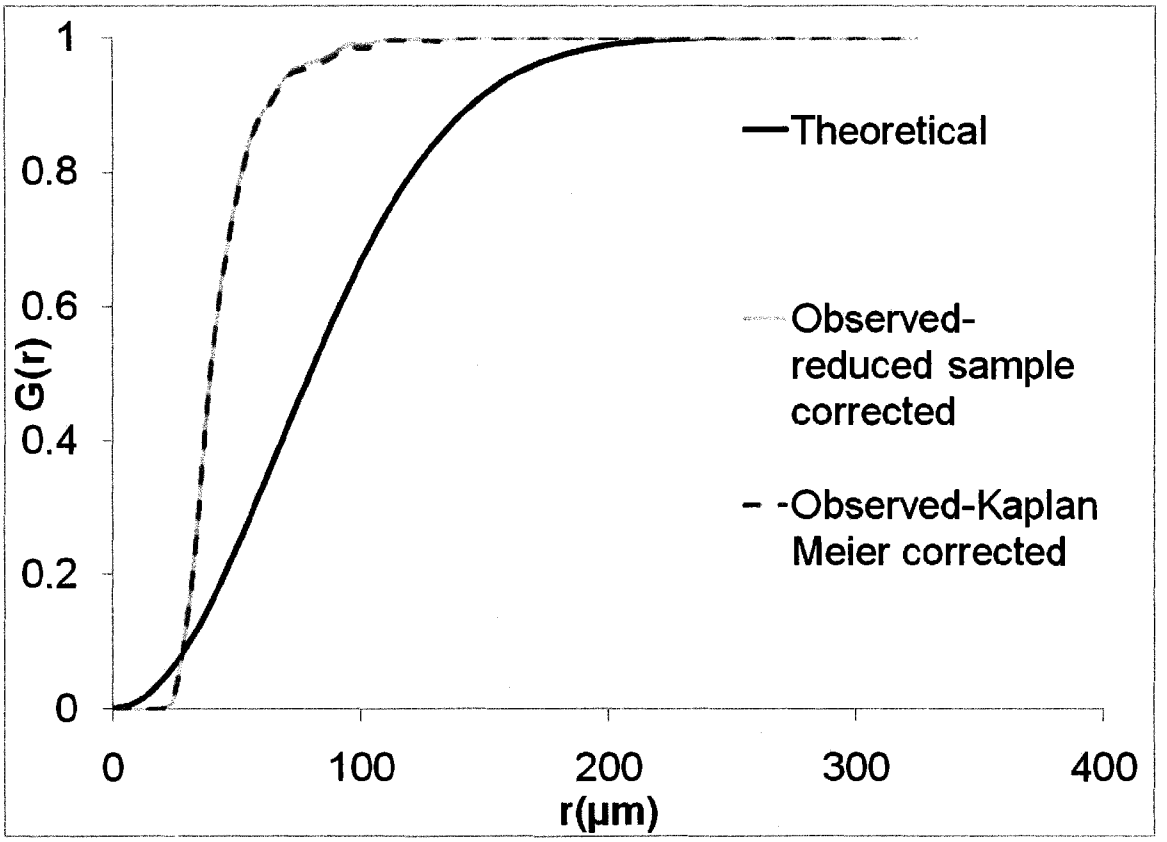

Figure 4.6 G(r) vs $G_{Poiss}(r)$ for subsets of sample RN1B derived from 500 µm reduction in window size.
Edge corrected nearest neighbor cumulative distributions, G(r), for subsets of sample RN1B derived from 500 µm reduction in window size plotted against the expected distribution from a Poisson distributed point pattern $G_{Poiss}(r)$ with the same average intensity of the whole sample. Solid black line is $G_{Poiss}(r)$, solid light grey line is G(r) after reduced sample correction, and dashed dark grey line is G(r) after Kaplan-Meier correction.

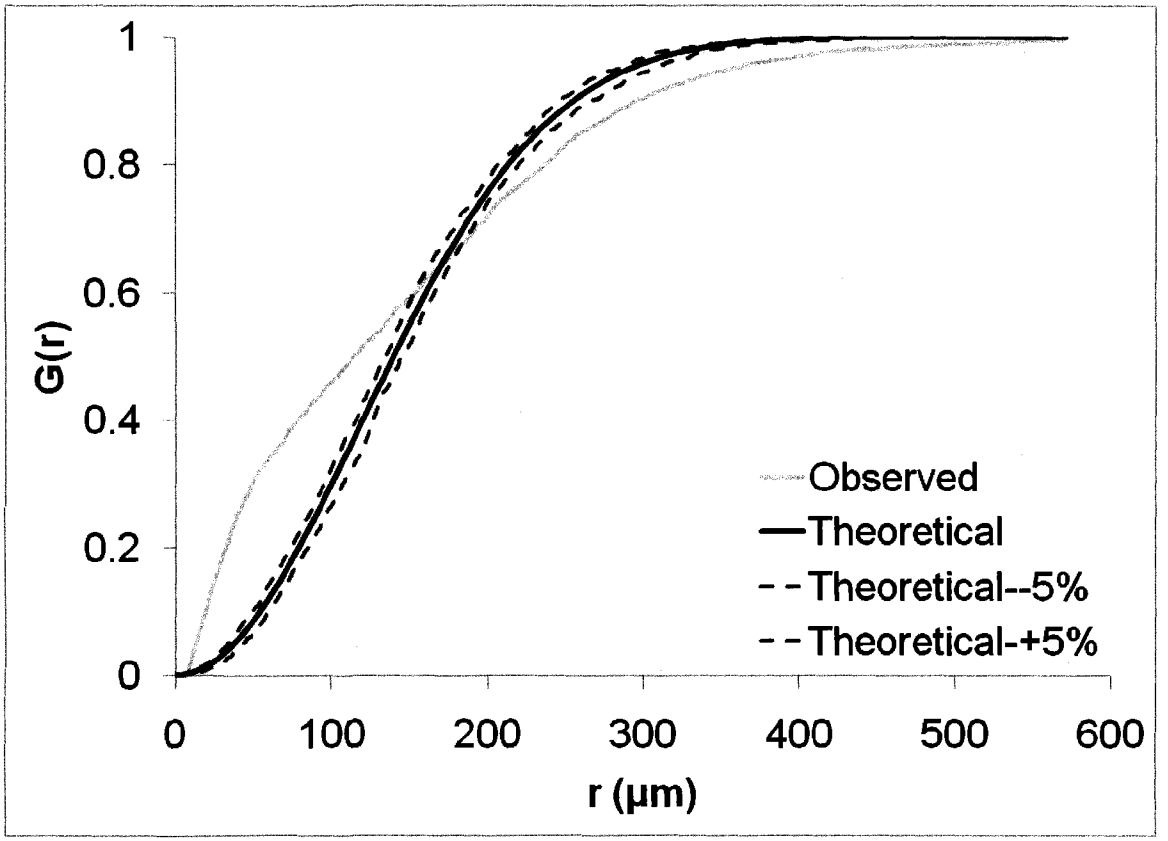

Figure 4.7 $G_{Poiss}(r)$ and G(r) for sample 79VB2D within 5% significance envelope. $G_{Poiss}(r)$ (solid black line) for sample 79VB2D plotted within 5% significance envelope (dashed lines) generated from Monte Carlo simulations plotted against G(r) (light grey line) for same sample.

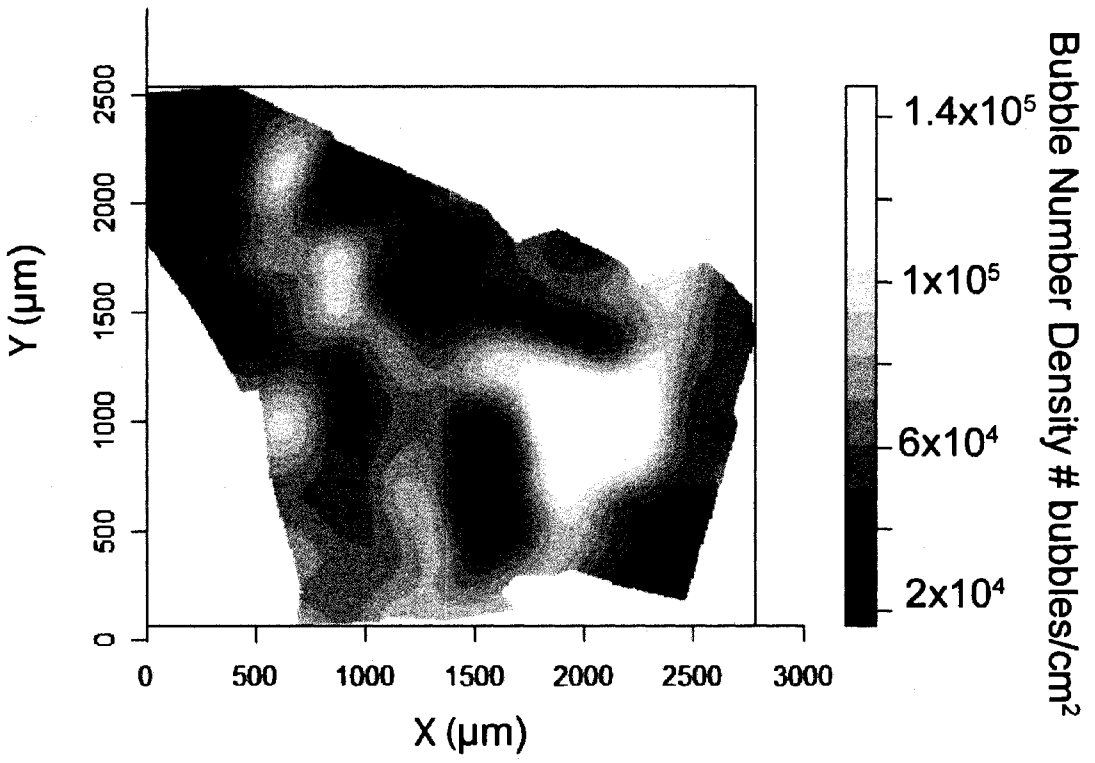

Figure 4.8 Bubble number density plot for 79VB2C. Kernel size is 100.

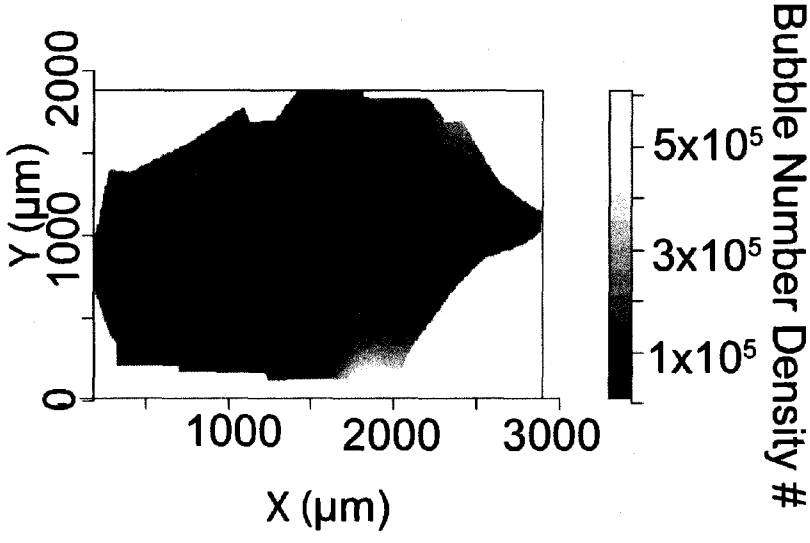

Figure 4.9 Bubble number density plot for 79VB2D. Kernel size is 100.

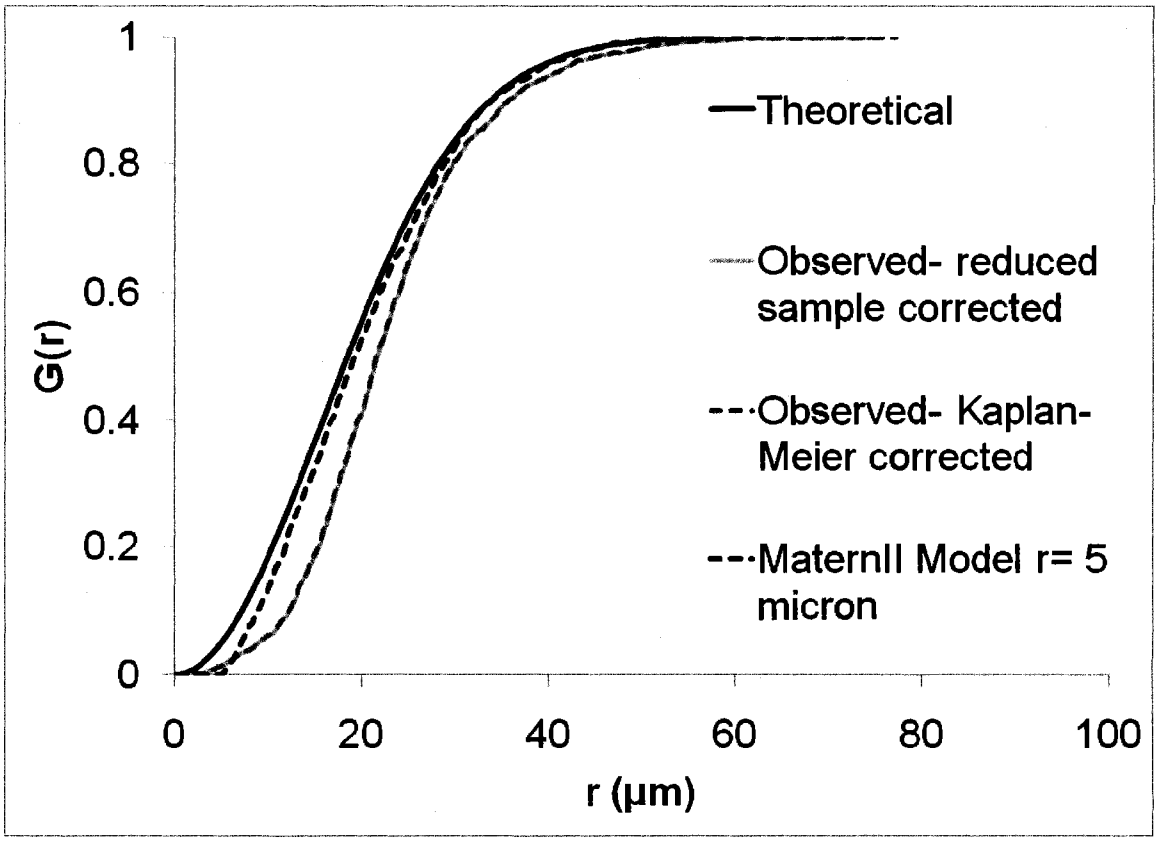

Figure 4.10 G(r) vs $G_{Poiss}(r)$ for sample 79VB2C.
Edge corrected nearest neighbor cumulative distributions, G(r), for sample 79VB2C plotted against the expected distribution from a Poisson distributed point pattern $G_{Poiss}(r)$ of same intensity. Black line is $G_{Poiss}(r)$, light grey line is G(r) after reduced sample correction, and dashed dark grey line is G(r) after Kaplan-Meier correction. Dashed black line is the distribution derived from a Matern II model with minimum separation of 5µm.

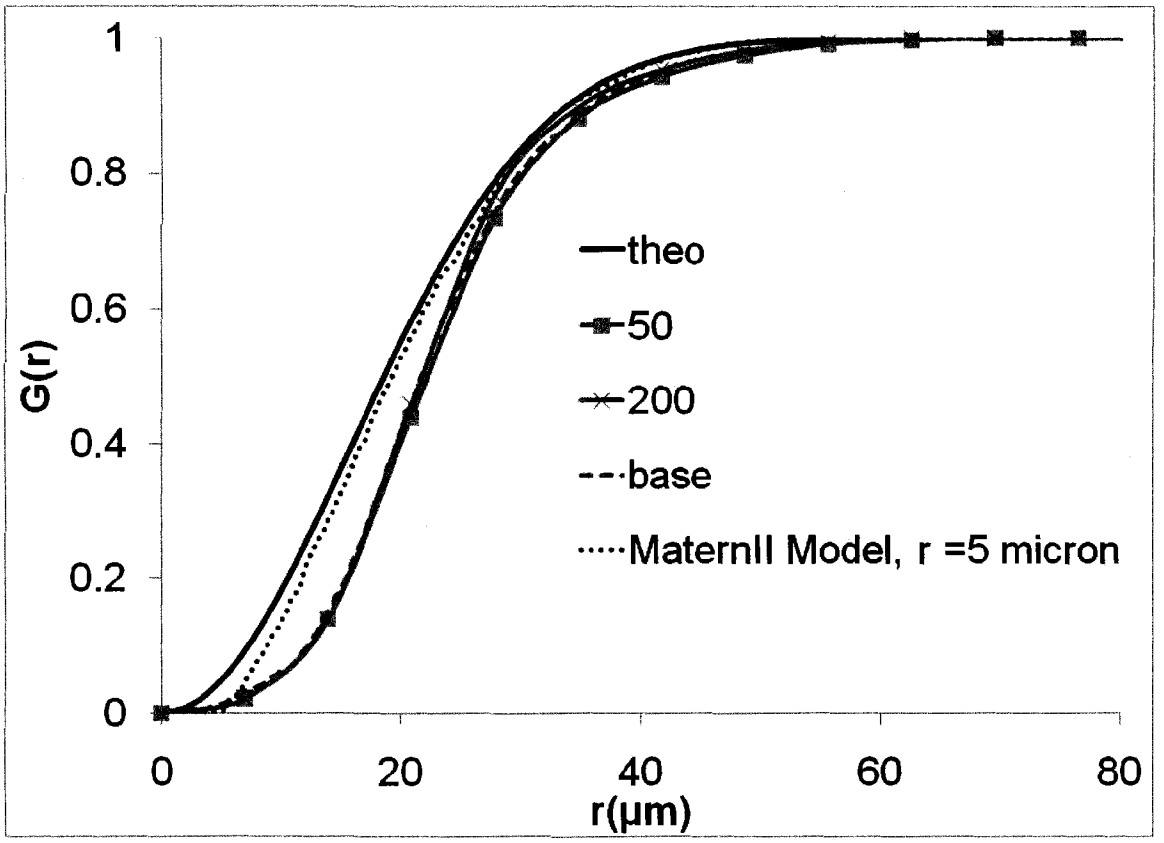

Figure 4.11 G(r) vs $G_{Poiss}(r)$ for subsets of sample 79VB2C derived from reductions in window size.
Kaplan-Meier edge corrected nearest neighbor cumulative distributions, G(r), for subsets of sample 79VB2C derived from reductions in window size (50μm and 200μm) plotted against the expected distribution from a Poisson distributed point pattern $G_{Poiss}(r)$ with an average intensity of the whole sample. Black line is $G_{Poiss}(r)$, dashed dark grey line is G(r) for whole sample, square markers for reduction of 50μm, and cross markers for reduction of 200μm. Dashed black line is the distribution derived from a Matern II model with minimum separation of 5μm.

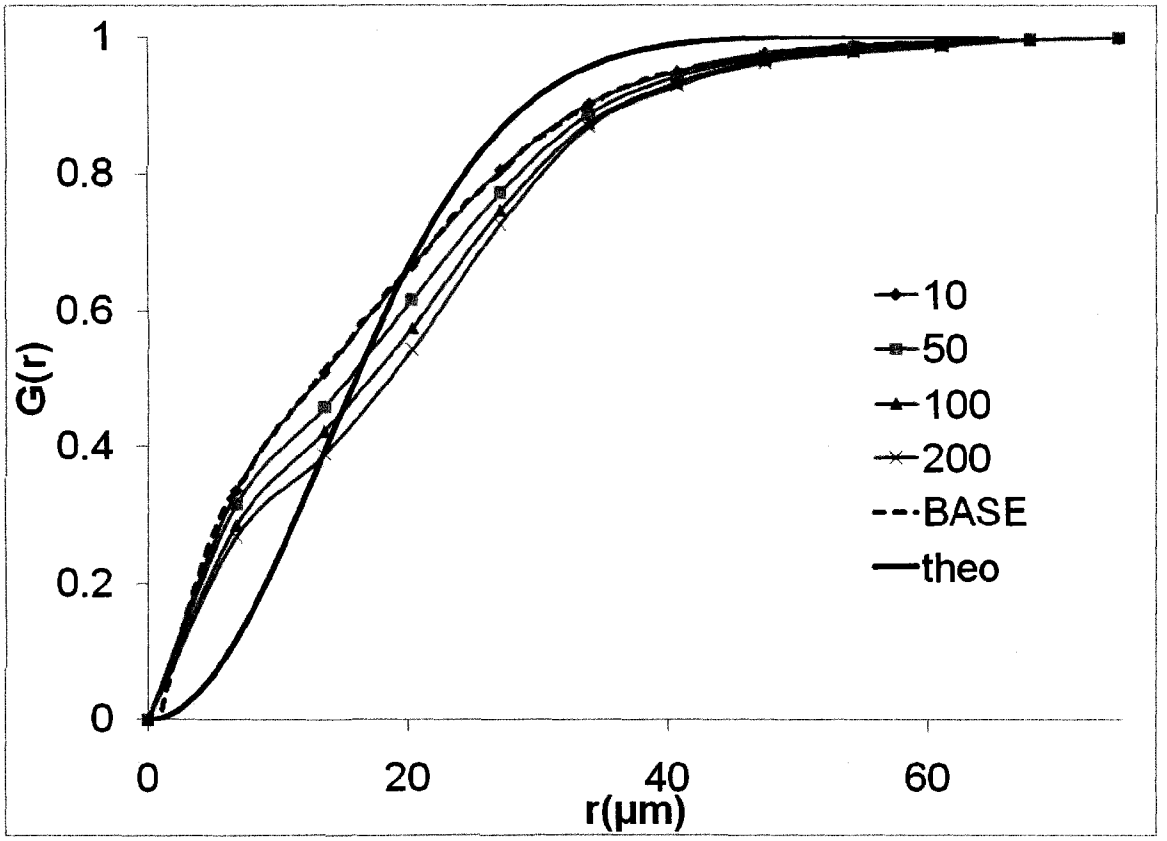

Figure 4.12 G(r) vs $G_{Poiss}(r)$ for subsets of sample 79VB2D derived from reductions in window size.
Kaplan-Meier edge corrected nearest neighbor cumulative distributions, G(r), for subsets of sample 79VB2D derived from reductions in window size (10µm to 200µm reductions) plotted against the expected distribution from a Poisson distributed point pattern $G_{Poiss}(r)$ with an average intensity of the whole sample. Solid black line is $G_{Poiss}(r)$, dashed dark grey line is G(r) for whole sample, diamond markers for reduction of 10µm, square markers for reduction of 50µm, triangle markers for reduction of 100µm and cross markers for reduction of 200µm.

Chapter 5 Investigating shallow dike intrusions using a particle code

Abstract

We present a study of shallow dike intrusion behavior through weak sandstone and strong granite using a particle code model which focuses on the fracture mechanics of dike propagation. Using this approach, the change in mechanical properties within the process zone which develops ahead of an intrusion is modeled concurrently with the intrusion. The effect of localized stresses resulting from the intrusion on further dike growth can also be assessed. Starting from small models calibrated with laboratory tests, an upscaled set of models with dimensions of 500m (width) by 100m (height) and an upper depth of 100m are used to investigate intrusion behavior in homogeneous and layered models under lithostatic, compressive (+2GPa) and extensional (-2GPa) regimes. The model results show observed field relations such as extensive microfracturing across the weaker sandstone layers and parallel dike jointing at distances of 10's of meters in the stronger granite layers. Intrusion in the weak sandstone layers proceeds through dissipative growth after extensive microfracturing generating intrusions with widths of 10's of meters. Intrusion into granite proceeds by the buildup of a critical strain within the granite layer leading to a crack propagating across the layer followed by magma invasion. Typically the intrusions widths are somewhat less than in the sandstone. Compressional and extensional regimes both act to retard intrusion growth towards the surface. In the compressive regime, doming of overlying layers is preferred over dike propagation. In

the extensional regime, lateral growth is preferred over propagation. A scaled dependence to fracture toughness is also observed to emerge from the modeling.

Although the scale of the intrusions are an order of magnitude greater than field observations, this study suggests that the particle code method with some modifications can provide insights into the complex mechanism of dike intrusion at shallow depths which cannot be obtained though the current analytical or continuum models.

Introduction

Magma driven fractures with vertical orientation are termed dikes and those with horizontal orientations are called sills. They are important for magma transport in the lithosphere and also as volcanic eruption feeders (Gudmundsson 2002; Gudmundsson and Brenner 2005; Stewart et al. 2003). In volcanically active settings, intrusion-induced seismicity (Patane et al. 2002) and surface deformation (Ito and Yoshioka 2002) are essential input parameters for eruption forecasts. Older intrusion complexes are often of interest for their associated mineral deposits.

Dike propagation is a complex process dependent on buoyant rise, fracture and fluid mechanics. It was assumed that most dikes acted as feeders to eruptions (Macdonald 1972; Williams and McBirney 1979); however, recent studies have concluded that many more dikes are injected into composite volcanoes and rift zones than are observed at the surface (Gudmundsson 1995; Gudmundsson 2002; Marinoni and Gudmundsson 2000). The mechanics which allow or prevent a dike reaching the surface are not well understood. Since the intrusions, however, tend to be of a similar density to the

surrounding rock, buoyant rise is probably not the controlling mechanism at shallow depths.

Field Observations

Field observations indicate several processes may occur when a propagating dike passes from one layer to another. If the layers are mechanically similar and welded at the contact, the dike may propagate through the contact with little change in course. A contrast in layer properties, however, tends to result in one of the following scenarios: sill formation, enhanced vertical propagation, dike offset at the contact or dike arrest with a blunt or tapering end. Tomography studies (Foulger and Toomey 1989; Lees 1992; Patane et al. 2002; Sherburn et al. 2003; Stefano and Chiarabba 2002) have revealed that high contrasts in elastic/mechanical parameters exist at shallow depths in many volcanic settings. They may be the result of alternating lava/ash layers as in stratavolcanoes or due to the presence of existing solidified intrusions. A better understanding of how dike propagation would be affected by these is critical to our ability to predict volcanic eruptions.

Field studies have also identified other features which are clearly associated with dike intrusions. Dike tip process zones where material in the vicinity of the intrusion appears damaged or altered are common and may extend up to tens of metres from the dike. Specific features commonly found within these process zones are deformation bands (Weinberger et al. 1995; Weinberger et al. 2000), dike parallel joints (Delaney et al. 1986), host rock breccias (Delaney and Pollard 1981) and mineralised fractures (Rogers

and Bird 1987). Understanding how the propagation of future dikes might be affected by the presence of these damage zones is also important in predicting volcanic eruptions.

Analytical and Numerical Studies

The most common approach to modeling dike propagation is to use the linear elastic fracture model (LEFM) where the dike is modeled as a fluid filled crack within a linear elastic medium. In the original application of fracture mechanics to dike propagation (Pollard 1987; Rudnicki 1980), if the stress intensity at the crack tip, K, equals or exceeds the fracture toughness of the host rock, K_c, the dike propagates. K is dependent only on the pressure difference between the fluid in the crack and the host medium, ΔP, and the length of the crack, l, as shown in Eq.1

$$K = \Delta P \sqrt{l} \tag{1}$$

In the Barenblatt modification (Barenblatt 1962) to LEFM, a tensile stress acts within a cohesive zone ahead of the crack tip to close the crack. Propagation is now also dependent on the crack width and a deformed process zone would be expected ahead of the dike. The size of the process zone relative to the dike size is important for predicting expected propagation behavior (Rubin 1993). If the process zone is small, dike propagation essentially proceeds in an elastic fashion. Otherwise, inelastic effects become increasingly important and the LEFM breaks down.

Advanced applications of the basic analytical models to fractured media (Rivalta et al. 2005) show that as the fracture density in the host medium increases, the average crack

opening increases, leading to decreased effective fracture toughness. The damage rheology model (Lyakhovsky et al. 1997) applied to the study of Meriaux et al. (1999) modelled the degradation of material ahead of the crack tip as a function of strain resulting in a reduction in elastic coefficients and leading to off-plane inelastic deformation.

A detailed finite element study performed by Gudmundsson and Phillip (2006) characterized the local stresses arising in layered models above a pressured chamber. The model summarized the direction of the least principle stress and the resulting discussion assumed that the dike would propagate perpendicular to this. The study proposed that in order for the stress field along the entire pathway of the feeder dike to favor fracture propagation, a stress field homogenization is required which might be achieved though host rock alteration and deformation.

Whilst the analytical/numerical studies suggest that dike propagation could be damage controlled and are of help in predicting how rock properties might control propagation, they are necessarily static. It is not possible to feed back changes in mechanical properties, take into account the local changes in stress that would arise from the propagating dike or model the impact of fracture mechanics. Ideally, we would like to be able to model dike propagation within a realistic geological setting with model feedback allowing changes in mechanical properties and localised stress fields over time. Through such a model we could assess local and far field damage due to the intrusion, understand the difference in intrusion mechanisms between different lithologies and how dikes behave as they approach the boundary between two mechanically different layers and

predict the effect of regional stress regimes on intrusion behaviour. We propose that the use of a particle or distinct element code where a collection of discrete bodies with simple inter-contact relationships undergo finite displacements and rotations may provide a way to do this. Complex system behavior is not prescribed in these models but emerges spontaneously from simple contact laws (Cundall 2001; Hobbs et al. 2004).

PFC^{2D}

We used the particle code model, PFC^{2D} (ITASCA 2004) in this study to create a synthetic rock whose mechanical behaviour is modelled using a collection of circular rigid particles bound together with bonds of finite normal and shear stiffness. The inter-particle interactions are modelled using a linear elastic model, a frictional sliding model and a bond model which act in parallel. An explicit time-stepping scheme is used where, at each step, Newton's second law is applied to each particle to provide updated velocities and positions from an initial set of contact forces. The resulting "rock" displays elastic behavior under low stress but may also "fracture" and exhibit brittle behavior if the inter-particle bonds break. The discrete particles do not have to represent real particles in order for the micro and macro behaviors to be reproduced. The code has been used successfully to model soil behaviors and rock deformation (Christiansson 2004; Gotteland 2004; Hunt et al. 2003; Zhao et al. in press; Zhao et al. 2007) including the emergence of shear bands in granular materials (Ord et al. in press).

The bulk properties are not assigned as in more commonly used continuum models but derive from the grain and cement micro-properties. By calibrating small scale synthetic models to laboratory tests such as biaxial strength tests, it is possible to develop a large

scale synthetic rock model with the elastic and brittle properties of a real rock (Potyondy and Cundall 2004).

The bonded particles in these models are representative of two distinct lithologies, the mechanically strong Lac du Bonnet granite (Potyondy and Cundall 2004) and the fairly unconsolidated, mechanically weak Gosford sandstone (Ord et al. in press). Potyondy and Cundall (2004) estimate the Young's modulus for the Lac du Bonnet granite to be 69GPa and Poisson ratio as 0.26. The Gosford sandstone parameters are estimated to be 6GPa and 0.25. A Poisson's ratio of 0.25 describes most rocks within the Earth's crust (Bell 2000). Laboratory estimates of Young's modulus for volcanic rocks can range from as little as 0.1GPa for volcanic tuffs to ~110GPa for basalts. Clearly the two rock types used in this model represent rocks with distinctly different strengths but both fall within the expected range in strength and Poisson's ratio for volcanic settings.

Methods

The models were built using the workflow detailed in Potyondy and Cundall (2004) and summarised in Figure 5.1 which produces a parallel bonded collection of particles under isotropic stress. A compact collection of particles were first created where the particle diameters have a uniform distribution between D_{max} and D_{min}. The particles were placed randomly at half their final size so that no two particles overlapped (**A**). The particles were then expanded to their final sizes (**B**) and the system allowed to rearrange under zero friction (**C**). An isotropic stress state was installed through an iterative approach where boundary particles were moved, freeing interior particles. This allowed static

equilibrium conditions to develop. The stress field was measured by averaging the stresses within the particle collection. Iterations continued until the stress increment (the difference between the target stress and the calculated stress) was within 5% of the target stress. Particle and intra-grain cement properties (Table 5.1) were chosen to reproduce the macro-properties of the two rock types, the mechanically strong Lac Du Bonnet Granite and the mechanically weak Gosford Sandstone.

A lithostatic stress state was applied in a similar manner to the isotropic case by moving boundary particles again until the difference between target stress and current stress on each of the boundary walls was within tolerance (±5%). The starting models were shallow layered models of dimension 500 (width) by 100m (height) with a top depth of 100m under lithostatic stress. The stress distribution in the final model can be seen in Figure 5.2. Two further sets of models with extensional and compressive stress regimes were created with an average difference from lithostatic of -2/+2GPa respectively. The boundary conditions applied to the models are illustrated in Figure 5.3. Four or eight overlapping boundary walls were placed around the model. The base wall was immobile. All other walls moved to maintain the initial stress since we expect that at a distance of~250m away from the dike entry point, the excess stress and strain associated with the dike have been dissipated and the pressure at the walls should therefore approximate lithostatic. The model lateral extent was chosen to minimise boundary effects on the intrusions.

Dike intrusion was modelled using an incoming particle stream at the base of the model. The particle properties are summarised in Table 5.1. In reality, the driving force for dike

propagation will be due to buoyancy, and perhaps volatile exsolution at the tip, but the aim here is to investigate how the stresses and damage associated with an intrusion into a particular lithology affect future propagation. The velocity of the incoming particles (60m/s) was chosen as a result of a sensitivity study on what velocity would cause cracking of the base layer. Thermal effects such as intrusion solidification or thermal alteration of the host rock are not modelled.

The ultimate effect of the incoming particle stream was the breaking of the inter-particle bonds in the synthetic rock model. Figure 5.4 illustrates how the model tracks the bond failure over time. Inter-particle bonds which suffer a shear failure are notated with a pink line, those with a normal failure by a light blue line. Tracking the mode and extent of bond breakages throughout the model over time is useful for interpretation of the model results with respect to field observations

Results

The simplest case investigated involved examining first the differences in propagation mechanism within two different media: the relatively weak Gosford sandstone (Figure 5.5) and the mechanically stronger Lac du Bonnet granite (Figure 5.6). In the sandstone model shown in Figure 5.5, at timestep 32568, (A), localized microfracturing occurs ahead of the intrusion entry point, extending vertically to the top of the model (100m) and with a lateral extent of ~68m either side of the intrusion entry point. Compared to the fractured area, the areal extent of invasion is much smaller with an intrusion width of 7m and a height of 11m. By timestep 42568, (B), further vertical propagation of the intrusion

to a height of 17m is accompanied by more distal microfracturing. Most of the microfracturing occurs within 118m of the intrusion entry point but isolated areas can be found throughout the model. Some of these may be as a result of boundary conditions. At timestep 92568 (C) most of the model is fractured, the intrusion still shows some vertical progression (27m) but the main intrusion width has doubled (15m) compared to timestep 42568 and there is also a wide sill like base of 48m to the intrusion. The extensive compression front ahead of the propagating dike at timestep 32568 shown in Figure 5.7 illustrates how the intrusion is able to generate distal microfractures. The width of the lines is proportional to the compressive stresses with a maximum stress of 170 MPa. When the stress exceeds inter-particle bond strength, extensive microfracturing occurs which weakens the formation, leaving no clear propagation direction and resulting in dissipative dike growth. Figure 5.8, which shows the total bond strain energy for the model over time, explains this further. There is an initial small build up of strain in the model but this is quickly released through microfracturing. Once the inter-particle bonds are broken, there is no means to build up strain again as the particle collection easily deforms and the bond strain energy remains low and constant.

Figure 5.6 illustrates an intrusion at timestep 123028 into the mechanically strong Lac du Bonnet Granite. Unlike the sandstone model, no real intrusion is observed until a crack propagates across the entire layer followed by magma invasion, with no microfracturing observed. Prior to intrusion a sill forms under the granite layer of length 61m at timestep 123028. The resulting intrusion has a width of 14m and a height of ~41m, which is similar to the layer thickness. Parallel dike joint faulting is observed at a distance of

105m from the intrusion entry point. Figure 5.9 shows the bond strain energy over time for granite layers of varying thickness, and illustrates that there is a build-up of critical strain before a crack propagates across the entire granite layer followed by magma invasion. The magnitude of the critical strain and the time to failure is a function of the layer thickness where the greater the layer thickness, the greater the critical strain and the longer the time to failure. The termination of the dike at the sandstone/granite boundary and the microfracturing in the overlying sandstone layer is explored in more detail in the next section

Layered models

We now proceed to describe the intrusion patterns which arise within layered models under lithostatic stress. The models are composed of four alternating layers where the base layer is sandstone or granite and each layer is 25m thick. The boundary conditions are set so that the average stress for each layer is maintained at lithostatic. Figure 5.10 shows the stress concentration for a layered model under lithostatic stress prior to invasion. The stresses are concentrated in the stiffer layers as was observed in the numerical models of Gudmundsson and Brenner (2005) and Gudmundsson and Phillip (2006).

In Figure 5.11, intrusion into a layered model with a sandstone base is shown at timestep 1173306. The extensive microfracturing of the base layer leaves no clear propagation direction and so several spurs develop from the central intrusion which has a height of only 44m. Rather than intrusion growth towards the surface, there is considerable lateral growth and the intrusion width is ~ 159m. Parallel cracks form in the overlying granite at

distances of ~76 and ~47m from the central crack which is approximately above the intrusion entry point. These could be used by the dike for invasion if the intrusion reached them. However, lateral growth and overlying layer doming is preferred over vertical propagation of the intrusion. This model shows some problems with boundary conditions for the upper granite layer, which presumably would deform in a similar manner to the other layers if it was not constrained to maintain contact with the upper wall. Instead of doming, the upper granite layer peels away from the lower sandstone.

Figure 5.12 illustrates the intrusion pattern at timestep 1177789 for invasion into a layered model with a granite base under lithostatic stress. A sill of length 82m forms to the right of the propagating crack which must form across the entire granite layer before intrusion occurs. After magma invasion using the newly formed crack, the majority of the intrusion growth is initially due to expansion within the crack and the intrusion has a width of 76m. However, the intrusion does eventually reach the overlying sandstone layer. The sandstone layer shows extensive microfracturing before the intrusion arrives which causes the propagation path within the sandstone layer to be ill defined and spurs develop off the main intrusion with a width of 37m. The total intrusion height is 88m with the basal part of the intrusion reaching a height of 47m. Distinct cracks also appear in the upper granite before magma invasion at distance of 78 and 138 meters from the intrusion entry point. These show characteristics of brecciation where the crack within the granite is filled with sandstone material from the overlying layer.

Impact of regional stress regimes on intrusion

In order to examine the impacts of regional stress regimes, we modelled dike intrusion patterns by changing the model regional stress regimes according to Figures 5.13-5.16. Addressing first the 4 layer model with a sandstone base, in Figure 5.13 we see that at early time (timestep of 123306 for lithostatic and compressive case, 119906 for extensional) there is little difference in initial propagation style between the different stress regimes. The intrusion dimensions vary from widths of 17m for the lithostatic case to 22m for the compressive and 24m for the extensional case. The intrusion heights range from 13m for the lithostatic case to 16m for the compressive and extensional cases. The intrusion causes extensive microfracturing over the whole sandstone layer resulting in an intrusion which favours lateral growth over vertical propagation. In Figure 5.14, the models under all stress regimes show doming at late time (timestep of 1173306 for lithostatic and compressive case, 1169906 for extensional). The lithostatic and compressive cases have invasion limited to the lower sandstone layer although microfracturing has occurred in the upper sandstone layer and a set of parallel cracks have formed across the overlying granite layer at distances of ~76 and 47m from a central crack located above the intrusion entry point . The compressive regime has an intrusion with two distinct spurs coming off the main intrusion with widths of 40m and 20m. The maximum intrusion height is 41m for the compressive regime compared to 44m for the lithostatic case. In contrast, the extensional regime encourages propagation into the overlying granite layer. The main intrusion has a width of 147 m but once the intrusion invades the overlying granite layer using an early formed dike joint for invasion, the

intrusion width is only 39m. Two cracks form in the first granite layer, the central crack used for invasion and a parallel crack at a distance of 110m from the central one. An additional crack forms in the upper granite layer which presumably could be used for invasion at a later point.

Figure 5.15 and Figure 5.16 show intrusion for the same three stress regimes into a similar model where the base is granite. At early time (timestep of 127789 for lithostatic and extensional case, 126889 for compressive) shown in Figure 5.15, there is again little difference in initial propagation style. A crack forms across the entire base granite layer before magma invasion, and intrusion growth occurs through expansion of the crack. The intrusion's width is similar in the lithostatic, compressive and extensional cases (11,13and 11m respectively). A sill forms prior to the crack propagation and has similar dimensions also in the lithostatic and compressive regimes (43m and 46m respectively). However, the extensional regime has a much smaller sill length of 36m. The intrusion heights are 22m, 17m and 26m respectively. A crack forms parallel to the intrusion crack in the base layer for all regimes. At late time (timestep of 1177789 for lithostatic and extensional case, 1176889 for compressive), shown in Figure 5.16, both the compressive and extensive regimes have retarded dike propagation compared to the lithostatic case with maximum intrusion heights of 78m for the compressive case and 65m for the extensional case compared with 88m for the lithostatic case. In the compressive case retardation results from a preference for dissipated growth in the sandstone layer with doming of overlying layers so that the intrusion does not reach the second granite layer. This is reflected in the intrusion geometry. The compressive case shows a blocky

intrusion with a width of 78m and height of 58m entirely within the sandstone layer despite the initial layer thickness being only 25m. In contrast, the lithostatic case has a base intrusion width of 76m which narrows to 37m as the intrusion enters the overlying granite layer. The height of the basal intrusion is 47 m with a total intrusion height of 88m. In the extensive case, two main spurs develop during the invasion into the overlying sandstone layer, which fill in creating a basal intrusion of width 118m and height of 46 m. A 3rd spur develops towards the top resulting in a maximum intrusion height of 65m.

Dike joints are apparent in all three cases. In the compressive regime, a dike joint occurs in the lower granite layer at a distance of 131m from the intrusion entry point and in the upper layer at distances of 68m and 205m. In the lithostatic regime, a dike joint in the lower granite layer occurs at a distance of 135 m and in the upper granite layer at distances of 78 and 138m. In the extensional regime, a dike joint in the lower granite layer occurs at a distance of 149 m and in the upper granite layer at a distance of 126m. The crack in the overlying granite layer keeps opening in the extensional case but dissipative growth in the sandstone layer is preferred and the dike keeps expanding rather than progressing vertically.

Discussion

This study is a test of the suitability of the particle code model approach to modelling dike intrusions and in general the model results generally fit well with field observations. They suggest that propagation to the surface is a rare event regardless of the formation which the dike is intruded into. None of the models allowed propagation to develop

further than ~65m from the intrusion entry point preferring lateral growth and doming in preference to further propagation. All the models show extensive parallel dike jointing in the mechanically strong granite layer and damage zones ahead of the dike in the weaker sandstone layers. Field observations also suggest that many more dikes are intruded into stratavolcanoes than reach the surface. In contrast to the models of Gudmundsson and Brenner (2005) and Gudmundsson and Phillip (2006), which concentrated solely on localisation of stresses but also predicted that surface propagation would be rare, these models also exhibit many of the characteristics of dike process zones. This suggests that particle code modelling holds promise as a new way to examine dike processes.

Gudmundsson and Brenner (2005) and Gudmundsson and Phillip (2006) proposed that dike termination at boundaries was primarily due to stress barriers related to abrupt changes in stiffness. The models in this study concur that changes in stiffness can control dike termination but they also illuminate why stiffness may be a controlling factor beyond simply acting to concentrate stresses. The stiffness of the model materials differed by an order of magnitude (69 GPa vs. 6GPa) and they exhibited clear differences in intrusion behaviour.

For intrusion into granite, the layer thickness is critical as a clean crack across the layer is required for propagation. In Figure 5.9 which shows the bond strain energy over time for intrusion into granite layers of varying thickness, a crack forms across the entire layer when the strain drops abruptly. For a thicker layer, a longer time is required to build up sufficient strain within the layer for failure. For instance, a layer of thickness 5m cracked at timestep 23890 with maximum bond strain energy of 73MPa. In contrast a 50m layer

required a critical strain of 730MPa and failed at timestep 127430. Over the timescales investigated in these models, no crack formed for a layer 100m thick. Intrusions into granite may be assisted by the prior creation of dike joints which can be used for invasion providing an easy pathway for propagation without build-up of strain across the layer. Intrusion into sandstone is primarily through the generation of extensive microfractures which weaken the formation and promote dissipative growth. Conversely an intrusion which originates in a weak layer may be unable to build sufficient strain with the granite layer to cause cracking, preferring to grow through dissipative growth in the micro fractured weak layer. The model contrasts in stiffness are representative of the contrasts in stiffness that might be expected at a stratavolcano. In other volcanic settings, however, we might expect the contrast to be less and therefore the differences in behaviour here is likely to be more pronounced that would be expected in other settings.

It may not be just the contrast in stiffness between the layers that is important but also the overall stress regime. Models with the same contrasts in stiffness showed different behaviours under different stress regimes. Surprisingly both extensive and compressive regimes retard dike propagation relative to the lithostatic case (granite base) with a compressive regime favoring surface deformation and an extensional regime favoring growth through crack expansion.

Fracture toughness

Fracture toughness estimated from dike dimensions is several orders of magnitude higher than that seen in small scale tests (Ryan 1994) and appears to depend on the length scale of the crack and the crack tip process zone (Rubin 1995). These models suggest that for

mechanically strong layers, dike propagation does not proceed by incremental small cracks but though cracking across an entire layer which would require that the stress intensity be much higher and therefore the estimated fracture toughness would be higher too. A better measure of the "toughness" of the layer would be the fracture energy as suggested by Rubin (1995) since this would take into account the size of the crack.

Current model limitations

This study also revealed some limitations to using a particle code to model intrusions, many of which could be improved upon in future studies. The main issue is that we were unable to relate the speed of the incoming particles (60m/s) to an intrusion ascent rate. It may be possible however to use the momentum of the balls as a proxy to the fracture energy. Secondly, although the scale of the models themselves appears suitable with some minor adjustments in boundary conditions, the scale of the evolved dikes are on the order of 10s of metres which is an order of magnitude larger than those observed in the field. The chosen particle size and total model dimensions determine the total number of particles used in the model. Since the momentum and position of each particle is tracked and recalculated at each timestep, the number of particles in the model determines the run times. Decreasing the particle radius increases the number of particles in the model for given model dimensions. The particle radius of ~1m which resulted in 7550 original particles was chosen in order to keep model run times reasonable (<48hours) in the large scale models whilst still using a large enough model that boundary effects were minimised. Future models should be tested with much smaller particles. This may require

a parallel version of the code to be run on a supercomputer in order to still allow investigation of dike modelling in a reasonable amount of time.

Finally, the Gosford sandstone model is unconsolidated and therefore very weak. The availability of a small scale model calibrated to laboratory stress tests determined its use in this study as a weak layer. However the behaviour may be extreme compared to the expected behaviour in weak layers that might be found in volcanic settings. Future studies should incorporate weak layers which are calibrated to a stronger sandstone or volcanic tuff small scale model.

Conclusions

PFC^{2D} has proved to be a useful tool for exploring dike mechanisms. The model results show observed field relations such as extensive microfracturing across the weaker sandstone layers and parallel dike jointing at distances of 10's of meters in the stronger granite layers. Intrusion in the weak sandstone layers proceeds through dissipative growth after extensive microfracturing generating intrusions with widths of 10's of meters. Intrusion into granite proceeds by the buildup of a critical strain within the granite layer leading to a crack propagating across the layer followed by magma invasion. Typically the intrusions widths are somewhat less than in the sandstone. Compressional and extensional regimes both act to retard intrusion growth towards the surface. In the compressive regime, doming of overlying layers is preferred over dike propagation. In the extensional regime, lateral growth is preferred over propagation. A scaled dependence to fracture toughness is also observed to emerge from the modeling.

Although the scale of the intrusions are an order of magnitude greater than field observations, this study suggests that the particle code method with some modifications can provide insights into the complex mechanism of dike intrusion at shallow depths which cannot be obtained though the current analytical or continuum models.

Future studies should work on relating the momentum of the incoming particles to the fracture energy of a dike and ensure that the scale of the dikes more closely approximates that observed in the field.

Acknowledgements

This project was made possible through a CSIRO internship to J Mongrain.

References

Bagdassarov N, Dorfman A, Dingwell DB (2000) Effect of alkalis, phosphorus, and water on the surface tension of haplogranite melt. Am Mineral 85(1):33-40

Barenblatt GI (1962) The mathematical theory of equilibrium cracks in brittle fracture. Advanced applied mechanics 7:55-129

Bell FG (2000) Engineering properties of soils and rocks. Blackwell, Oxford

Burgisser A, Gardner JE (2004) Experimental constraints on degassing and permeability in volcanic conduit flow. Bull Volcanol 67(1):42-56

Carroll MR, Blank JG (1997) The solubility of H_2O in phonolitic melts. Am Mineral 82:549-556

Christiansson R (2004) Numerical simulation of the mechanical behavior of discontinuous rock masses. In: Numerical Modeling in Micromechanics via Particle Methods - 2004. Routledge, pp 85 - 92

Cioni R (2000) Volatile content and degassing processes in the AD 79 magma chamber at Vesuvius (Italy). Contributions to Mineralogy and Petrology 140(1):40-54

Cioni R, Civetta L, Marianelli P, Metrich N, Santacroce R, Sbrana A (1995) Compositional layering and syn-eruptive mixing of a periodically refilled shallow magma chamber: the AD 79 plinian eruption of Vesuvius. J Petrol 36(3):739-776

Cox RG (1969) The deformation of a drop in a general time- dependent fluid flow. Journal of Fluid Mechanics 37:601-623

Cundall PA (2001) A discontinuous future for numerical modelling in geomechanics ? Proceedings of the Institution of Civil Engineers, Geotechnical Engineering 149:41-47

Delaney JS, Pollard DD (1981) Mechanics of growth of some lacolithic intrusions in the Henry mountains, Utah, I: field observations, Gilbert's model, physical properties and flow of the magma. Tectonophysics 18:261-309

Delaney PT, Pollard DD, Ziony JI, McKee EH (1986) Field relations between dikes and joints: Emplacement processes and paleostress analysis. J Geophys Res 91:4920-4938

Foulger GR, Toomey DR (1989) Structure and evolution of the Hengill-Grensdalur volcanic complex, Iceland: Geology, geophysics, and seismic tomography. J Geophys Res 94(B12)

Gardner JE, Hilton M, Carroll MR (1999) Experimental constraints on degassing of magma; isothermal bubble growth during continuous decompression from high pressure. Earth Planet Sci Lett 168(1-2):201-218

Gardner JE, Hilton M, Carroll MR (2000) Bubble growth in highly viscous silicate melts during continuous decompression from high pressure. Geochim Cosmochim Acta 64(8):1473-1483

Gardner JE, Thomas RME, Jaupart C, Tait S (1996) Fragmentation of magma during Plinian volcanic eruptions. Bull Volcanol 58(2):144-162

Gotteland P (2004) DEM modeling of soil geocomposite material for rockfall impact. In: Numerical Modeling in Micromechanics via Particle Methods - 2004. Routledge, pp 13 - 20

Gudmundsson A (1995) Infrastructure and mechanics of volcanic systems in Iceland. An Rev Earth Planet Sci 28(107-140)

Gudmundsson A (2002) Emplacement and arrest of sheets and dykes in central volcanoes. J Volcanol Geotherm Res 116:279-298

Gudmundsson A, Brenner SL (2005) On the conditions of sheet injections and eruptions in stratovolcanoes. Bull Volcanol 67:768-782

Gudmundsson A, Phillip SL (2006) How local stress fields prevent volcanic eruptions. J Volcanol Geotherm Res 158:257-268

Gurioli L, Houghton BF, Cashman KV, Cioni R (2005) Complex changes in eruption dynamics during the 79 AD eruption of Vesuvius. Bull Volcanol 67(2):144-159

Hobbs B, E, Ord A, Regenauer-Lieb K, Boschetti F, Zhang Y, Durrlemann S (2004) Ab initio emergent phenomena in PFC. In: Shimizu Y, Hart R, Cundall PA (eds) Numerical modeling in Mocromechanics via Particle Methods. Balkema, Leiden, pp 235-239

Hui H, Zhang Y (2006) Toward a general viscosity equation for natural anhydrous and hydrous silicate melts. Geochim Cosmochim Acta 2007(71):403-416

Hunt SP, Meyers AG, Louchnikov V (2003) Modelling the Kaiser effect and deformation rate analysis in sandstone using the discrete element method. Computers and Geotechnics 30(7):611-621

Iacono Marziano G, Schmidt BC, Dolfi D (2007) Equilibrium and disequilibrium degassing of a phonolitic melt (Vesuvius AD 79 "white pumice") simulated by decompression experiments. J Volcanol Geotherm Res 161(3):151-164

ITASCA (2004) PFC2D Particle Flow Code in 2 Dimensions. Users Guide. Minnesota, USA

Ito T, Yoshioka S (2002) A dike intrusion model in and around Miyakejima, Niijima and Kozushima in 2000. Tectonophysics 359:171-187

King PL, Larsen JF, Lui DK, Lockard J, Dalby KD, Griffin T (2006) Rapid Analysis of total H_20 and molecular H_2O contents of small geologic glasses using reflectance IR spectroscopy. Geol. Assoc. Canada-Mineral. Assoc. Canada Abstract 649

Larsen JF (2006) Experimental study of bubble nucleation in K-phonolite melt. In: AGU. San Francisco

Larsen JF, Gardner JE (2000) Experimental constraints on bubble interactions in rhyolite melts; implications for vesicle size distributions. Earth Planet Sci Lett 180(1-2):201-214

Larsen JF, Gardner JE (2004) Experimental study of water degassing from phonolite melts: implications for volatile oversaturation during magmatic ascent. J Volcanol Geotherm Res 134:109-124

Lees JM (1992) The Magma System of Mount St. Helens: Nonlinear High Resolution P-Wave Tomography. J Volcanol Geotherm Res 53:103-116

Lyakhovsky V, Ben-Zion Y, Agnon A (1997) Distributed damage, faulting and friction. J Geophys Res 102(B12):27635-27649

Lyakhovsky V, Hurwitz S, Navon O (1996) Bubble growth in rhyolitic melts-experimental and numerical investigation. Bull Volcanol 58(1):19-32

Macdonald GA (1972) Volcanoes. Prentice-Hall, New Jersey

Manga M, Stone HA (1994) Interactions between bubbles in magmas and lavas: effects of bubble deformation. J Volcanol Geotherm Res 63:267-279

Mangan MT, Sisson TW, Hankins WB (2004) Decompression experiments identify kinetic controls on explosive silicic eruptions. Geophys Res Lett 31:no.8, 4

Marinoni LB, Gudmundsson A (2000) Dykes, faults and palaeostresses in Teno and Anaga massifs of Tenerife (Canary Islands). J Volcanol Geotherm Res 103(83-103)

Massol H, Koyaguchi T (2005) The effect of magma flow on nucleation of gas bubbles in a volcanic conduit. J Volcanol Geotherm Res 143(3-4):69-88

Meriaux C, Lister JR, Lyakhovsky V, Agnon A (1999) Dyke propagation with distributed damage of the host rock. Earth Planet Sci Lett 165:177-185

Mourtada-Bonnefoi CC, Laporte D (2004) Kinetics of bubble nucleation in a rhyolitic melt; an experimental study of the effect of ascent rate. Earth Planet Sci Lett 218(3-4):521-537

Mueller S, Melnik O, Spieler O, Scheu B, Dingwell DB (2005) Permeability and deagssing of dome lavas undergoing rapid decompression:An experimental determination. Bull Volcanol 67:526-538

Ord A, Hobbs B, Regenauer-Lieb K (in press) Shear band emergence in granular materials- A numerical study. International journal for numerical and analytical methods in geomechanics

Patane D, Chiarabba C, Cocina O, De Gori P, Moretti M, Boshi E (2002) Tomographic images and 3D earthquake locations of serismic swarm preceeding the 2001 Mt Etna eruption: eruption for an dyke intrusion. Geophys Res Lett 29(10):135-138

Pollard DD (1987) Elementry fracture mechanics applied to the structural interpretation of dykes. Geological Association of Canada (34):5-24

Potyondy DO, Cundall PA (2004) A bonded particle model for rock. International journal of rock mechanics and mining sciences 41:1329-1364

Proussevitch AA, Sahagian DL (1996) Dynamics of coupled diffusive and decompressive bubble growth in magmatic systems. J Geophys Res 101:17447-17455

Proussevitch AA, Sahagian DL, Kutolin VA (1993) Stability of foams in silicate melts. J Volcanol Geotherm Res 59(1-2):161-178

Rivalta E, Bottinger M, Dahm T (2005) Buoyancy-driven fracture ascent: Experiments in layered gelatine. J Volcanol Geotherm Res 144:273-285

Rogers RD, Bird DK (1987) Fracture propagation associated with dike emplacement at the Skaergaard intrusion, East Greenland. Journal of Structural Geology 9:71-86

Rubin AM (1993) Tensile fracture of rock at high confining pressure:implications for dike propagation. J Geophys Res 98

Rubin AM (1995) Why geologists should avoid using "fracture" toughness (at least for dykes). In: Baer, Heiman (eds) Physics and Chemistry of Dykes. Balkema, Rotterdam, pp 53-64

Rudnicki JW (1980) Fracture mechanics applied to the earth's crust. An Rev Earth Planet Sci 8:489-525

Rust AC, Manga M, Cashman KV (2003) Determining flow type, shear rate and shear stress in magmas from bubble shapes and orientations. J Volcanol Geotherm Res 122(1-2):111-132

Ryan MP (1994) Magmatic Systems. Academic Press, San Diego

Saar MO, Manga M (1999) Permeability-porosity relationship in vesicular basalts. Geophys Res Lett 26(1):111-114

Sahimi M (1994) Applications of percolation theory. Taylor & Francis, p 258

Sherburn S, Bannister S, Bibby H (2003) Seismic velocity structure of the central Taupo Volcanic Zone, New Zealand, from local earthquake tomography. J Volcanol Geotherm Res 122(1-2):69-88

Sheridan MF, Barberi F, Rosi M, Santacrose R (1981) A model for Plinian eruptions of Vesuvius. Nature 289:282-285

Sparks RSJ (1978) The dynamics of bubble formation and growth in magmas; a review and analysis. J Volcanol Geotherm Res 3(1-2):1-37

Stefano RD, Chiarabba C (2002) Active source tomography at Mt. Vesuvius: Constraints for the magmatic system. J Geophys Res 107(b11)

Stewart MA, Klein EM, Karson JA, Brophy JG (2003) Geochemical relationships between dikes and lavas at the Hess Deep Rift: implications for magma eruptibility. J Geophys Res 108

Taylor GI (1932) The viscosity of a fluid containing small drops of another fluid. Proceedings of the Royal Society of London, A 138:41-48

Taylor GI (1934) The formation of emulsions in definable fields of flow. Proceedings of the Royal Society of London, A 146:501-523

Toramaru A (1995) Numerical study of nucleation and growth of bubbles in viscous magmas. Journal of Geophysical Research, B, Solid Earth and Planets 100(2):1913-1931

Weinberger R, Baer G, Shamir G, Agnon A (1995) Deformation bands associated with dyke propagation in porous sandstone, Makhtesh Ramon, Israel. In: Baer, Heiman (eds) Physics and Chemistry of Dykes. Balkema, Rotterdam, pp 95-112

Weinberger R, Lyakhovsky V, Baer G, Agnon A (2000) Damage Zones around en echelon dike segments in prous sandstone. J Geophys Res 105:3115-3133

Whittington A, Richet P, Linard Y, Holtz F (2001) The viscosity of hydrous phonolites and trachytes. Chem Geol 174:209-224

Williams H, McBirney AR (1979) Volcanology. Freeman, San Francisco

Wömer G, Schmincke H-U (1984) Petrogenesis of the zoned Laacher See tephra. Journal of Petrology 25:836-851

Woods AW, Koyaguchi T (1994) Transitions between explosive and effusive eruptions of silicic magmas. Nature 370(6491):641-644

Yi Y-B, Sastry AM (2004) Analytical approximation of the percolation threshold for overlapping ellipsoids of revolution. Proceedings of the Royal Society of London, A 460:2353-2380

Zhao C, Hobbs BE, Ord A, Peng S (In Press) Critical contact stiffness concept and simulation of crack generation in particle models of large length-scales. Computers and Geotechnics

Zhao C, Hobbs BE, Ord A, Robert PA, Hornby P, Peng S (2007) Phenomenological modelling of crack generation in brittle crustal rocks using the particle simulation method. Journal of Structural Geology 29(6):1034-1048

Table 5.1 Properties of particle and intra-grain "cement" in models.

	Grain Properties								Cement Properties			
	Ball Radius (m)	Dmax/Dmin	Density (kgm^{-3})	Porosity Vol. %	Friction	Young's Modulus (GPa)	Normal to shear strength ratio	Parallel Bond Radius (m)	Young's Modulus (GPa)	Normal strength (MPa/m)	Tensile strength (MPa/m)	Shear Strength (MPa/m)
Sandstone	1	1.7	2227	16	1.0	6	1.0	1	6	2	3.5	3.5
Granite	1	1.7	2630	16	0.5	62	2.5	1	62	23	160	160
Magma	1	1	2300	-	-	0.1	-	-	-	-	-	-

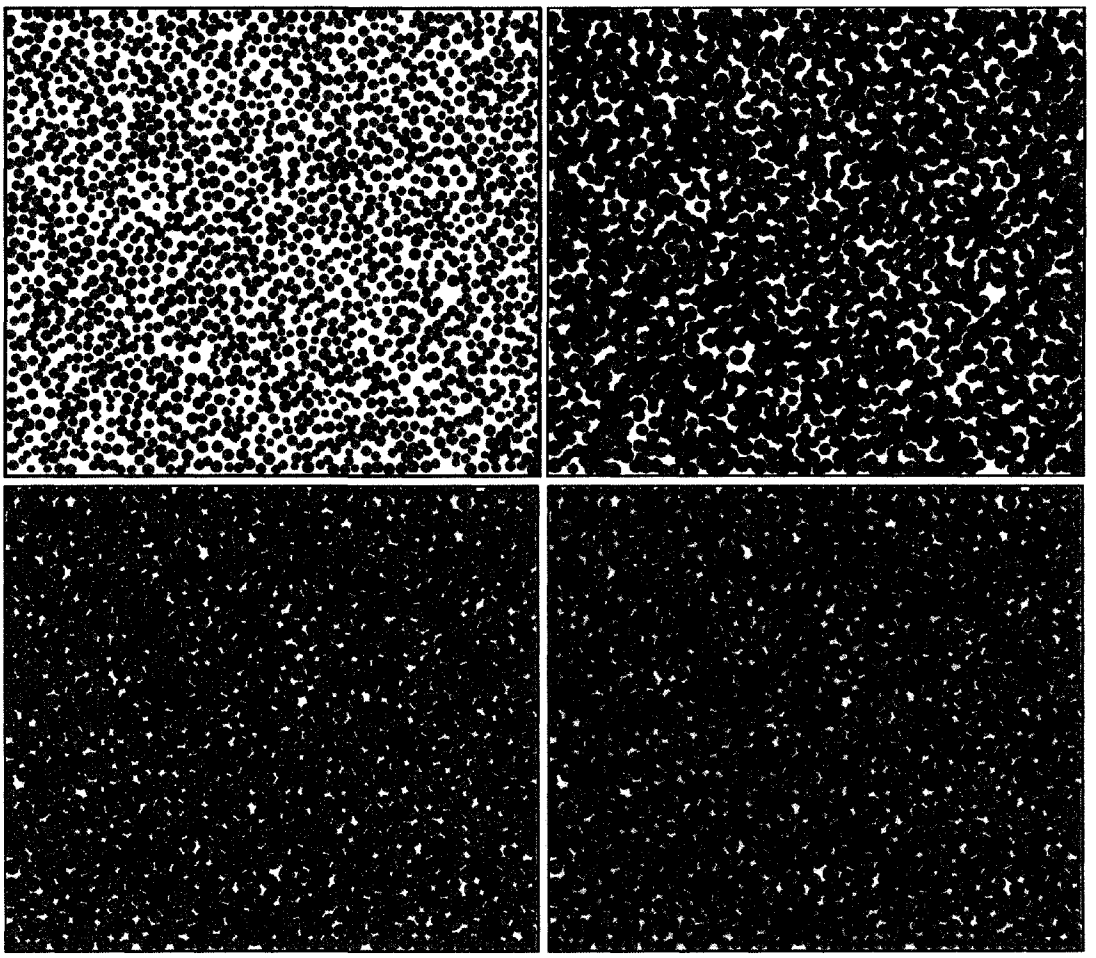

Figure 5.1 Synthetic rock genesis workflow for PFC^{2D} model.
(A) Particle Assembly for porosity less than finally required using reduced bail radius. (B) Particle Assembly at required porosity, achieved through ball expansion. (C)Particle Rearrangement (D) Contact Force Distribution after to achieve isotropic stress condition. Compressive forces are shown in pink where the thickness of the line is proportional to the magnitude.

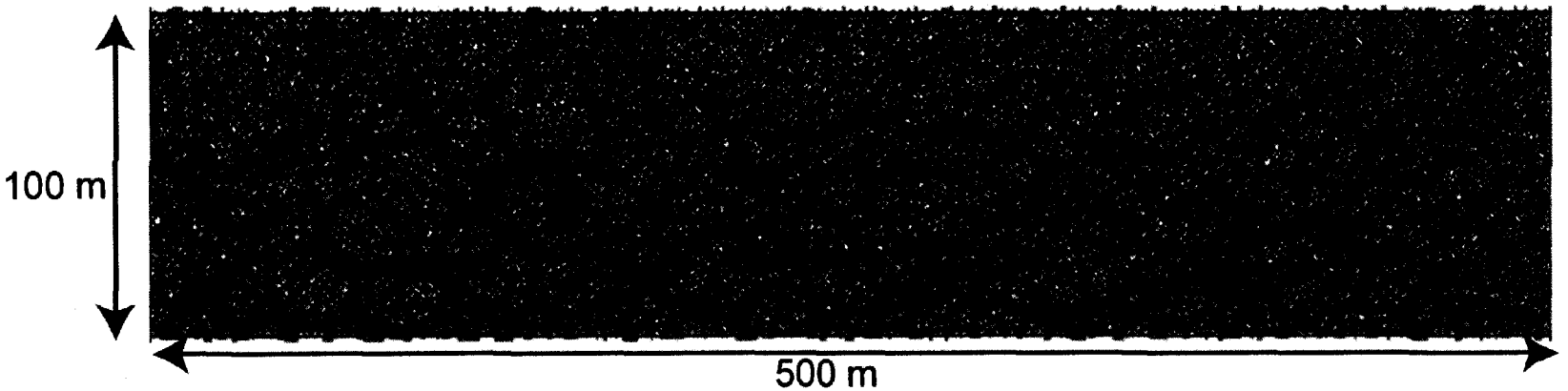

Figure 5.2. Compressive forces for model under lithostatic stress.
Model top depth is 100m. Pink line thickness is proportional to magnitude of compressive force

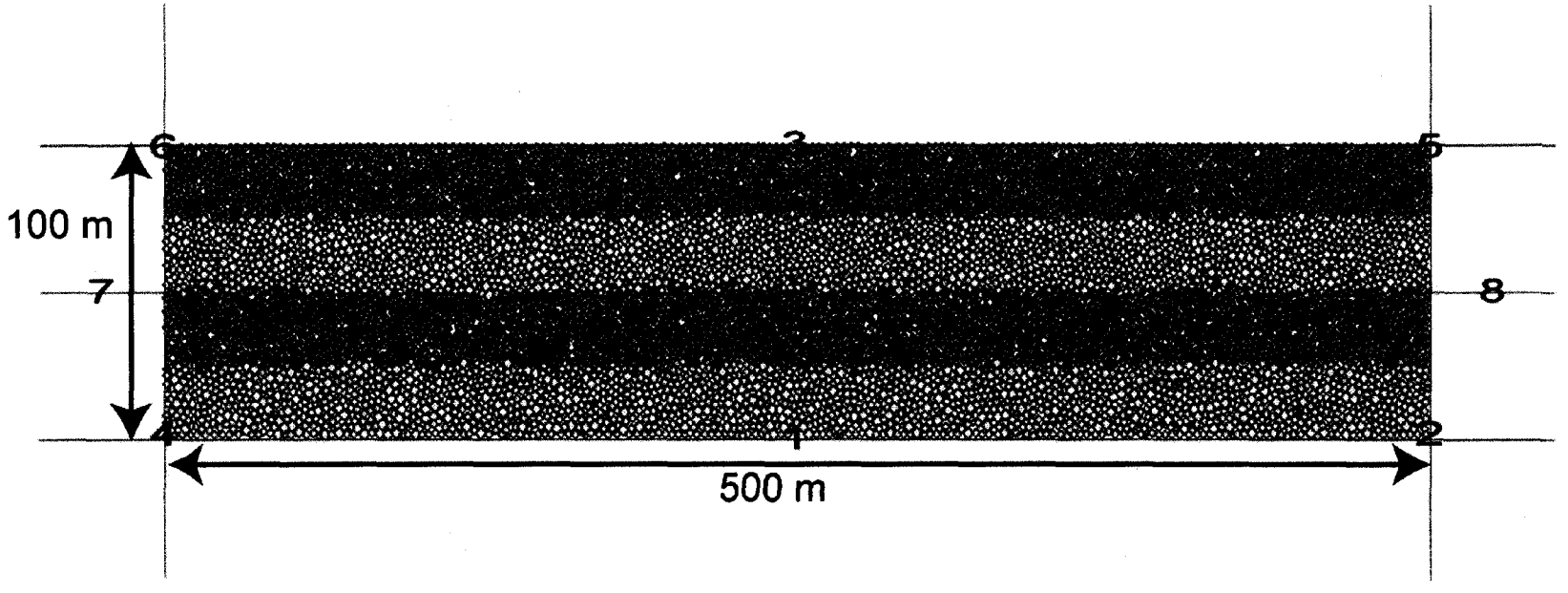

Figure 5.3 Model Overview.
Blue bonded particles represent granite. Yellow bonded particles represent sandstone. Eight numbered boundary walls which are all free to move to maintain required stress state except for base wall, #1.

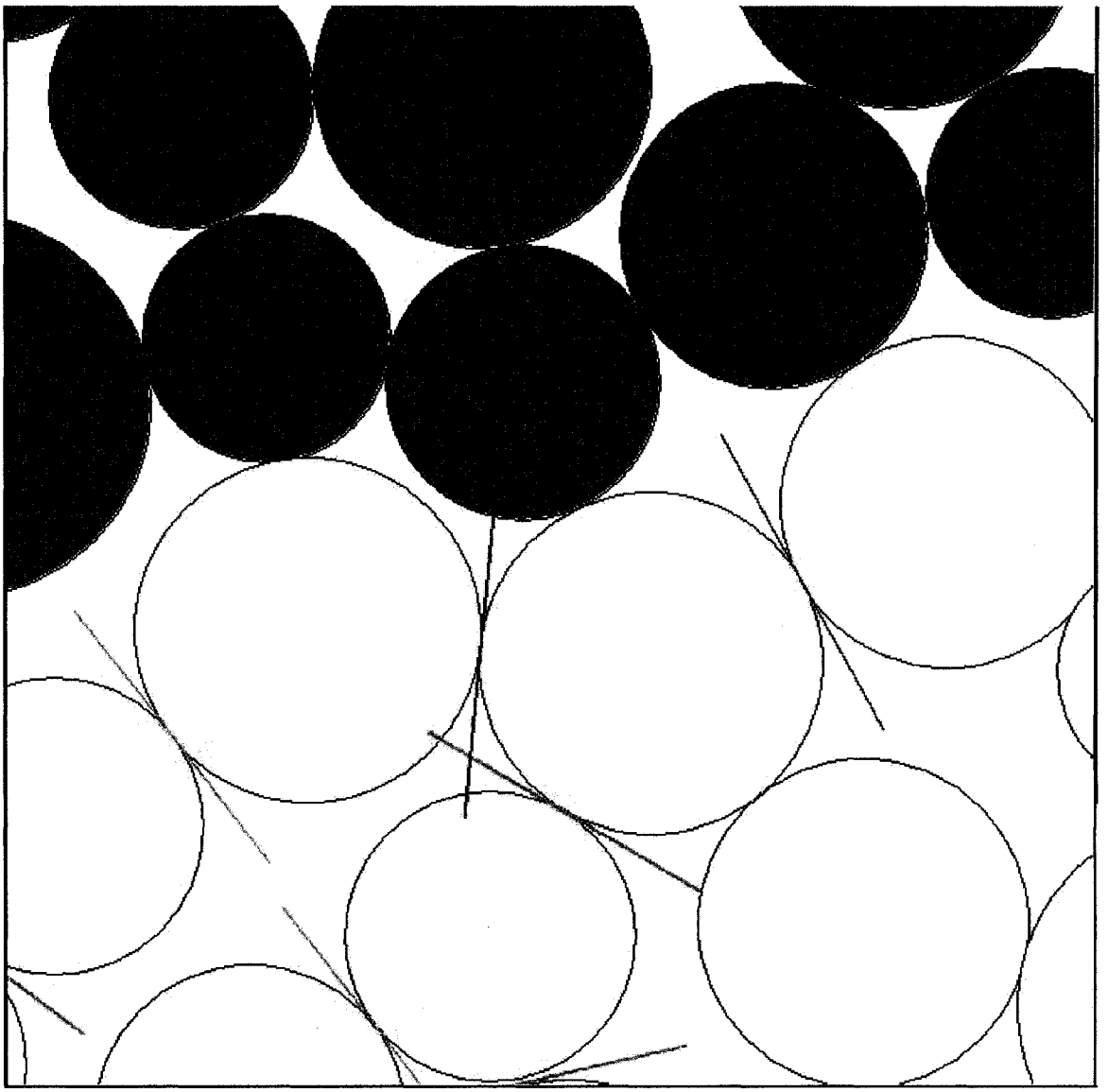

Figure 5.4 Illustration of inter-particle bond failure.
Blue particles represent granite. Yellow particles represent sandstone. Blue lines represent inter-particle bonds broken by normal failure. Pink lines represent inter-particle bonds broken by shear failure.

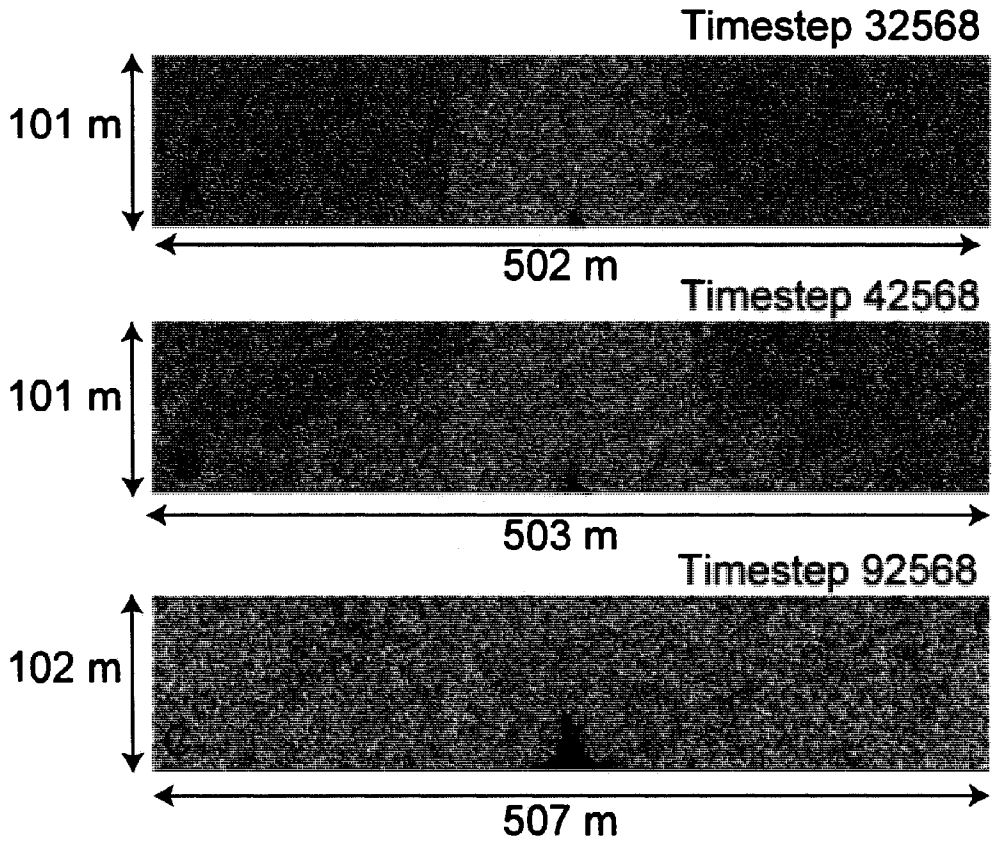

Figure 5.5 Intrusion into sandstone under lithostatic stress.
Yellow particles are sandstone, red particles represent magmatic intrusion. Biue lines are inter-particle bonds broken by normal failure. Pink lines are inter-particle bonds broken by shear failure. Extensive microfracturing initially ahead of intrusion but later across entire model. Later invasion is lateral and vertical as microfracturing leads to no clear propagation direction

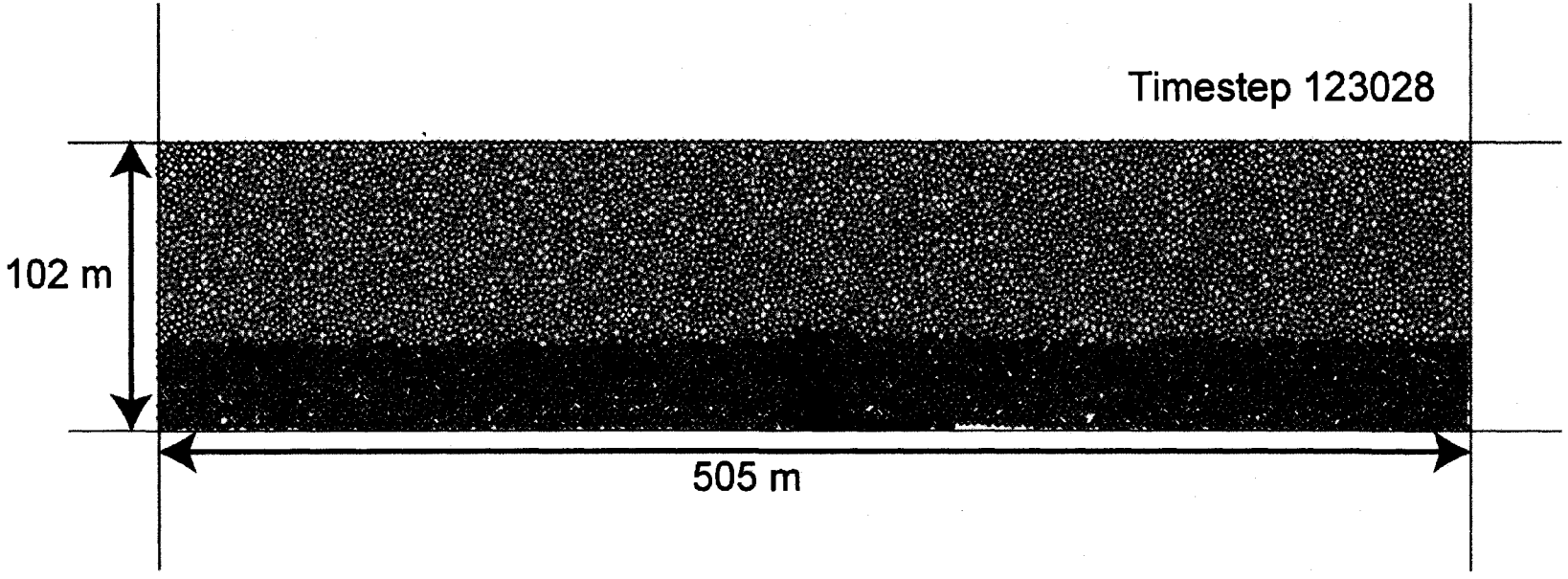

Figure 5.6 Intrusion into granite under lithostatic stress.
intrusion invades crack formed across granite layer. Microfracturing in upper sandstone but occurs without invasion of sandstone. Parailel dike jointing is visible in the granite iayer. Yellow particles are sandstone, blue particles represent granite, red particle represent magmatic intrusion. Blue lines are inter-particle bonds broken by normal failure. Pink lines are inter-particle bonds broken by shear failure. They represent micro-fracturing of the formation.

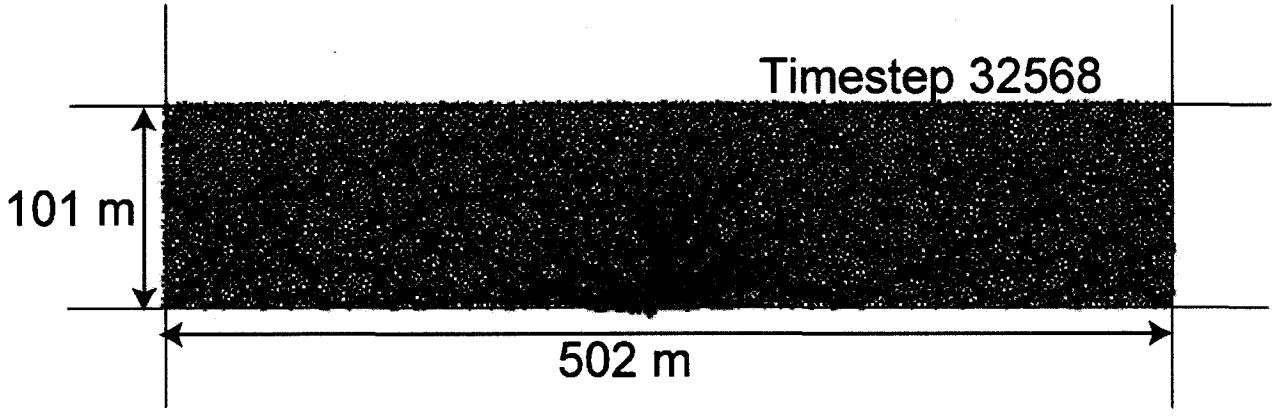

Figure 5.7 Compressive front ahead of intrusion into sandstone.
Yellow particles are sandstone. Pink lines are compressive stress with iine thickness proportional to the stress magnitude.

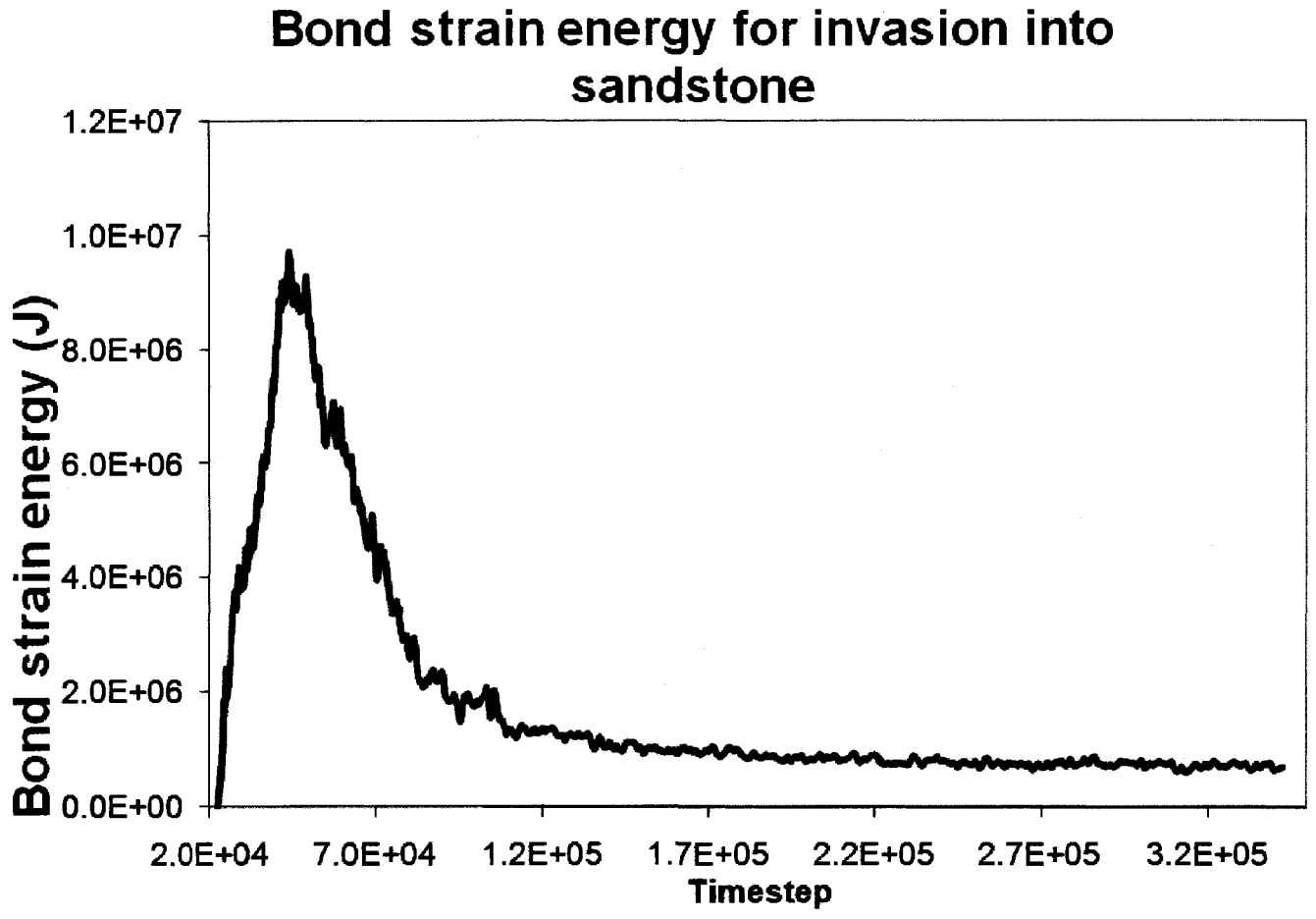

Figure 5.8 Bond strain energy for intrusion into sandstone under lithostatic stress.
Steep build up of stress is followed by gradual release of strain with no significant further buiidup observed

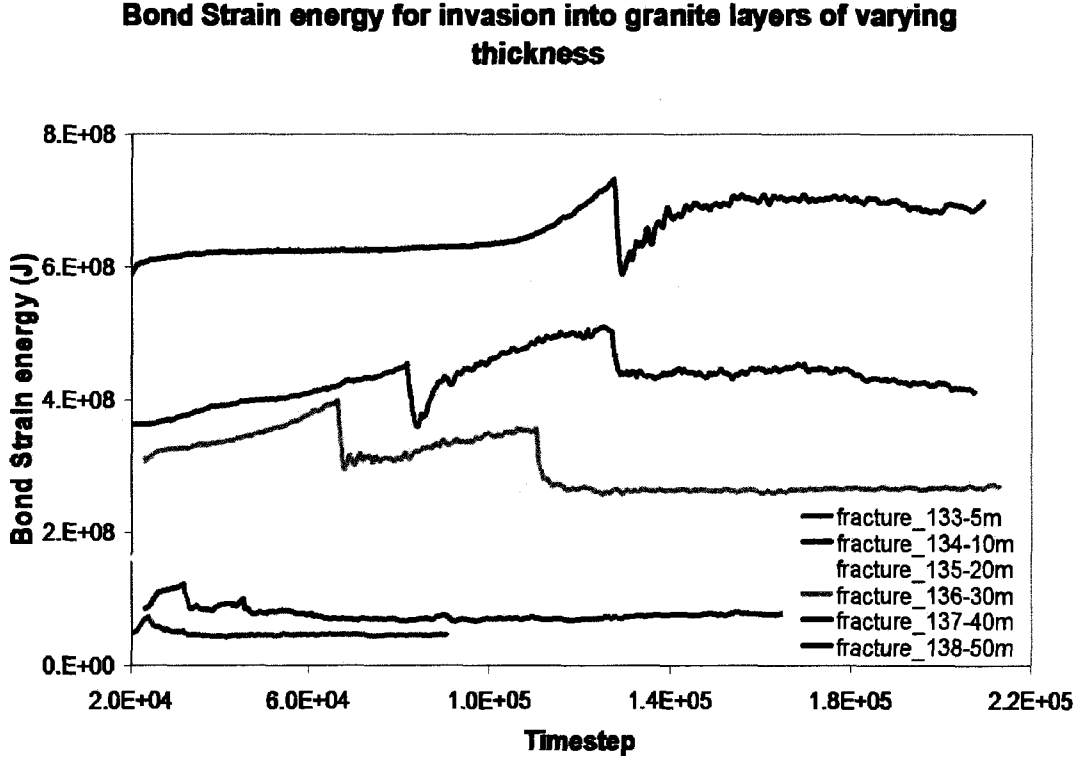

Figure 5.9 Bond strain energy for intrusion into granite layers of varying thickness.

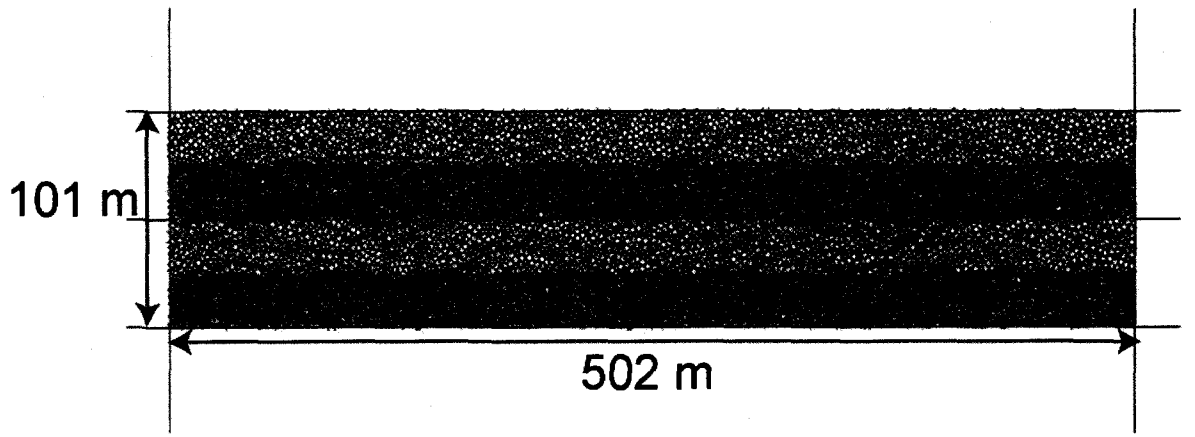

Figure 5.10. Stress concentration in stiff layers.
Compressive stresses are pink lines, electric blue lines are tension. Line thickness is proportional to stress. Yellow particles represent weak sandstone. Blue particles represent strong granite

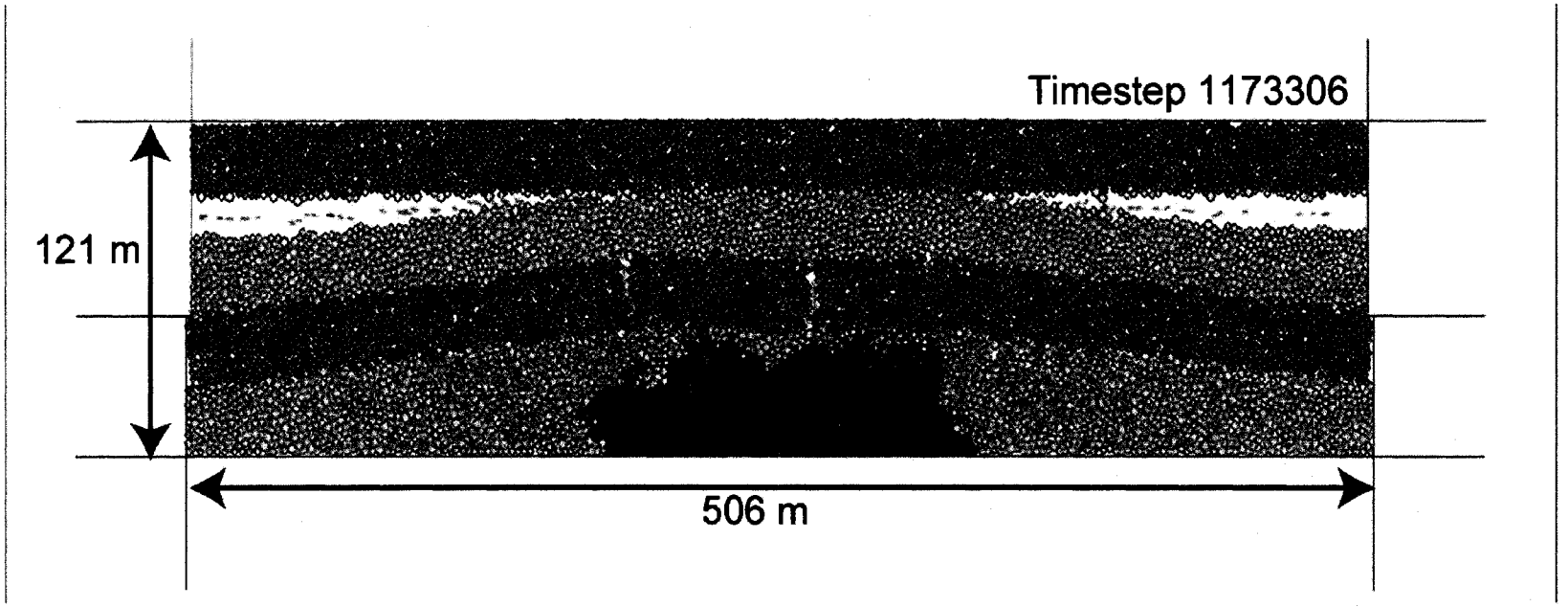

Figure 5.11 Intrusion into layered model with sandstone base.
Yellow particles are sandstone, blue particles represent granite, red particle represent magmatic intrusion. Biue lines are inter-particie bonds broken by normal failure. Pink iines are inter-particle bonds broken by shear failure. Intrusion expansion is preferred over further propagation. Dike jointing is observed in the upper granite iayer despite no invasion into iayer. Extensive microfracturing in observed in invaded sandstone iayer but also in the upper sandstone iayer with no intrusion.

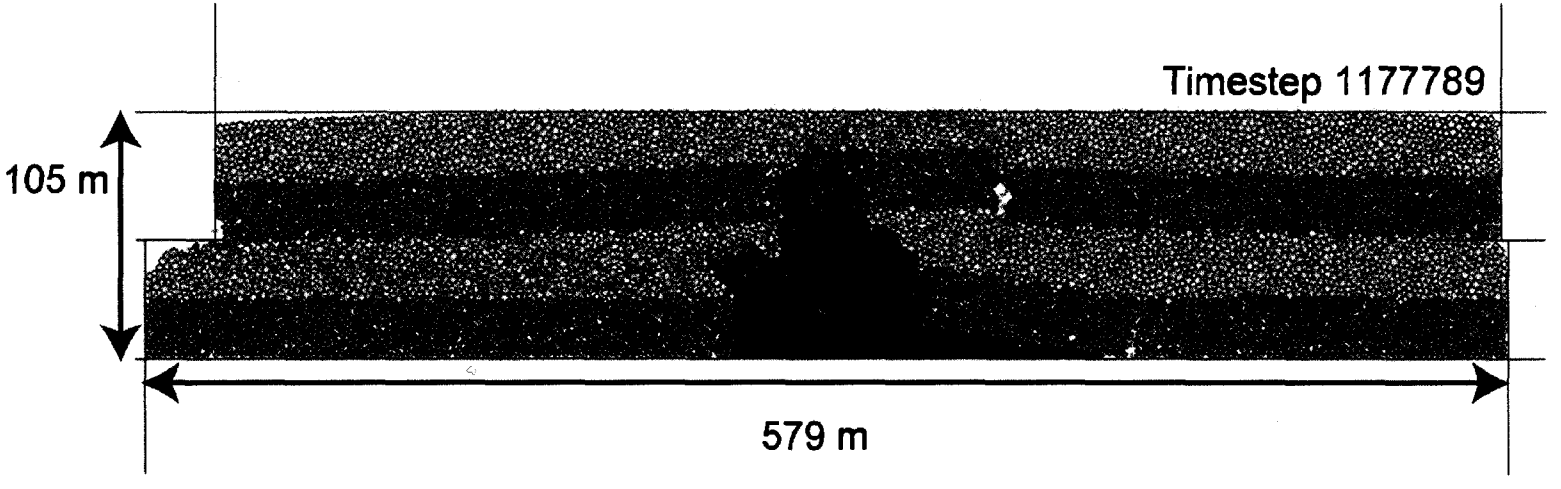

Figure 5.12 Intrusion into layered model with granite base.
Yellow particles are sandstone, blue particles represent granite, red particles represent magmatic intrusion. Blue lines are inter-particle bonds broken by normal failure. Pink lines are inter-partlcie bonds broken by shear fallure.

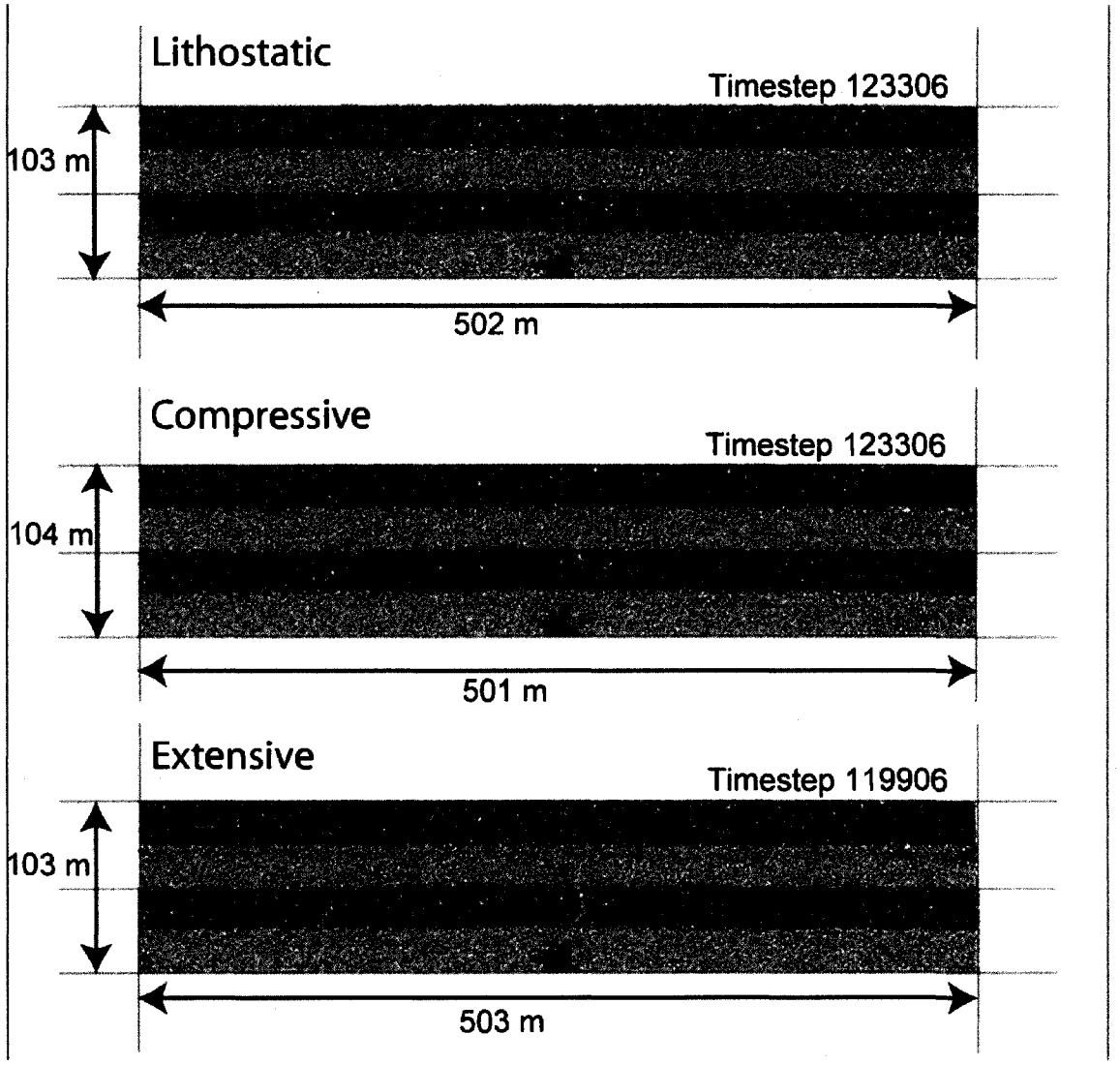

Figure 5.13 Intrusion into layered model with sandstone base with different stress regimes- early time.
Yellow particles are sandstone, blue particles represent granite, red particle represent magmatic intrusion. Blue lines are inter-particle bonds broken by normal failure. Pink lines are inter-particle bonds broken by shear failure.

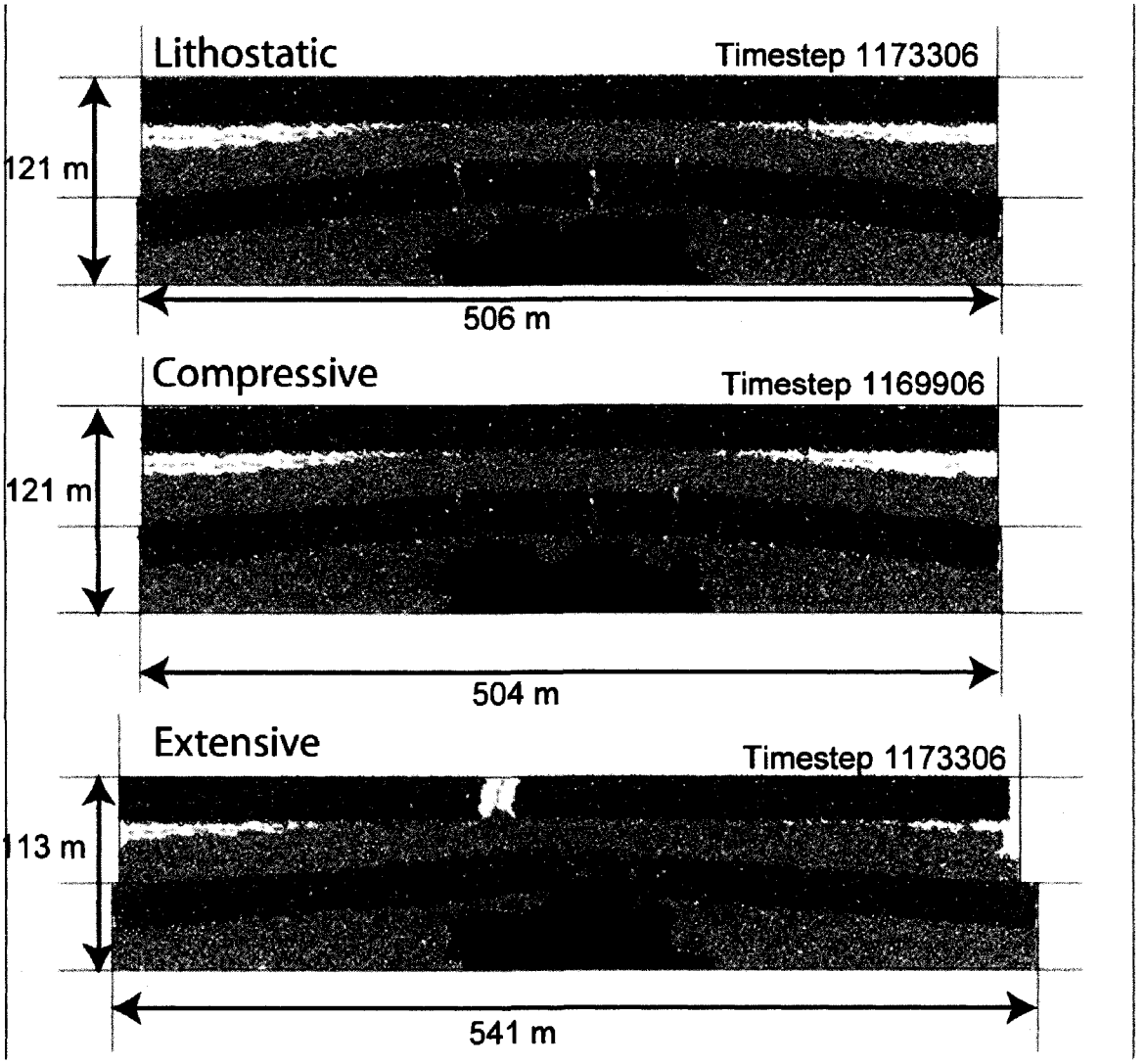

Figure 5.14 Intrusion into layered modei with sandstone base with different stress regimes- late time.
Yellow particles are sandstone, biue particles represent granite, red particle represent magmatic intrusion. Biue lines are inter-particle bonds broken by normal failure. Pink iines are inter-particie bonds broken by shear failure.

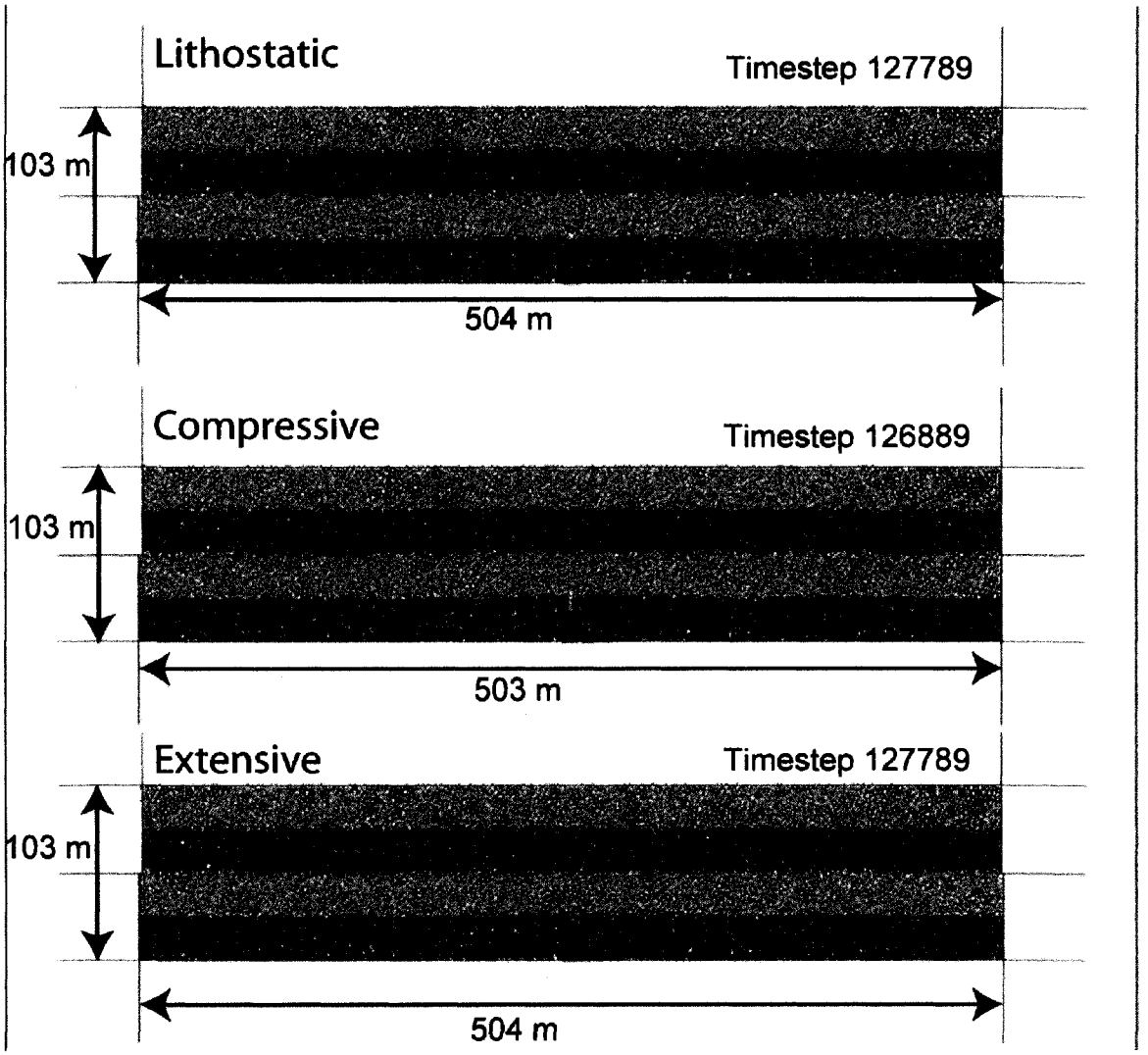

Figure 5.15 Intrusion into layered model with granite base with different stress regimes- early time.
Yellow particles are sandstone, blue particles represent granite, red particle represent magmatic intrusion. Blue lines are inter-particle bonds broken by normal failure. Pink lines are inter-particle bonds broken by shear failure.

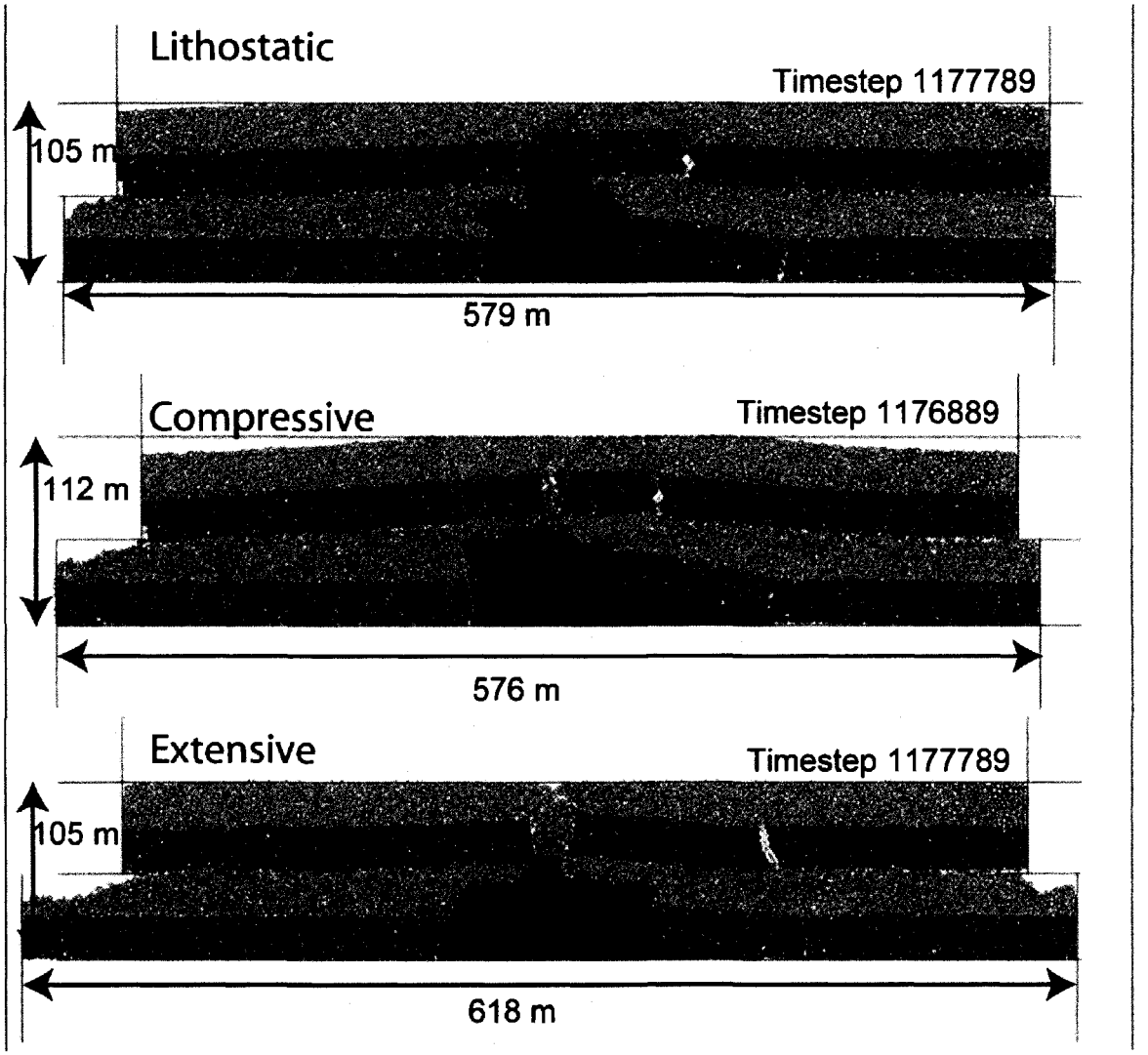

Figure 5.16 Intrusion into layered model with granite base with different stress regimes- late time.
Yellow particles are sandstone, blue particles represent granite, red particle represent magmatic intrusion. Blue lines are inter-particle bonds broken by normal failure. Pink lines are inter-particle bonds broken by shear failure.

Chapter 6 Conclusions

During the decompression experiments detailed in Chapter 1, the expansion of the bubbles caused melt shearing leading to bubble deformation and the enhanced coalescence. The readiness of the bubbles to deform was a function of the low surface tension and viscosity of the K-Phonolite melt as compared to the rhyolite melts more commonly studied. In a conduit setting, melt shearing could also arise from velocity gradients across the conduit. A further result of this deformation was that extensive permeability developed within the sample at a vesicularity of 40-50%. As the bubbles became connected to the external vapor, they lost excess vapor pressure, causing them to degas. After degassing, the connected bubbles collapsed, leaving remnant bubble textures and a significantly decreased sample porosity. Silicic melts with higher viscosity and surface tension tend to develop extensive permeability at much higher porosities (~65%) and to resist coalescence. Compared to those melts, the alkalic melt studied would degas earlier/lower in the conduit erupted samples should show features of bubble collapse. Surface tension and viscosity are therefore shown to be important controls on a melt's ability to degas.

The study presented in Chapter 2 revealed that a high N_v which constrains the narrow bubble size distribution and thereby inhibits coalescence is critical to the generation of an interconnected highly vesicular (~73% vol. %) magma. The close packed arrangement that the bubbles are forced to adopt, brings a new coalescence mechanism into play-

coalescence induced coalescence, where the coalescence of two bubbles promotes the coalescence of neighboring bubbles, generating large vugs. The presence of these vugs destabilizes the vesicular magma through stress concentrations leading to eventual collapse and abrupt degassing over a timescale of minutes. Thus degassing can be fast and these experiments also show that it can be almost complete. On a conduit scale, these results may be relevant to understanding vulcanian plug formation rates, overpressure buildup and effusive eruptions. This study shows that the initial N_v^m exerts significant control on the mode of degassing in highly vesicular rhyolite. A high N_v^m can lead to rapid and almost complete degassing at shallow depth. The experiments in Chapter 2 help in constraining the narrow range of melts to which N_v^m is critical in determining degassing behavior to highly silicic rhyolites.

In Chapter 3, the importance of the initial N_v was demonstrated. Complementing this, Chapter 4 described a new method, application of the 2D spatial statistics model Spatstat to nucleated bubble populations, which can quantitatively describe the spatial distribution of Nv for any sample. This model offers an improvement over simple visual recognition of bubble populations, used to discriminate between nucleation mechanisms qualitatively, that will enable researchers to quantify bubble nucleation mechanisms and discriminate between samples with complex bubble textures. This should be of significant help to the interpretation of future bubble and crystal nucleation studies.

In chapter 5, the particle code model, PFC^{2D} proved to be a useful tool for exploring dike mechanisms. The model results showed observed field relations such as extensive microfracturing across the weaker sandstone layers and parallel dike jointing at distances of 10's of meters in the stronger granite layers. Intrusion in the weak sandstone layers proceeded through dissipative growth after extensive microfracturing generating intrusions with widths of 10's of meters. Intrusion into granite where intrusions widths were somewhat less than in the sandstone, proceeded by the buildup of a critical strain within the granite layer leading to a crack propagating across the layer followed by magma invasion. Compressional and extensional regimes both acted to retard intrusion growth towards the surface. In the compressive regime, doming of overlying layers was preferred over dike propagation whilst in the extensional regime, lateral growth was preferred. A scaled dependence to fracture toughness was also observed to emerge from the modeling similar to field observations. The study showed that both lithology and regional stress regimes are important in controlling dike propagation. The intrusions patterns that result for each scenario however are complex and this study represents only a preliminary investigation into what may be a very rewarding research application.

The work contained in this thesis provides a board exploration of the critical parameters which control eruptive styles and the initiation of a volcanic eruption using methods which range from experimental to statistical to computational. Inspiration and the adaptation of models or techniques from areas diverse as polymer physics and the

generation of titanium bone implants have been key to the interpretation of much of the work contained in this thesis. This multidisciplinary approach to volcanological problems has yielded insights that might not have been possible otherwise.

Appendix 1

Manual for the generation and analysis of spatial point patterns derived from intersected bubble centroids with a polished surface

Software Installation

Spatstat (http://www.cran.rproject.org/src/contrib/Descriptions/spatstat.html), by Baddeley and Turner (2005), is a package developed for the **R** (R.D.C. Team, 2007) statistical computing platform. **R** compiles and runs on UNIX, Windows and MacOS. Instructions for downloading and installing both R and Spatstat can be found at the above website.

Point Pattern Loading

To load the point pattern data (i.e. bubble centroids), open the R GUI and load the Spatstat package using the command ***library(spatstat)*** and set the working directory to the folder containing your point pattern files ***File>Change dir***.

Before importing the sample point patterns, a sample window must be created using the coordinates of the sample perimeter. To create the window object, ***window*** use

window <- owin(poly=list(x=c(0.5,1,0.5,.....),y=c(0,1,2,.....)))

where the x and y coordinates are the exported sample perimeter coordinates. The sample point pattern can then be imported and associated with this window.

Create the point pattern object, ***Example***, using points collected in the file sites_example.tab, within the window object, ***window***, using the command

Example <- scanpp("sites_example.tab", window, dir="",

header=FALSE, multitype=FALSE)

To check that the point pattern object, ***Example,*** reproduces the point pattern correctly use ***plot(Example)*** to generate a plot of the point pattern within its associated window (Figure 4.1) and compare with the original photomontage, and threshold images.

Point Pattern Summary

Spatstat provides a number of ways to observe and derive fundamental data from a point pattern containing experimental bubble centroids. The number of bubbles within the analytical window and the 2d bubble number density can be found using the function ***summary(Example)***. A plot of the bubble centroid locations can be created using ***plot(Example***), as described above, and compared with a shaded relief contour map image of bubble density across the surface of the sample (Figure 4.4). The spatial homogeneity of the point pattern can be assessed using a kernel smoothed intensity plot. The second parameter within the brackets is the kernel size which is defined as the standard deviation of the Gaussian smoothing kernel.

plot(density.ppp(Example,100,dimyx=c(300, 300)),xlab='x

(micron)',ylab='y (micron)')

Since bubbles nucleated around the edges of the sample may not be controlled by the same processes as bubbles in the center, we may wish to remove them to allow analysis

of "internally" nucleated bubbles only. This can be achieved in an objective manner using the following function which reduces the window of analysis by a given distance.

new_300 <- erode.owin(window, 300)

The subset of points falling within this window can be exported to a new point pattern object for separate analysis using the following function.

int_300 <- Example[new_300]

Distribution functions can be derived from the point pattern of interest, and applied specifically to decipher bubble nucleation processes. The ones of most interest and their command lines are listed below.

Nearest Neighbor Distribution Function G(r)

To create the object ***G_Example*** which is a function value object containing the estimated values of G(r) for the point pattern, ***Example*** use the ***Gest*** command as follows

G_Example <-Gest(Example)

Calculations of G(r) can be affected by biases introduced through edge effects. Spatstat corrects for this bias using either the Kaplan-Meier or a reduced sample estimator. The reduced sample estimator excludes points that lie within a certain distance from the sample edges. The Kaplan-Meier estimator detailed in (Baddeley, 1998) utilizes G(r).

Ripley's K-Function

Similarly the ***Kest*** command can be used to calculate K(r), Ripley's K-function for a given point pattern .The command ***Lest*** will generate L(r) for a point pattern, a commonly-used transformation of K(r) which transforms the Poisson K function to the straight line $L_{Poiss}(r) = r$.

MaternII Model

In the MaternII Model, the points of the homogeneous Poisson process are marked by independent arrival times. Any point that lies closer than a distance r from another point that has an earlier arrival time is deleted. To create the object ***rmII*** for a point pattern with intensity, kappa, with an inhibition distance of r, use the following command line.

rmII <- rMaternII(kappa,r,win=owin(c(o,1,.....),c(o,1,.....)))

Monte Carlo Method

To test the significance of any deviations of observed distributions from the equivalent Poisson distribution, a Monte Carlo method is available within Spatstat. By generating 39 point patterns using a Poisson distribution with the same average intensity as the observed pattern, two further curves forming an envelope around the Poisson curve are generated and represent the Poisson curve at ± 5% significance (e.g. Figure 4.7). The command line required to generate the envelope at ± 5% significance is shown below.

E <- envelope(Example, Kest, nsim = 39, rank = 1)

Data Export

To export the distribution data to a table which can be opened in a plotting program such as excel, use the following

write.table(F_Example, file="F_Example.txt", append=FALSE, quote=TRUE, sep=" ", row.names=TRUE, col.names=TRUE)